AN ABSTRACT OF THE THESIS OF

Shusheng Luan for the degree of Doctor of Philosophy in Oceanography presented on June 28, 1993.

Title: Long-term Momentum and Heat Balances and Turbulent Mixing in the Upper Equatorial Pacific Ocean

Redacted for privacy

Abstract approved: _____
Clayton A. Paulson

The unique properties of high shear, low R_i, zero inertial rotation, and strong diurnal variations of the upper equatorial ocean provide an ideal settings for testing models of turbulent mixing. Initially, we utilize inverse methods to construct the long-term balances of zonal momentum and heat in the upper 200 meters of the equatorial Pacific Ocean at 152°W from meteorological and oceanic data. Then we use the time-independent forcing terms obtained from inverse analysis to drive a simple critical-R_i model of turbulence, modified from Price *et al.* (1986) by excluding the bulk Richardson number mixing and adding a background diffusion of constant diffusivity.

The modeled steady-state velocity, temperature, turbulent fluxes and diffusivities are consistent with analysis. However, strong transient behavior of the model with a time scale of 100 days due to vertical advection underscores the importance of spin-up of a turbulence model before investigating effects of time-varying surface forcing.

When solar radiation is allowed to vary diurnally, the simulated diurnal cycle of turbulent mixing has two prominent phases: during the day, the solar insolation creates stratification that interrupts the strong turbulent transfers between the westward wind and the eastward EUC core; during the night, the surface cooling re-establishes their interaction through a 100-m deep water column. The diurnal cycle of turbulent dissipation compares well to the Tropic Heat 1984 measurements.

The model uses only a local gradient Richardson number criterion to parameterize mixing. Model tests show that the inclusion of a bulk Richardson number criterion (as used in previous model simulations) distorts the turbulent mixing in both the steady and diurnally varying cases. The model periodically (7 days on average) results in an intense mixing event, then allows the gradual build-up of shear until the next catastrophic mixing event (even when all forcing terms are time-independent). The model produces smaller mean vertical gradients and highly intermittent time series of modeled velocity and temperature near the surface. It seems inconsistent to include both the bulk and the gradient Richardson number as mixing criteria in a model of turbulence.

Long-term Momentum and Heat Balances and Turbulent Mixing in the Upper Equatorial Pacific Ocean

by

Shusheng Luan

A Thesis Submitted to

Oregon State University

in partial fulfillment of

the requirements for the degree of

Doctor of Philosophy

Completed June 28, 1993

Commencement June 1994

APPROVED:

Redacted for privacy

Professor of Oceanography in charge of major

Redacted for privacy

Dean of College of Oceanographic and Atmospheric Sciences

Redacted for privacy

Dean of Graduate School

Date thesis presented June 28, 1993

Typed by Shusheng Luan for Shusheng Luan

To

My wife, my father and mother,

Mr. Liangwu Shang, my primary school teacher,

And the memory of the students in Beijing on June 4, 1989.

ACKNOWLEDGEMENTS

I am most grateful to my major advisor, Dr. Clayton A. Paulson, for providing me the opportunity and the guidance for my life as a graduate student here at OSU. It has been very rewarding to work with his patience, understanding, dedication and professionalism. I thank Dr. Paulson for the help and care he has given to my family. He has been not only a great teacher to me, but also a great friend, to me and my family.

I thank both Dr. Paulson and Dr. P. Ted Strub for being my major professors, being kindly available for the numerous short-notice meetings and casual discussions. Both have provided many valuable encouragement, insights, and guidance to this thesis work, which has turned out to be a very challenging and rewarding experience. I also appreciate the indispensable assistance from the Committee Members: Profs. Clayton A. Paulson, P. Ted Strub, Robert S. Yeats, Richard M. Adams, Roland A. de Szoeke, Murray D. Levine, and James N. Moum.

I am indebted to Dr. James F. Price for providing the code of the Price *et al.* (1986) model of turbulence, and to Dr. David Halpern for providing the EPOCS and NORPAX mooring data. My knowledge of the equatorial oceans have been enhanced by the 1991 Summer Workshop on Equatorial Physics, taught by Profs. Lewis Rothstein, Dennis Moore, James O'Brien, Julian McCreary, Michael McPhaden, and others. Discussions with Dr. Rebecca Schudlich about her modeling work have also contributed to my research.

It has been a great privilege for me to know Dr. John S. Allen, who inspired my strong interests in the nonlinear dynamics and chaos in the ocean, and to know Dr. Roland A. de Szoeke, who helped me with the derivations related to penetrative convection. And I am thankful to all other instructors who taught me great courses: Drs. Thomas M. Dillon, Murray D. Levine, James N. Moum, Dudley B. Chelton, Andrew F. Bennett, Robert N. Miller, and Charles B. Miller, in a incomplete long list. I must thank Dr. Pricilla Newberger for her great kindness and helpful computation expertise ever since I was new to the college, Dr. Jack A. Barth for patient assistance with LaTeX, Mr. Steve R. Gard and Mr. Eric Beals for the intensive care for my computer needs, and Mr. Thomas G. Leach and Mr. Charles Sears for their assistance with system management problems. And my student life at OSU won't have been as smooth without the many very friendly and kind assistances from Mrs. Donna Obert and Joyce Weathers.

My international experience would not be as successful without the great understanding and precious help from so many great people. I treasure the friendship with Dr. George H. Keller and his wife Mrs. Sussan Keller, who I knew back in China, and who have provided me with unforgettable parental as well as academic advice. And I enjoy the hospitality of and continue the friendship with the family of Mr. Kyle Janssen and Dr. Carol Harding, and their lovely son Bryn and daughter Tira.

I thank Dr. Zhenlin Li and his wife Jingping Wang who were there for me in my early days in Corvallis, and all other alumni from Qingdao, China, who arranged many happy gatherings with wonderful meals and sometime "intense" GoJi games (a card game born to Qingdao City). And I will never

forget the hard time I had to live through in the Spring of 1989 with the other members of the Chinese Students and Scholars Association (CSSA) at Oregon State University. Generous help from the Corvallis community have taught me the value of international peace, human rights, and freedom and democracy. I will treasure the excellent workmenship during that period of time and the close friendship thereafter with Guangwen Zhou, Deqian Wang, Yimin Zeng, Guangchao Zhang, Yongsheng Feng, and their families. In addition, I thank the CSSA officers of every term I was in Corvallis for their dedication and hard work to promote friendship between members and the Corvallis community.

My acknowledgement will never be complete without mentioning my great friendship with my long-time colleagues, Fred Bahr and Hemantha W. Wijesekera, who my wife and I enjoyed hiking and camping with in the central Oregon Cascades. My great thanks to Gongming Wang and Yimin Zeng for proof reading the earlier drafts of my thesis. I also enjoyed the understanding, friendship, help and support from Eric Fields, Vassilis Zervakis, Ayal Anis, Hongbo Qi, Robin Tokmakian, Alberto Mestas-Nũnez, Ed Zaron, Steve Pierce, Hongyan Li, Tom Strand, Scott Pegau, Marcelino Suzuki, Bo Huang, Chaojiao Sun, Yao Yunda, Shanji Zhang, and so on. Friends, teachers, and colleagues I have not specifically mentioned, thanks for your kind help and support all these years.

This study was supported by National Science Foundation and Office of Naval Research.

Table of Contents

List of Figures

List of Tables

Long-term Momentum and Heat Balances and Turbulent Mixing in the Upper Equatorial Pacific Ocean

Chapter 1

General Introduction

Strong diurnal cycles of current, temperature, and dissipation rates of turbulent kinetic energy, were detected during the Tropic Heat measurements of November 1984 (TH84) at 140°W in the upper equatorial Pacific (Gregg *et al.*, 1985; Moum and Caldwell, 1985; Toole *et al.*, 1987; Peters *et al.*, 1988; Moum *et al.*, 1989). During daytime, when solar heating stablized the upper layer, only weak turbulent dissipation was measured and limited to the top 10 meters most of that time. During nighttime, surface cooling deepened the surface mixed layer and destabilized the flow further down, dissipation of order $10^{-7}\,\mathrm{m^2\,s^{-3}}$ was observed to extend to depths of 80 m. The observed dissipation rate at mid-latitides is 100 times smaller, with much shallower penetration below the nighttime mixed layer depth (Shay and Gregg, 1986;

Price *et al.*, 1986, hereafter, PWP). The upper equatorial Pacific was also observed to have high vertical shear, strong surface heating, a westward wind stress, a sharp thermocline, and an energetic equatorial undercurrent (EUC) as deep as 120 m (Knox and Halpern, 1982; Gregg *et al.*, 1985; Moum and Caldwell, 1985). Consequently, the gradient Richardson number, R_i, was low and close to its critical value, $R_{ic} = 0.25$, in the upper water column as deep as 100 m, another property rarely seen at mid-latitude.

Therefore, it is important to study the diurnal cycle of turbulent mixing and its interaction with the large-scale equatorial flow system. The properties of high shear, low Richardson number, and zero Coriolis force, in the upper equatorial ocean, provide a unique setting for testing numerical models of turbulence and improving our knowledge of mixing processes in the ocean. One of the obvious models, suggested by the low gradient Richardson number, is a simple critical-R_i model introduced by PWP. It is a one-dimensional, time-dependent mixed-layer model of the upper ocean, based on shear instability as its mixing mechanism and requires the fewest adjustable parameters in models of its class. PWP applied the model to simulate diurnal cycles of turbulent mixing in the mid-latitude oceans. Schudlich and Price (1992) (hereafter, SP) simulated the diurnal cycle observed during the 12 days of TH84 at 140°W on the equator, using the PWP model.

The long-term steady state of the upper equatorial ocean are proved to possess the same properties observed during the short-term cruises. A recent study of historic hydrology data at 152°W showed high shear and low R_i (also close to 0.25) in the upper 70 m, implying persistent strong turbulent mixing at the equator on a long-term basis (Luan *et al.*, 1991a).

However, studying the effects of the diurnal cycle using simple models of turbulence calls for a comprehensive prescription of model forcing, which was not done by previous studies (*e.g.*, SP). A systematic approach to such goals has been pursued in this dissertation. Because the short-term observations like Tropic Heat 84 supplied only a very limited data set, long-term data sets are used to study the steady-state system of the upper equatorial dynamics and thermodynamics (Chapter 2). The comprehensive understanding of the upper equatorial ocean provides a sound basis for the study of turbulent mixing and the interaction between the air and sea. Model simulation of the steady-state turbulent mixing was very helpful for evaluating general model performance and for looking at the transient behaviors that might seriously contaminate the diurnal signals (Chapter 3). With these major questions cleared, the details of the diurnal processes in the upper equatorial ocean can be effectively modeled and better understood, and model parameterizations of turbulent mixing be assessed when compared with observations (Chapter 4).

Chapters 2 through 4, titled "Long-Term Budgets of Momentum and Heat in the Upper Equatorial Pacific", "A Critical-R_i Model of Turbulent Mixing Applied to the the Upper Equatorial Pacific", "Models of the Diurnal Cycle of Mixing in the the Upper Equatorial Pacific", respectively, are papers coauthored with Drs. Clayton A. Paulson and P. Ted Strub. The papers are to be submitted for publication in either the Journal of Geophysical Research, the Journal of Physical Oceanography, or other suitable periodicals. They are referenced as Luan *et al.* (1993a), Luan *et al.* (1993b), and Luan *et al.* (1993c) in chapters other than its own equivalent.

Chapter 2

Long-Term Momentum and Heat Balances in the Upper Equatorial Pacific Ocean

Abstract

Long-term observations of velocity and temperature in the equatorial Pacific were analyzed to obtain budgets of zonal momentum and heat in the upper 200 m at 152°W. The inverse analysis yielded vertical profiles of vertical velocity, terms in the momentum and heat balance equations, vertical turbulent fluxes of momentum and heat and turbulent diffusivities for momentum and heat.

The estimate of vertical velocity *vs.* depth is close to parabolic, zero at the surface, increasing to a maximum of $2.7 \times 10^{-5}\,\mathrm{m\,s^{-1}}$ at a depth of 100 m and decreasing to a value close to zero at 200-m depth. This estimate of vertical velocity is in good agreement with the average of previous observations when allowance is made for the variation with longitude of the depth of the maximum. Vertical velocity from the inverse analysis is in poor agreement with previous results from a general circulation model.

The estimated zonal momentum balance in the high shear region above the equatorial undercurrent core (EUC, 125-m depth) is dominated by the zonal pressure gradient, the vertical turbulent transport divergence and vertical advection. Below the EUC core, the dominant terms are vertical and horizontal advection. All terms are insignificant compared to the residual at 200-m depth. The vertical integral of the zonal pressure gradient is close to the wind stress. The wind stress estimated from the inverse analysis ($0.048\,\mathrm{N\,m^{-2}}$) is in excellent agreement with previous estimates from the wind field.

The estimated heat balance between 70 and 200-m depth is dominated by zonal and vertical advection. In the upper 70 m, vertical turbulent heat transport divergence and meridional eddy transport divergence are also important terms. Heat flux at the surface estimated from the inverse analysis is more than twice as large ($97\,\mathrm{W\,m^{-2}}$) as previous estimates from meteorological observations ($40\,\mathrm{W\,m^{-2}}$). Even though a value larger than $40\,\mathrm{W\,m^{-2}}$ is plausible, it is within the range of uncertainty of the inverse estimate.

Turbulent diffusivities for momentum and heat were estimated as functions of depth. The ratio of the diffusivities is close to one and they decrease from $0.0047\,\mathrm{m^2\,s^{-1}}$ at the surface, consistent with a log-layer estimate, to 0.0010 at 80-m depth. The near-surface estimates of diffusivity are close to previous estimates based on observations of dissipation, but the dissipation estimates decrease much faster with depth and are approximately an order of magnitude smaller than the inverse estimates at a depth of 80 m. This result

agrees with a previous conclusion that turbulent viscosity must be larger than the dissipation estimates to balance momentum. The reason for the discrepancy may be due to the transport of momentum by internal waves.

2.1 Introduction

The momentum and heat balances in the upper 200 meters of the equatorial oceans have features different from those at higher latitudes. In the equatorial Pacific, the easterly trade winds drive a westward surface flow, the South Equatorial Current (SEC), which causes a water mass buildup in the western Pacific. The sea level difference between the western and eastern Pacific induces a zonal pressure gradient, which drives an eastward subsurface jet as strong as $1\,\mathrm{m\,s^{-1}}$, the equatorial undercurrent (EUC). The vertical shear in the zonal velocity is as large as $0.02\ \mathrm{s^{-1}}$ between the SEC and EUC, which causes strong turbulence and vertical mixing, evident in microstructure measurements (Gregg *et al.*, 1985; Chereskin *et al.*, 1986; Peters *et al.*, 1988; Dillon *et al.*, 1989; Moum *et al.*, 1989).

The trade winds drive poleward Ekman transport both north and south of the equator which, in turn, drives upwelling to compensate for the loss of mass at the equator. Upwelling causes a tongue of cold water in the eastern equatorial Pacific (Fig. 1a). Large transports of momentum and heat are associated with both vertical and horizontal advection on the equator (Fig. 1b). The strong stratification also supports the existence of internal waves.

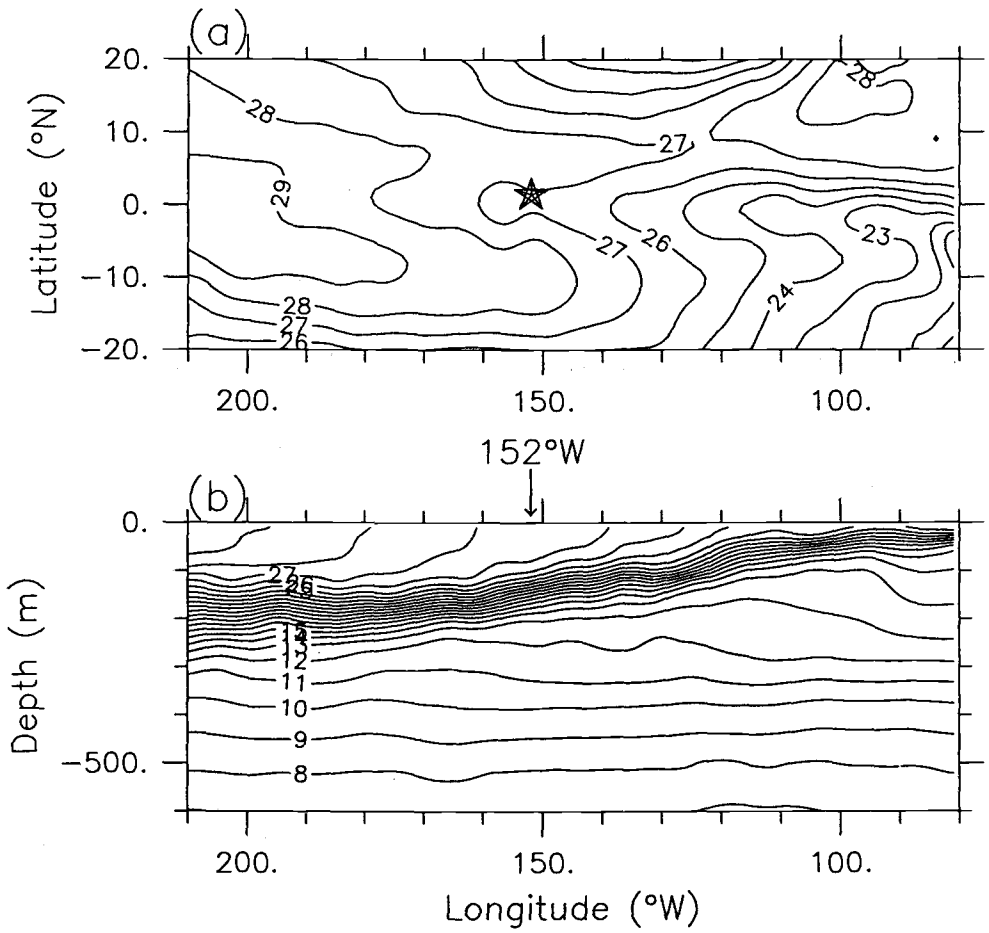

Figure 1. Contours (a) of mean sea surface temperature and (b) of mean temperature *vs.* depth in the equatorial mid-Pacific from Levitus (1982). The location (0°N, 152°W) of the analysis reported in this paper is marked.

The steady-state zonal momentum and heat conservation equations can be written as

$$\overline{U}\frac{\partial\overline{U}}{\partial x}+\overline{V}\frac{\partial\overline{U}}{\partial y}+\overline{W}\frac{\partial\overline{U}}{\partial z}+\frac{\partial\overline{U'U'}}{\partial x}+\frac{\partial\overline{V'U'}}{\partial y}=-\frac{1}{\rho_\circ}\frac{\partial\overline{P}}{\partial x}-\frac{1}{\rho_\circ}\frac{\partial\overline{F}_m}{\partial z} \tag{2.1}$$

$$\overline{U}\frac{\partial\overline{T}}{\partial x}+\overline{V}\frac{\partial\overline{T}}{\partial y}+\overline{W}\frac{\partial\overline{T}}{\partial z}+\frac{\partial\overline{U'T'}}{\partial x}+\frac{\partial\overline{V'T'}}{\partial y}=-\frac{1}{\rho_\circ C_p}\frac{\partial\overline{F}_h}{\partial z} \tag{2.2}$$

where

$$\overline{F}_m=-\rho_\circ\overline{K}_m\frac{\partial\overline{U}}{\partial z} \tag{2.3}$$

$$\overline{F}_h=-\rho_\circ C_p\overline{K}_h\frac{\partial\overline{T}}{\partial z} \tag{2.4}$$

Here x, y and z are positive eastward, northward and upward ($z=0$ at the sea surface), respectively; U, V, W and T are the zonal, meridional and vertical velocities and temperature, respectively; P is the pressure, $\rho_\circ$ is density, and C_p is specific heat of seawater; F_m and F_h are the vertical turbulent fluxes of zonal momentum and heat, respectively; K_m is the vertical turbulent viscosity and K_h the vertical turbulent diffusivity of heat. Except for $\rho_\circ$ and C_p, all variables are functions of z. The long-term mean, denoted by overbars, is intended to be an average over a year or longer; the fluctuations, denoted by primes, are variations with time scales from a day to a year (Bryden and Brady, 1989). Contributions of horizontal turbulent fluxes with scales less than those of meso-scale eddies are neglected on the basis that horizontal gradients of velocities are orders of magnitude smaller than vertical gradients. Interannual variabilities and El Niño phenomena are beyond the scope of this paper.

The objective of the present paper is to construct long-term balances of zonal momentum and heat in the upper 200 meters at 152°W in the equatorial Pacific. While many studies of large-scale momentum and heat budgets in the equatorial Atlantic or Pacific have been reported (Bryden and Brady, 1985; Pares-Sierra *et al.*, 1985; Enfield, 1986; Philander and Pacanowski, 1986b; Bryden and Brady, 1989; Wacongne, 1989 and 1990), little effort has been devoted to the vertical structure of the momentum and heat balances at this location. We will examine how different processes contribute to conserving momentum and heat. In Section 2.2 we survey the long-term observations of meteorology and the upper ocean at 152°W on the equator. In Section 2.3 we describe the inverse method. The inverse solutions for the vertical velocity are discussed in Section 2.4, the zonal momentum balance in Section 2.5, the heat balance in Section 2.6, the turbulent fluxes of zonal momentum and heat in Section 2.7. The inverse solutions for the turbulent diffusivities are presented and compared to previous results from microstructure experiments in Section 2.8. Section 2.9 is on the gradient Richardson number and Section 2.10 contains conclusions. Sensitivities of the inverse solutions to a variety of weighting methods, representations of vertical velocity and turbulent fluxes, values of background turbulent diffusivity, and perturbations of forcing terms, are presented in the Appendix.

2.2 Observations

In this section we describe observations in the upper 200 m near 0°N, 152°W, and estimate the magnitude of terms in the momentum and heat balance equations (Eqs. 2.1 and 2.2). The surface wind stress and heat flux and the terms in the equations are estimated as a prelude to the inverse analysis described in the next section.

Surface wind stress and net heat flux at 0°N, 152°W, have been estimated by a number of investigators. The climatological average wind stress estimated by Wyrtki and Meyers (1976) is $\tau_o^x = -0.048\,\mathrm{N\,m^{-2}}$ (positive eastward), about 20% smaller than the value $-0.06 \pm 0.02\,\mathrm{N\,m^{-2}}$ estimated by Hellerman and Rosenstein (1983). The stress varies seasonally by a factor of 2 at this location (Hellerman and Rosenstein, 1983). The climatological average net surface heat flux is estimated to be $-40\,\mathrm{W\,m^{-2}}$ (net heating) with a 95% confidence interval of $\pm 50\,\mathrm{W\,m^{-2}}$ (Weare *et al.*, 1981; Esbensen and Kushnir, 1981). In this study we chose $-0.05\,\mathrm{N\,m^{-2}}$ and $-40\,\mathrm{W\,m^{-2}}$ as imposed values of surface wind stress and net heat flux, respectively.

The primary observations of currents used in this paper were reported by Knox and Halpern (1982) and analyzed by Bryden and Brady (1989). An array of moorings was deployed within a degree of the equator at 152°W for the 15-month period from April, 1979 to June, 1980. In addition, currents observed from a mooring on the equator at 140°W from August, 1983 to July, 1985 (Halpern and Weisberg, 1989) are used to obtain horizontal derivatives of zonal velocity. No El Niño occurred during either of the observation periods. Data was recorded at five depths of 20, 50, 100, 150, and 250 m for

152°W, and at seven depths of 10, 20, 50, 75, 100, 150, and 250 m for 140°W (Fig. 2). Bryden and Brady (1989) estimated that zonal velocities at 152°W had standard errors increasing from about $0.03\,\mathrm{m\,s^{-1}}$ at 250 m to $0.10\,\mathrm{m\,s^{-1}}$ at and above a depth of 120 m. The error estimates at 140°W were similar (Halpern and Weisberg, 1989).

Zonal velocity in the upper 10 meters at 140°W and 20 meters at 152°W was estimated by extrapolation. The extrapolation is composed of an upper and a lower segment. The upper segment is a logarithmic profile which extends downward from the depth of an estimated roughness length, $z = -z_o = -0.0001$ m:

$$\overline{U}(z) = U_o - \frac{u_*}{\kappa} \ln \frac{-z}{z_o}, \quad \text{for } z \leq -z_o \tag{2.5}$$

where U_o is the velocity at $z = -z_o$, $u_* = \tau_x/(|\tau_x|\,\rho_o)^{\frac{1}{2}}$ is the friction velocity, τ_x is the surface wind stress, and $\kappa = 0.4$ is the von Karman constant. The lower segment is a linear extrapolation upward from the two uppermost data points. The segments meet at a depth where they have equal values of zonal velocity and vertical shear. These matching conditions determine the matching depth and the value of U_o. For $\tau_x = -0.05\,\mathrm{N\,m^{-2}}$, $U_o = -0.32\,\mathrm{m\,s^{-1}}$ and the matching depth is 1.94 m at 152°W, and $U_o = -0.43\,\mathrm{m\,s^{-1}}$ and the matching depth is 1.31 m at 140°W. Because the current data and temperature data used in this paper does not resolve vertical scales better than 1 m, we take the velocity averaged over the top 1 m as the surface value for $\overline{U}(z)$ at $z = 0$. For $\tau_x = -0.05\,\mathrm{N\,m^{-2}}$, $\overline{U}(0) = -0.18\,\mathrm{m\,s^{-1}}$ at 152°W, and $\overline{U}(0) = -0.29\,\mathrm{m\,s^{-1}}$ at 140°W. Varying τ_x by ±50% or z_o by plus/minus an order of magnitude

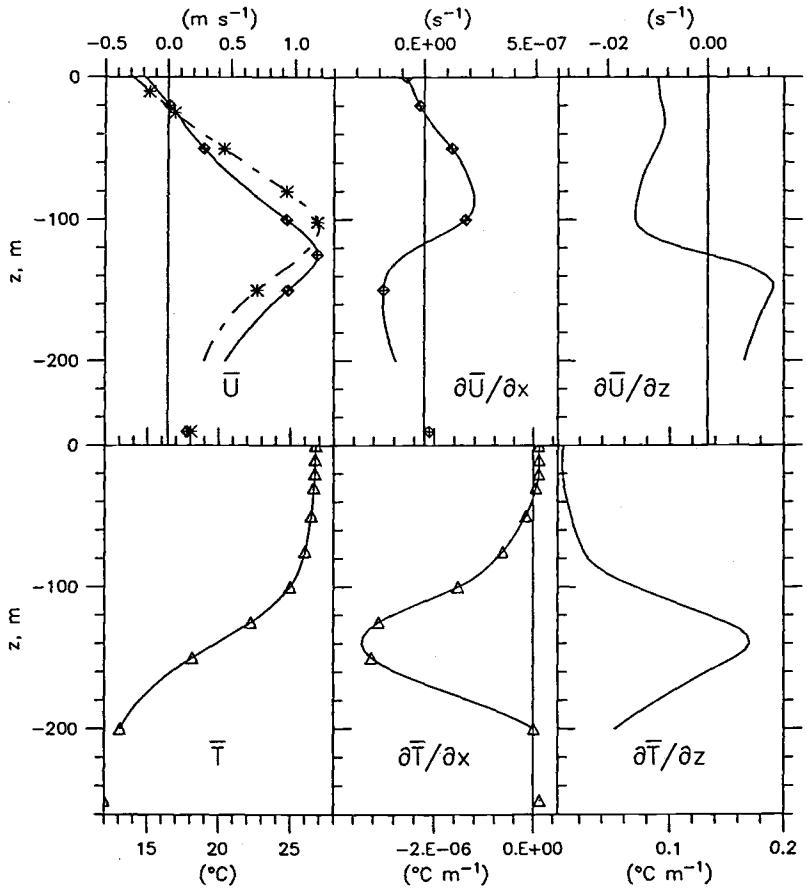

Figure 2. Long-term mean observations at 152°W used as forcing for the inverse analysis. The solid and dashed lines are fourth-order splines fit to the observations (symbols) in the upper 250 m. Zonal velocity, $\overline{U}$, (solid line) and its vertical gradient are from Bryden and Brady (1989). The zonal velocity gradient, $\partial\overline{U}/\partial x$, is obtained from the difference between the observations at 152°W and those reported by Halpern and Weisberg (1989) at 140°W (dashed). Temperature, $\overline{T}$, and its zonal and vertical gradients are from Levitus (1982).

changes $\overline{U}(0)$ by only $0.01\,\mathrm{m\,s^{-1}}$. Therefore, the above method of extrapolating zonal velocity to the surface is not sensitive to changes in u_* and z_o.

We have inserted a maximum velocity of $1.2\,\mathrm{m\,s^{-1}}$ at the depth of 125 m at 152°W, in addition to the data available from the moorings. The need for this additional point is due to the poor vertical resolution in the observations at the undercurrent core. The estimate of the depth and strength of maximum velocity is based on the average velocity profile observed during the Hawaii-Tahiti Shuttle Experiment between 150°W and 158°W (Wyrtki and Kilonsky, 1984). The shape of the velocity profile is assumed similar in both cases.

Continuous vertical profiles of zonal velocity were obtained by fitting the observations, the estimated maximum, and the extrapolated values in the surface layer with a fourth-order spline. The fitted curves are plotted in Fig. 2 for the upper 200 m, the region of interest. The vertical gradient of zonal velocity at 152°W is the derivative of the spline-fitted $\overline{U}(z)$. The zonal gradient of zonal velocity is determined from the difference between $\overline{U}(z)$ at 152°W and that at 140°W.

We can estimate the magnitude of the zonal advection term, $\overline{U}\partial\overline{U}/\partial x$, from Fig. 2. The zonal velocity is of order $1\,\mathrm{m\,s^{-1}}$ and the zonal gradient $\partial\overline{U}/\partial x$ has a maximum of $2\times10^{-7}\,\mathrm{s^{-1}}$. The zonal advection term is therefore of order $2\times10^{-7}\,\mathrm{m\,s^{-2}}$.

We may also estimate the magnitude of the meridional advection term, $\overline{V}\partial\overline{U}/\partial y$. The observed mean meridional velocity $\overline{V}$ has a magnitude of $0.04\,\mathrm{m\,s^{-1}}$ (Bryden and Brady, 1989). The standard error increases from

about $0.015\,\mathrm{m\,s^{-1}}$ at deeper levels to $0.035\,\mathrm{m\,s^{-1}}$ near the surface. We approximate $\partial\overline{U}/\partial y$ with a parabolic interpolation to data at each depth of the three moorings at 152°W within 72 km north and south of the equator (Bryden and Brady, 1989). The resulting magnitude of $\overline{V}\partial\overline{U}/\partial y$ is $3\times10^{-8}\,\mathrm{m\,s^{-2}}$.

Temperature data used in this paper are from the climatological atlas of Levitus (1982). The atlas has data at standard depths 0, 10, 20, 30, 50, 75, 100, 125, 150, 200, 250, 300 m and below, with a horizontal resolution of 1° longitude by 1° latitude. We form the temperature field in the upper 300 meters for the vertical section along the equator from 147°W to 157°W by fitting a parabola at each standard depth. Estimates of temperature and its zonal gradient are thus obtained at 152°W at each standard depth (Fig. 2). Fourth-order splines are then fitted to the estimates to obtain continuous profiles of $\overline{T}$ and $\partial\overline{T}/\partial x$ in the upper 200 m at 152°W (Fig. 2). The vertical temperature gradient, $\partial\overline{T}/\partial z$, follows directly. Use of the ±5° zonal curve fitting reduces noise caused by irregular sampling.

The magnitude of the zonal advection term, $\overline{U}\partial\overline{T}/\partial x$, can be estimated from the data in Fig. 2. The estimated zonal gradient, $\partial\overline{T}/\partial x$(z), has a maximum of $3.5\times10^{-6}\,^{\circ}\mathrm{C\,m^{-1}}$ between 125 and 150 m. The term $\overline{U}\partial\overline{T}/\partial x$ is thus of order $3.5\times10^{-6}\,^{\circ}\mathrm{C\,s^{-1}}$ or $0.3\,^{\circ}\mathrm{C\,day^{-1}}$.

We may also estimate the magnitude of the meridional advection term, $\overline{V}\partial\overline{T}/\partial y$. Fitting a parabola to the Levitus data at each standard depth from 2°S to 2°N along 152°W yields a $\partial\overline{T}/\partial y$ of order $10^{-6}\,^{\circ}\mathrm{C\,m^{-1}}$. Thus $\overline{V}\partial\overline{T}/\partial y$ is of order $4\times10^{-8}\,^{\circ}\mathrm{C\,s^{-1}}$.

The horizontal, meso-scale, eddy transport terms were calculated by Bryden and Brady (1989) from the time series of daily-averaged measurements of velocity and temperature at 110°W and 152°W. Zonal differences were then calculated between 152°W and 110°W, and meridional differences were calculated between 72 km north and south of the equator at 152°W. The divergence of meso-scale meridional eddy transport of zonal momentum is of order $10^{-7}\,\mathrm{m\,s^{-2}}$. The divergence of meso-scale meridional eddy transport of heat is of order $10^{-7}\,^{\circ}\mathrm{C\,s^{-1}}$. The zonal divergences of eddy transports of zonal momentum and heat are both an order of magnitude smaller than their meridional counterparts, respectively. The meridional terms are plotted in Fig. 3 together with a linear least squares fit as a function of depth. A linear fit was used because the vertical structure in the values is thought to be mostly noise (Bryden and Brady, 1989).

Mangum and Hayes (1984) estimated the mean zonal pressure gradient force between 110°W and 152°W from the Equatorial Pacific Ocean Climate Studies (EPOCS) and North Pacific Experiment (NORPAX) hydrographic data for the 1979 to 1981 period. The zonal pressure gradient has a value of $P_\circ = -\rho_\circ^{-1}\partial\overline{P}/\partial x|_{z=0} = 4.5 \times 10^{-7}\,\mathrm{m\,s^{-2}}$ at the surface and decreases to within two standard errors of zero at 200 m. The pressure gradient varies seasonally by a factor of 2 of the annual mean (Mangum and Hayes, 1984). Dillon *et al.* (1989) approximated the vertical profile with a Gaussian function

$$-\frac{1}{\rho_\circ}\frac{\partial\overline{P}}{\partial x} = P_\circ \exp[-(\frac{\tilde{z}}{h_p})^2] \tag{2.6}$$

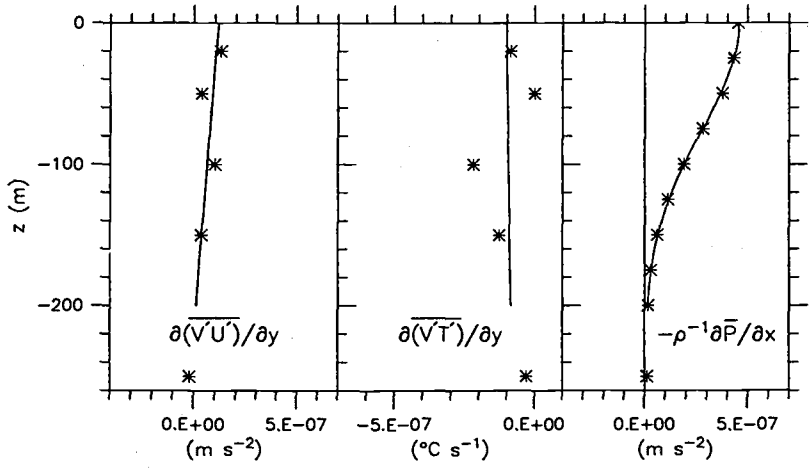

Figure 3. Long-term mean values of the meridional gradients of meridional eddy transports of zonal momentum and heat (Bryden and Brady, 1989) and zonal pressure gradient (Mangum and Hayes, 1984) at 0°N, 152°W. The observations are marked by symbols and the solid lines are linear fits for the eddy transport terms and a Gaussian function (2.6) for pressure.

where $P_\circ$ is the value of zonal pressure gradient at the surface; and h_p is the depth scale. A least squares fit to the mean zonal pressure gradient profile in Mangum and Hayes (1984) yields $P_\circ = 4.56 \times 10^{-7}\,\mathrm{m\,s^{-2}}$ and $h_p = 107\,\mathrm{m}$ (Fig. 3c). With these values we have $-\rho^{-1}\int_{-200}^{0} \partial\overline{P}/\partial x dz = 0.044\,\mathrm{N\,m^{-2}}$; *i.e.*, the vertically integrated zonal pressure gradient force is equivalent to a westerly wind stress of $0.044\,\mathrm{N\,m^{-2}}$, close to the wind stress of $0.05\,\mathrm{N\,m^{-2}}$ specified for this study.

Because vertical advection of momentum and heat is expected to be large at 0°N, 152°W, vertical velocity must be prescribed or estimated to balance the budgets. Observations and models (Wyrtki, 1981; Hansen and Paul, 1984, and 1987; Bryden and Brady, 1985, and 1989; Halpern and Freitag, 1987; Philander *et al.*, 1987; and Halpern *et al*, 1989) suggest that vertical velocity increases from zero at the surface to maximum values of order $10^{-5}\,\mathrm{m\,s^{-1}}$ at depths ranging between 50 and 100 m. In this paper, vertical velocity will be treated as an unknown variable and determined by the analysis described in the next section. The results, including comparison with previous estimates, are discussed in Section 2.4.

The magnitude of the terms, excepting the vertical turbulent transport, in the budget equations for momentum and heat (Eqs. 2.1 and 2.2) can be summarized. In the momentum equation, the terms $\overline{U}\partial\overline{U}/\partial x$, $\overline{W}\partial\overline{U}/\partial z$, $\partial\overline{V'U'}/\partial y$, and $-\rho_\circ^{-1}\partial\overline{P}/\partial x$ are all of order $10^{-7}\,\mathrm{m\,s^{-2}}$, and $\overline{V}\partial\overline{U}/\partial y$ and $\partial\overline{U'U'}/\partial x$, both of order $10^{-8}\,\mathrm{m\,s^{-2}}$. In the heat equation, the terms $\overline{U}\partial\overline{T}/\partial x$ and $\overline{W}\partial\overline{T}/\partial z$ are both of order $10^{-6}\,^\circ\mathrm{C\,s^{-1}}$, $\partial\overline{V'T'}/\partial y$, of order $10^{-7}\,^\circ\mathrm{C\,s^{-1}}$, and $\overline{V}\partial\overline{T}/\partial y$ and $\partial\overline{U'T'}/\partial x$, both of order $10^{-8}\,^\circ\mathrm{C\,s^{-1}}$.

2.3 Inverse analysis

In this section we describe the method used to determine vertical velocity, $\overline{W}$(z), and the turbulent fluxes, $\overline{F}_m$(z) and $\overline{F}_h$(z), which are approximated by

$$\overline{W}(z) = w_1 z + w_2 z^2 + w_3 z^3 \tag{2.7}$$

$$\overline{F}_m(z) = \rho_\circ \left(f_0 + f_1 z + f_2 z^2 + f_3 z^3 + f_4 z^4 \right) \tag{2.8}$$

$$\overline{F}_h(z) = \rho_\circ C_p \left(g_0 + g_1 z + g_2 z^2 + g_3 z^3 + g_4 z^4 \right). \tag{2.9}$$

where $\overline{W}$ is zero at the sea surface, and w_1, w_2, w_3, f_i, g_i, $i = 0, 1, \ldots, 4$, are thirteen unknown constants. The degrees of the polynomials were chosen *a posteriori* based on sensitivity studies (see Appendix).

We neglect terms at least an order of magnitude smaller than the leading terms, with one exception. From the previous section, we neglect $\overline{V}\partial\overline{U}/\partial y$ and $\partial\overline{U'U'}/\partial x$ in the momentum balance, and $\overline{V}\partial\overline{T}/\partial y$ and $\partial\overline{U'T'}/\partial x$, but not $\partial\overline{V'T'}/\partial y$, in the heat balance. We keep $\partial\overline{V'T'}/\partial y$ because it is a significant term in the surface mixed layer. Therefore, the long-term zonal momentum and heat balances at 0°N, 152°W, are approximated by

$$R_m(z) = \overline{U}\frac{\partial\overline{U}}{\partial x} + \overline{W}\frac{\partial\overline{U}}{\partial z} + \frac{\partial\overline{V'U'}}{\partial y} + \frac{1}{\rho_\circ}\frac{\partial\overline{F}_m}{\partial z} + \frac{1}{\rho_\circ}\frac{\partial\overline{P}}{\partial x} \tag{2.10}$$

$$R_h(z) = \overline{U}\frac{\partial\overline{T}}{\partial x} + \overline{W}\frac{\partial\overline{T}}{\partial z} + \frac{\partial\overline{V'T'}}{\partial y} + \frac{1}{\rho_\circ C_p}\frac{\partial\overline{F}_h}{\partial z} \tag{2.11}$$

where R_m and R_h are the imbalances, including errors and neglected terms.

We further constrain the problem with boundary conditions (surface and 200-m depth) and require that the turbulent diffusivities be finite and greater than or equal to a minimum background value:

$$\overline{F}_m = -\tau_x + R_\tau \qquad z = 0 \qquad (2.12)$$

$$\overline{F}_h = Q_{net} + R_Q \qquad z = 0 \qquad (2.13)$$

$$\overline{F}_m = 0 \qquad z = -h_{core} \qquad (2.14)$$

$$\frac{\partial \overline{F}_m}{\partial z} = 0 \qquad z = -200 \qquad (2.15)$$

$$\frac{\partial \overline{F}_h}{\partial z} = 0 \qquad z = -200 \qquad (2.16)$$

$$\overline{F}_m = -K_b \rho_\circ \frac{\partial \overline{U}}{\partial z} \qquad z = -200 \qquad (2.17)$$

$$\overline{F}_h = -K_b \rho_\circ C_p \frac{\partial \overline{T}}{\partial z} \qquad z = -200 \qquad (2.18)$$

$$\overline{K}_m = -\overline{F}_m \left(\rho_\circ \frac{\partial \overline{U}}{\partial z}\right)^{-1} \geq K_b \qquad -200 \leq z \leq 0 \qquad (2.19)$$

$$\overline{K}_h = -\overline{F}_h \left(\rho_\circ C_p \frac{\partial \overline{T}}{\partial z}\right)^{-1} \geq K_b \qquad -200 \leq z \leq 0 \qquad (2.20)$$

The value of background diffusivity is prescribed as $K_b = 10^{-5}\,\mathrm{m^2\,s^{-1}}$. Turbulence measurements yield a value either close to or smaller than $10^{-5}\,\mathrm{m^2\,s^{-1}}$ at a depth of 100 m (Peters *et al.*, 1988; Moum *et al.*, 1989). Sensitivity of the results to K_b is evaluated in the Appendix. The first condition specifies the turbulent momentum flux at the surface $\tau_x = -0.05\ \mathrm{N\,m^{-2}}$, plus an observational uncertainty, R_τ. The second condition specifies the turbulent heat flux at the surface $Q_{net} = -40\ \mathrm{W\,m^{-2}}$, plus an observational uncertainty, R_Q. The third is prescribed to keep $\overline{K}_m$ finite when evaluated at the depth of the EUC core, $h_{core} = 125\,\mathrm{m}$. The fourth and fifth boundary conditions require that convergences of vertical turbulent fluxes be zero at the lower bound. The sixth and seventh conditions specify the vertical turbulent fluxes at the lower boundary.

We now construct a linear system using the momentum and heat balance equations (2.10) and (2.11) and boundary conditions and other dynamical constraints in (2.12) through (2.20).

We obtain linear equations for the unknown coefficients by substituting the measured terms (discussed in the previous section) and the expressions for $\overline{W}$, $\overline{F}_m$ and $\overline{F}_h$ defined in (2.7), (2.8) and (2.9) into Eqs. (2.10) and (2.11) at the specified depths. We have observations of temperature at the 10 levels of 0, 10, 20, 30, 50, 75, 100, 125, 150, and 200-m from the Levitus atlas. We also have observations of currents at five levels of 20, 50, 100, 150, 250-m from Bryden and Brady (1989), an estimate of the zonal current from the neighboring Hawaii-Tahiti Shuttle Experiment at the 125-m level, and an extrapolated zonal velocity at the surface. We also use the values interpolated from the vertical profiles of zonal momentum terms obtained in the previous section at levels 10, 75 and 200 m in the momentum equation. Thus we have equations at each of 10 depths for the momentum and the heat balances. The method gives more weight to the upper layers where we have more observations.

The boundary conditions and dynamic constraints described by (2.12) through (2.18) give 7 linear equations when the expressions defined in (2.7), (2.8) and (2.9) are substituted for $\overline{W}$, $\overline{F}_m$ and $\overline{F}_h$.

The inequality conditions (2.19) and (2.20), requiring turbulent diffusivities, $\overline{K}_m$ and $\overline{K}_h$, to be greater than or equal to $K_b = 10^{-5}\,\mathrm{m^2\,s^{-1}}$, are applied at $z_j = j\Delta z$, $j = 0, 1, 2, \ldots, 40$, where $\Delta z = 5\,\mathrm{m}$. Thus we have 82 inequality constraints.

All equations of boundary conditions and inequality constraints are adjusted to have the same dimensions as the momentum or heat balance equations, by use of the constants ρ_o, $\rho_o C_p$, and/or a depth scale of $h_b = 200\,\mathrm{m}$ whenever needed.

In summary, we have obtained a system of 27 equality constraints and 82 inequality constraints for the 13 unknowns: w_1, w_2, w_3, f_i and g_i where $i = 0, 1, \ldots, 4$. We also multiply all equations of zonal momentum, including boundary conditions and other constraints on zonal momentum, by a weight $\lambda = 4$, to minimize the weighted sum of the momentum and the heat residuals. (Without the weighting, the minimization would be biased toward the heat balance.) Such a weighted linear system has a rank of 13, equal to the number of unknowns (see Appendix for tests of different weighting methods).

We apply the inverse analysis to the linear system constructed above. The technique employed to solve the linear least squares problem with both equality and inequality constraints is due to Lawson and Hanson (1974). The numerical algorithms developed by Haskell and Hanson (1981) and Hanson and Haskell (1982) are used. The method minimizes the weighted sum of residuals squared, $\lambda^2 \sum_{i=1}^{10} R_m(z_i)^2 + \sum_{i=1}^{10} R_h(z_i)^2 + \lambda^2 R_\tau^2 + R_Q^2$, where $z_i = 0$, -10, -20, -30, -50, -75, -100, -125, -150, and -200, for $i = 1, 2, \ldots, 10$. Solutions are obtained for the unknown coefficients, w_1, w_2, w_3, f_i and g_i, and hence $\overline{W}(z)$, $\overline{F}_m(z)$ and $\overline{F}_h(z)$. Turbulent transfer coefficients $\overline{K}_m$ and $\overline{K}_h$ are calculated according to (2.3) and (2.4), and the turbulent convergence terms, $-\rho_o{}^{-1}\partial\overline{F}_m/\partial z$ and $-(\rho_o C_p)^{-1}\partial\overline{F}_h/\partial z$, are computed.

2.4 Vertical velocity

The inverse solution for vertical velocity is close to a parabola, zero (specified) at the surface, a maximum of $2.7 \times 10^{-5}\,\mathrm{m\,s^{-1}}$ at a depth of 100 m and close to zero at 200 m (solid line, Fig. 4a and b). This estimate of vertical velocity falls within the range of previous estimates, a selection of which (Wyrtki, 1981; Hansen and Paul, 1984 and 1987; Bryden and Brady, 1985 and 1989; Halpern and Freitag, 1987; Philander *et al.*, 1987; and Halpern *et al*, 1989) is listed in Table 1 and plotted in Fig. 4a. The previous estimates of vertical velocity are based on data from satellite-tracked drifting buoys, CTD stations, moorings, historical atlas, and GCM results at longitudes from 80°W to 170°E and latitudes within 5 degrees from the equator. Time intervals for the data ranged from 3 months to multiple years, most free from El Niño episodes. The main difference between the previous observational estimates of $\overline{W}$ and the estimate from the inverse analysis is that the depths of the maxima of the previous estimates are consistently shallower than ours, approximately 50 m compared to our 100 m. The reason is that these previous estimates are all from observations east of 152°W where the thermocline and undercurrent are significantly shallower than at 152°W. The average longitude of the previous estimates is 127°W. Referring to Fig. 1, the top of the thermocline is about 100 m at 152°W and is at about 50 m at 127°W, consistent with the difference in depth of the maximum in $\overline{W}$ at the two locations. The largest of all the estimates of vertical velocity is from a general circulation model (Philander *et al.*, 1987) which yields an annual mean of $5.2 \times 10^{-5}\,\mathrm{m\,s^{-1}}$ at a depth of 50 m at 152°W.

Reference	Maximum ($\times 10^{-5} m/s$)	Depth of Maximum	Latitude Longitude	Time Interval	Data Source	Method
Wyrtki (1981)	1	50 m (specified)	5°S to 5°N 100°W to 170°E	Climatology	Atlas	Box model
Hansen and Paul (1984)	3	50 m (specified)	1.5°S to 1.5°N 100°W to 130°W	6/79 to 10/79	Drifting buoys	$\partial\overline{V}/\partial y$
Bryden and Brady (1985)	2.9	62 m	0.75°S to 0.75°N 110°W to 150°W	1/79 to 6/80 2/79 to 5/80	CTD stations	Box model
Hansen and Paul (1987)	1.7	50 m (specified)	1.5°S to 1.5°N 80°W to 130°W	11/77 to 6/82	Drifting buoys	$\partial\overline{V}/\partial y$
Halpern and Freitag (1987)	2.2	50 to 100 m	110°W	20 Jan to 24 Apr 79	Moorings	Continuity
Philander *et al.* (1987)	5.2	50 m	152°W	Annual mean	GCM	Numerical
Bryden and Brady (1989)	3.6	75 m	110°W to 152°W	1/79 to 10/81 4/79 to 6/80	Moorings	Continuity
Halpern *et al.* (1989)	2.5 2.0 2.2 1.9	25 to 125 m	134°W to 140°W 110°W to 140°W 124°W to 140°W 110°W to 140°W	1 Dec 83 to 31 Mar 84 1 May 84 to 30 Sept 84	Moorings	Continuity
This study	2.7	100 m	152°W	Climatology	Moorings and atlas	Inverse

Table 1. Previous and present estimates of maximum vertical velocity and the depth of the maximum in the equatorial mid-Pacific. As indicated, in some cases the depth of the maximum was specified. The location of each estimate is given under Latitude/Longitude. If no latitude is given, the location is on the equator. The box model method is based on conservation of momentum and heat within a box. The continuity method is based on integration of the continuity equation.

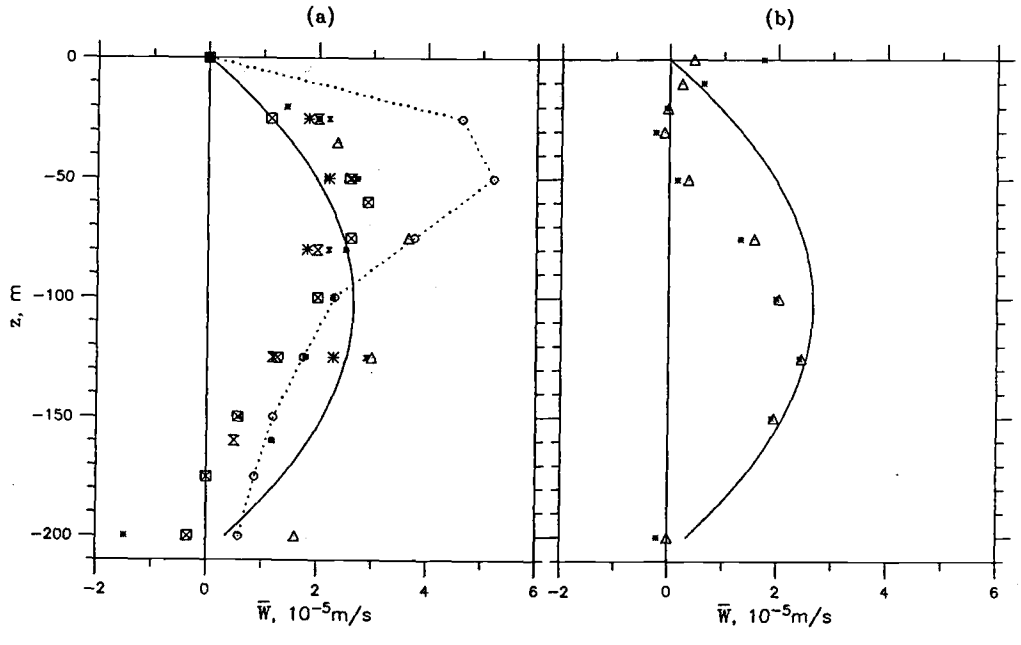

Figure 4. Equatorial vertical velocity *vs.* depth. Estimates of $\overline{W}$ (a) and (b) from the inverse analysis at 152°W (solid line), (a) from previous analyses (Wyrtki, 1981; Hansen and Paul, 1984 and 1987; Bryden and Brady, 1985 and 1989; Halpern and Freitag, 1987; Philander *et al.*, 1987; and Halpern *et al.*, 1989), and (b) from the product of zonal velocity and isotherm slope (triangles) and from the product of zonal velocity and isopycnal slope (asterisks). The dashed line in (a) is from the GCM result of Philander *et al.* (1987). See Table 1 for more information on the previous results.

If there is a balance between zonal and vertical advection of heat (terms 1 and 3 of Eq. 2.2), then flow will be parallel to isotherms and vertical velocity can be estimated from the product of the zonal velocity and the isotherm slope. This balance implies that the divergences of meridional advection, horizontal eddy transport and vertical turbulent transport are all negligible. There is a relatively deep, weakly-stratified, surface layer to the west of (0°N, 152°W), and an upward sloping thermocline and a shallowing surface layer to its east (Fig. 1b). Estimates of vertical velocity from the product of isotherm slope and zonal velocity are shown in Fig. 4b. Corresponding estimates based on isopycnal slope are also plotted. There is excellent agreement between these estimates and vertical velocity from the inverse analysis below 125 m; the difference in the upper 125 m is presumably caused by the divergence of turbulent heat transport and may be interpreted as a cross-isotherm or cross-isopycnal transport.

The sensitivity of the vertical velocity estimate to observational uncertainty and model assumptions was tested (see Appendix). If the vertical velocity is represented by a quadratic quadratic polynomial rather than a cubic (standard case), the solutions change negligibly. If a quartic representation is used, the solution for vertical velocity has a maximum of 2.8×10^{-5} m s^{-1} at a depth of 80 m. The estimate of vertical velocity is primarily determined by the heat balance and is therefore most sensitive to zonal velocity and to vertical and zonal gradients of temperature. When each of these is individually changed by ±50%, the maximum vertical velocity varies from 1.6 to 4.2×10^{-5} m s^{-1} and the depth of the maximum varies between 80 and 120 m.

2.5 Momentum balance

The terms [equation (2.10)] of the momentum balance, determined by the inverse method, are plotted *vs.* depth in Fig. 5. The dominant terms near the surface are the zonal pressure gradient and the vertical convergence of the turbulent zonal momentum flux. Both of these terms reach peak values in the upper 40 m and then decrease with depth to values of the same order as the residual below 150-m depth. The next largest term is vertical advection of zonal momentum which accelerates eastward flow above the undercurrent core and decelerates it below. The vertical advection term is zero at the surface, grows with depth and reaches a maximum at about 100-m depth, where it is also the dominant term. Below 125-m depth, the two dominant terms are zonal and vertical advection of zonal momentum, which mirror each other, both with extrema at about 145-m depth. Zonal advection of zonal momentum is also a significant term in the vicinity of 100-m depth where it reaches a negative peak. The meridional eddy transport term is the smallest of all of the terms and is only significant near the surface where its magnitude is about one-forth the magnitude of the zonal pressure gradient term. At 200-m depth, all terms are small, similar in magnitude to the residual.

The profile of turbulent stress convergence nearly mirrors that of the zonal pressure gradient. The 200-m integral of the turbulent stress convergence, $-0.048\,\mathrm{N\,m^{-2}}$, is close to both the specified wind stress, $-0.05\,\mathrm{N\,m^{-2}}$, and

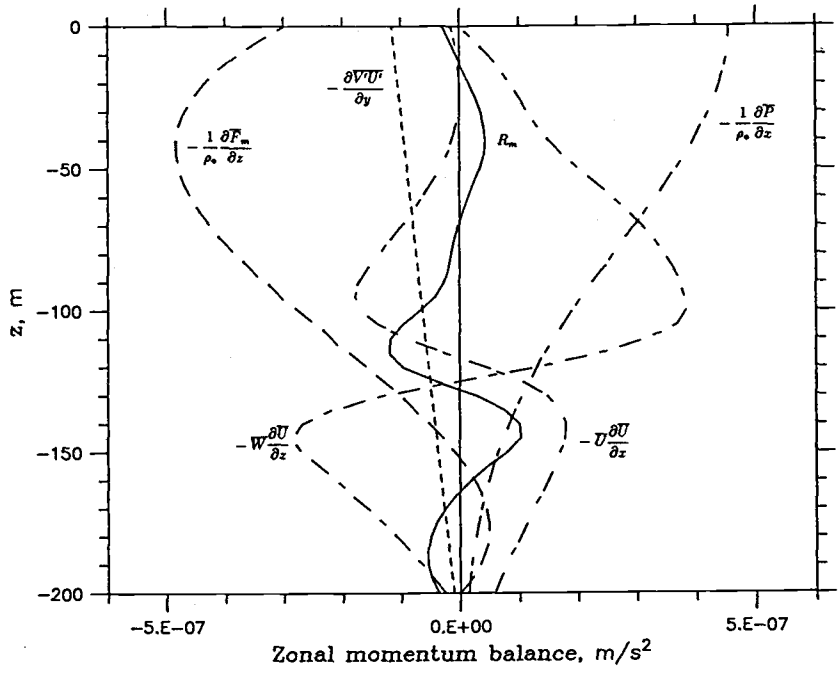

Figure 5. Terms in the long-term momentum balance (2.10) at 0°N, 152°W. Vertical velocity, $\overline{W}$, and the vertical turbulent momentum flux divergence, $-\rho^{-1}\partial\overline{F}_m/\partial z$, are from the inverse solution. All other variables are specified from observations. The residual, R_m, is shown as a solid line.

the 200-m integral of the zonal pressure gradient, $0.044\,\mathrm{N\,m^{-2}}$. The zonal pressure gradient is balanced by the wind stress which is vertically distributed by turbulent mixing.

The rms value of the residual term R_m is $0.5 \times 10^{-7}\,\mathrm{m\,s^{-2}}$, an order of magnitude smaller than the prevailing terms such as the zonal pressure gradient at the surface. The peaks in the residual (Fig. 5) between 100 and 150-m depth occur where some of the terms are changing rapidly with depth, which may indicate a lack of vertical resolution caused by the smoother polynomials in this analysis. The rms value justifies the neglect of the mean meridional advection and zonal eddy transport, both of order $10^{-8}\,\mathrm{m\,s^{-2}}$ (see Section 2.2).

In summary, the zonal pressure gradient is the primary force driving the eastward flow. Above the core of the EUC, the eastward zonal pressure gradient force and the upward advection of zonal momentum supplied by the EUC are balanced primarily by westward wind stress which is distributed vertically by turbulent mixing. Below the undercurrent core, zonal advection of zonal momentum tends to accelerate the flow and is balanced by vertical advection of zonal momentum.

2.6 Heat balance

The terms of the heat balance [equation (2.11)] are plotted as a function of depth in Fig. 6. Zonal and vertical advection are the dominant terms below 70 m, both of which have peaks at 135-m depth. This balance of terms is consistent with Section 2.4 where it was shown that along-isotherm

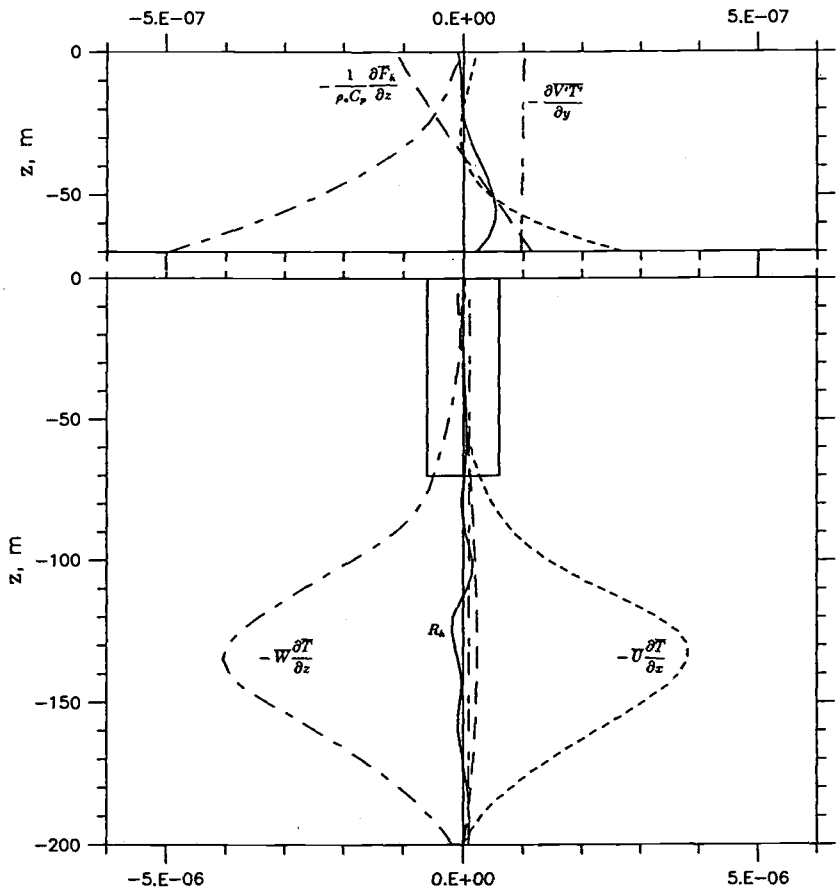

Figure 6. Terms in the long-term heat balance (2.11) at 0°N, 152°W. Vertical velocity, $\overline{W}$, and the vertical turbulent heat flux divergence, $-(\rho C_p)^{-1}\partial\overline{F}_h/\partial z$, are from the inverse solution. All other variables are specified from observations. The residual, R_h, is shown as a solid line. The upper panel shows the upper 70 m with the horizontal scale expanded by a factor of ten.

flow below 100-m depth agrees with estimates of vertical velocity from the inverse analysis. Even though small compared to the advection terms, the vertical turbulent transport divergence is larger than the peaks in the residual throughout most of the region below 70 m and is significantly larger than the rms residual. All terms are small at 200-m depth, similar in magnitude to the residual.

The heat balance in the upper 70 m is more complex than below (Fig. 6, upper panel). Zonal and vertical advection, vertical turbulent transport, and zonal eddy transport are all significant. Vertical advection of heat decreases to zero at the surface but is still the largest term below 40 m. Horizontal advection of heat is close to zero in the upper 50 m and increases rapidly below that depth. Vertical turbulent transport divergence is approximately linear, a cooling term above 40-m depth and a heating term below. The horizontal eddy transport term is a nearly constant heating term which approximately balances the vertical turbulent transport divergence at the surface. Mesoscale eddies transport heat to the cold tongue at the equator.

The rms value of the residual, R_h, is 0.8×10^{-7} °C s^{-1}, 1/50 the peak values of zonal and vertical advection. This justifies the neglect (Section 2.2) of the zonal eddy heat transport and the mean meridional advection, both of order 10^{-8} °C s^{-1}.

2.7 Turbulent fluxes

The inverse solution for the mean vertical turbulent flux of zonal momentum is shown in Fig. 7a. The solution for turbulent momentum flux at the surface is $0.048\,\mathrm{N\,m^{-2}}$, compared to the prescribed mean wind stress of $-0.05\,\mathrm{N\,m^{-2}}$. The difference, $0.002\,\mathrm{N\,m^{-2}}$, is the residual in (2.12) is. It falls well within the range of error estimates by Wyrtki and Meyers (1976) and Hellerman and Rosenstein (1983) as discussed in Section 2.2. The turbulent momentum flux decrease is approximately linear in the upper 80 m and it falls more rapidly below, equal to zero at the depth of maximum zonal velocity, as is required to keep the turbulent viscosity finite. The flux has values smaller than $0.002\,\mathrm{N\,m^{-2}}$ below the core.

The difference between the solid and dashed lines in Fig. 7a represents the misfit of the vertical turbulent flux of zonal momentum. The dashed line is the integral solution of the turbulent flux when the residual $R_m(z)$ is added to the solution for the vertical convergence of the turbulent flux of zonal momentum, and the flux is still required to be zero at the velocity maximum. The rms value of the difference between the solid and dashed lines is $0.002\,\mathrm{N\,m^{-2}}$. The turbulent flux is distinguishable from zero above the undercurrent core, but not below.

The inverse solution for the mean vertical turbulent flux of heat is shown in Fig. 7b. The turbulent heat flux is $-97\,\mathrm{W\,m^{-2}}$ at the surface, reaches a peak value of $-106\,\mathrm{W\,m^{-2}}$ at 35 m, and decreases to $-2\,\mathrm{W\,m^{-2}}$ at 200 m. The ocean gains heat at the surface and turbulent mixing carries it downward throughout the 200-m water column.

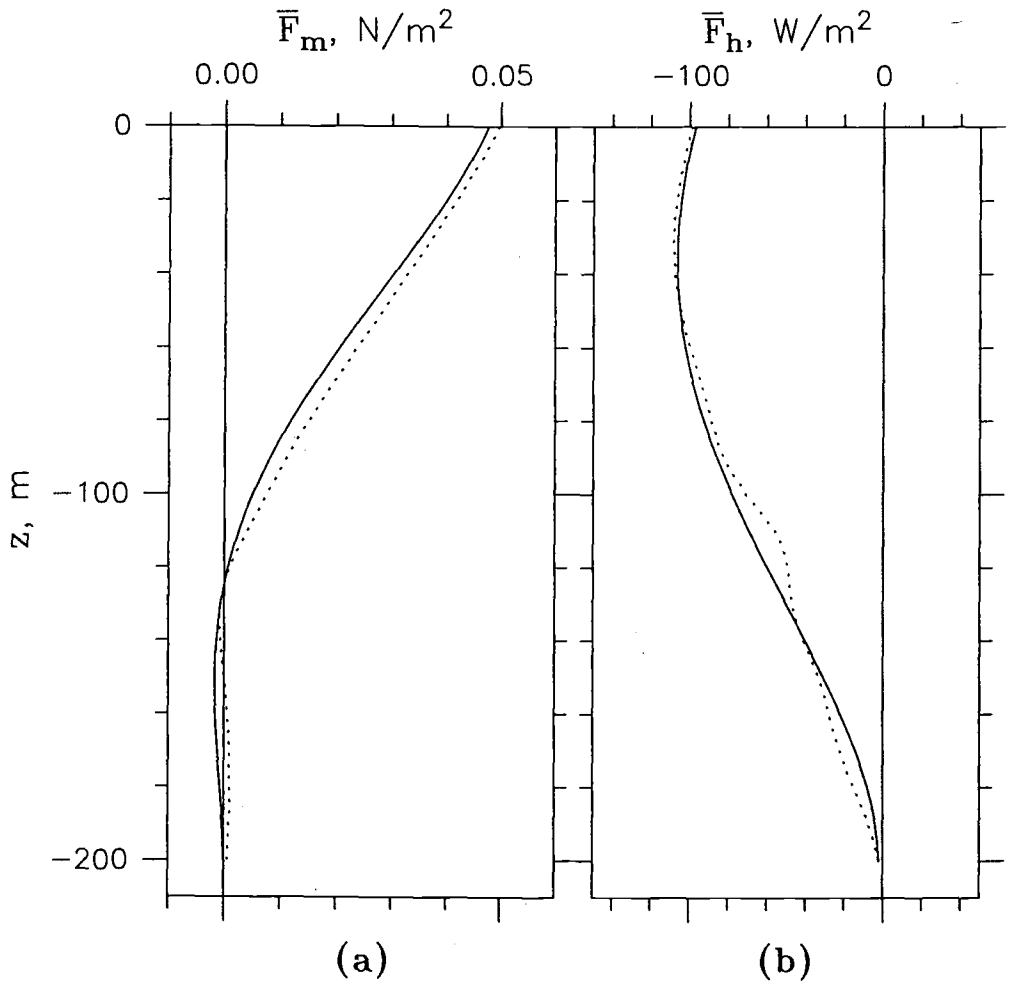

Figure 7. Inverse solutions for (a) vertical turbulent flux of zonal momentum $\overline{F}_m(z)$ and (b) vertical turbulent flux of heat $\overline{F}_h(z)$ at 0°N, 152°W. The dashed lines are the solutions of (2.10) and (2.11) with the residuals, $R_m(z)$ and $R_h(z)$, set to zero and with $\overline{W}(z)$ specified from the inverse solution (Fig. 4).

The inverse solution for the surface heat flux, $97\,\mathrm{W\,m^{-2}}$, is more than twice as large as the prescribed $40\,\mathrm{W\,m^{-2}}$ at the surface, but not much above the 95% confidence interval of $\pm 50\,\mathrm{W\,m^{-2}}$ for the prescribed value from the atlases (Weare *et al.*, 1981; Esbensen and Kushnir, 1981) as discussed in Section 2.2. The larger value for the surface heat flux is plausible. The value ($40\,\mathrm{W\,m^{-2}}$) from the atlases is based on contours drawn to averages over squares of more than five degrees at latitude intervals beginning on the equator. Hence the estimates on the equator may be biased toward lower values because of higher cloud cover to the north and south associated with the intertropical convergence. In other words, the smoothed estimates of heat flux from the atlases may be biased toward low values because of failure to resolve a maximum on the equator. A higher value is also supported by shipborne measurements during Tropic Heat 1984. The average heat flux at 140°W from 19 November to 1 December 1984 was $115\,\mathrm{W\,m^{-2}}$ (also net heating). Furthermore, as will be seen in the next section, a surface heat flux in the vicinity of $100\,\mathrm{W\,m^{-2}}$ is consistent with the turbulent thermal diffusivity and the turbulent viscosity being approximately equal near the surface.

The difference between the solid and dashed lines in Fig. 7b represents the misfit of the inverse solution for the turbulent heat flux. The dashed line is obtained by adding the residual, R_h, in the heat balance equation (2.11) to the vertical turbulent heat flux divergence and integrating with the same boundary conditions (2.18) at 200 m. The rms value of the misfit is $5\,\mathrm{W\,m^{-2}}$.

The sensitivity of the turbulent momentum and heat fluxes to variations in specified parameters and observations is given in the Appendix. The turbulent momentum flux is relatively insensitive to variations in observations and parameters. As might be expected, the largest changes in turbulent momentum flux occur in response to $\pm 50\%$ changes in the specified pressure gradient and the vertical profile of zonal velocity. Except in the upper 70 m the turbulent heat flux divergence term is small compared to zonal and vertical advection of heat and the turbulent heat flux is therefore sensitive to several parameters and observations. The dominant factors are background diffusivity, vertical and horizontal temperature gradients and the vertical gradient of zonal velocity.

2.8 Turbulent diffusivities

The inverse solutions for the turbulent diffusivities for momentum and heat, $\overline{K}_m$ and $\overline{K}_h$, are plotted as a function of depth in Fig. 8. Both diffusivities have values of $4.7 \times 10^{-3}\,\mathrm{m^2\,s^{-1}}$ at the surface and, apart from an unrealistic and insignificant subsurface maximum in $\overline{K}_h$, decrease to approximately 1×10^{-3} at 80-m depth and to 1×10^{-4} at 120-m depth. The ratio, $\overline{K}_m/\overline{K}_h$ varies between 0.7 and 1.3 in the upper 120 m. The misfits in the solutions for $\overline{K}_m$ and $\overline{K}_h$ were evaluated from the corresponding misfits for the turbulent fluxes (see Section 2.7) and are plotted in Fig. 8. The rms values of the misfits are $2 \times 10^{-4}\,\mathrm{m^2\,s^{-1}}$ and $0.5 \times 10^{-4}\,\mathrm{m^2\,s^{-1}}$ for $\overline{K}_m$ and $\overline{K}_h$, respectively. Tests of the sensitivity of the solutions for $\overline{K}_m$ and $\overline{K}_h$ to variations in specified parameters and observations is given in the Appendix.

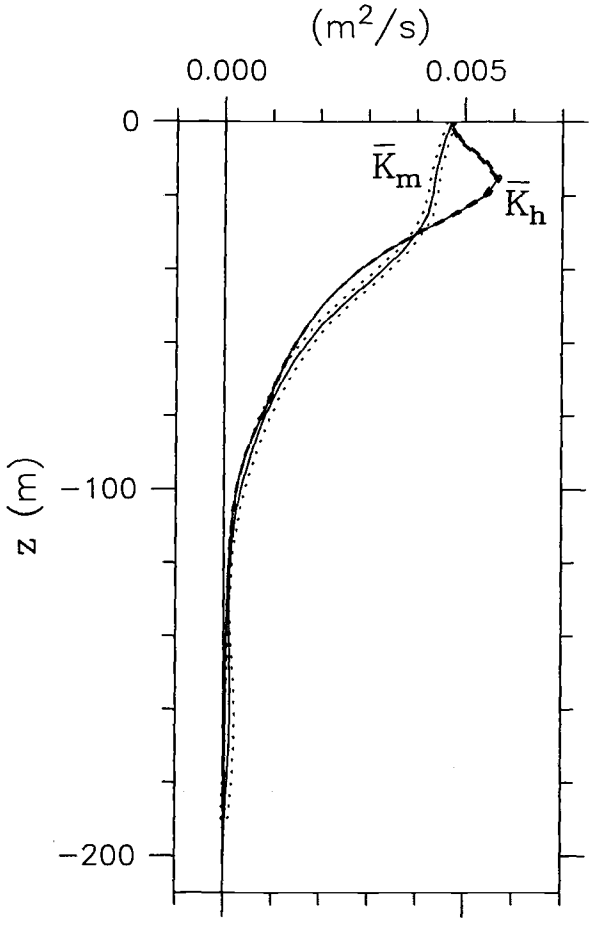

Figure 8. Turbulent diffusivities, $\overline{K}_m$ and $\overline{K}_h$, from the inverse solutions for the turbulent momentum and heat fluxes (Fig. 7). The dashed lines correspond to the ± the difference between the solid and dashed lines in Fig. 7, i.e., they result from assigning the residual to the turbulent flux convergence terms in the momentum and heat balance equations.

The similarity in the profiles of $\overline{K}_m$ and $\overline{K}_h$ suggest that turbulent transfer mechanisms for momentum and heat are similar. One expects $\overline{K}_m \leq \overline{K}_h$ because pressure forces may act to transfer momentum with no effect on the transfer of heat. The present estimate of $\overline{K}_h$ may be considered an upper bound because the uncertainty in $\overline{K}_h$ is larger than $\overline{K}_m$ (see discussion in previous section on the uncertainty in the turbulent fluxes).

The surface values of $\overline{K}_m$ and $\overline{K}_h$ are consistent with values predicted for a constant-stress log layer at the surface. Given the specified wind stress of $0.05\,\mathrm{N\,m^{-2}}$, the log-layer estimate of $\overline{K}_m$ $(= \kappa u_* z)$ is $4.7 \times 10^{-3}\,\mathrm{m^2\,s^{-1}}$ at a depth of 1.7 m. This depth is within the range (1.5 to 2.0 m) obtained in Section 2.2 for matching a log layer to velocity profiles linearly extrapolated from 10 and 20-m depths. This depth also fall within estimated range of the Monin-Obukhov length. Estimates of surface buoyancy flux from both Tropic Heat 84 and 87 are of order $1 \times 10^{-7}\,\mathrm{m^3\,s^{-2}}$ (Moum *et al.*, 1989; Hebert *et al.*, 1991). The Monin-Obukhov length has values of 0.7, 3.5 and 11 m for wind stress of 0.02, 0.05 and $0.10\,\mathrm{N\,m^{-2}}$, respectively.

Microstructure measurements were carried out as part of the Tropic Heat experiment, during which one ship occupied an equatorial station near 140°W from 19 November to 1 December 1984 (Moum and Caldwell, 1985), and another ship occupied a station a few tens of kilometers distant from 25 to 30 November (Gregg *et al.*, 1985). The average wind stress during the experiment was $-0.10\,\mathrm{N\,m^{-2}}$, two times the magnitude of its long-term average. The average net surface heat flux was $-115\,\mathrm{W\,m^{-2}}$, not much different from the estimate of $-97\,\mathrm{W\,m^{-2}}$ from the inverse analysis.

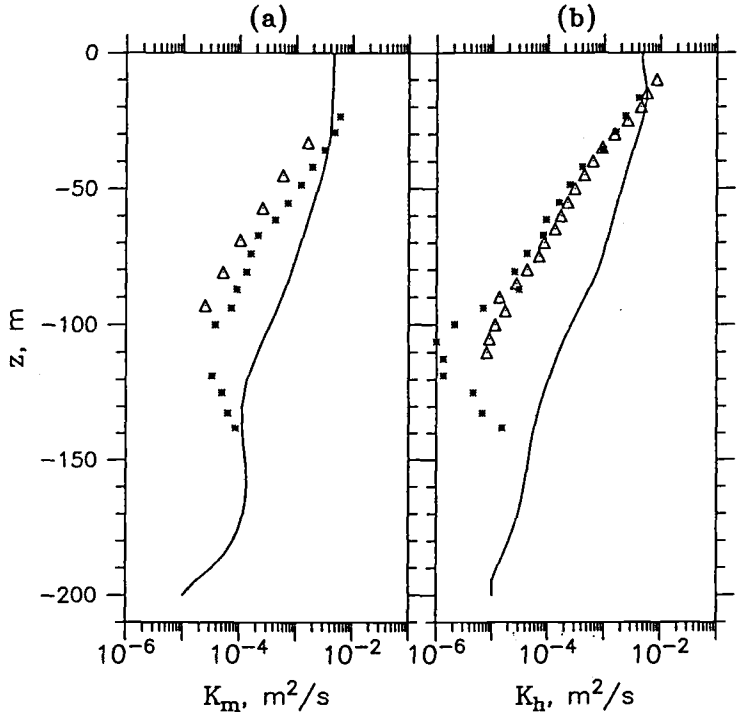

Figure 9. Inverse solutions (solid lines) and estimates based on observations of dissipation during Tropic Heat 84 for (a) turbulent viscosity, K_m, and (b) turbulent diffusivity for heat, K_h. Estimates in (a) and (b) from Peters *et al.* (1988) are marked by asterisks. Estimates of K_m in (a) from Dillon *et al.* (1989) and of K_h in (b) by Moum *et al.* (1989) are marked by triangles.

Peters *et al.* (1988) and Dillon *et al.* (1989) estimated $\overline{K}_m$ from the Topic Heat 84 observations by use of the dissipation method. Estimates of $\overline{K}_m$ as a function of depth are plotted in Fig. 9a. In the dissipation method it is assumed that the rate of mechanical production of turbulent kinetic energy (TKE) equals the rate of dissipation. Buoyancy production and turbulent transport divergence of TKE are neglected. Peters *et al.* (1988) also included the meridional contribution to the total shear (which accounts for 25% at maximum), while Dillon *et al.* (1989) did not. The dissipation estimates of $\overline{K}_m$ from the two sets of measurements agree with each other within a factor of two. The dissipation estimates are in good agreement with the inverse solution in the vicinity of 30 m, but the estimates diverge with increasing depth. The dissipation estimates of $\overline{K}_m$ are about an order of magnitude smaller than the inverse solution at a depth of 90 m.

Peters *et al.* (1988) and Moum *et al.* (1989) estimated $\overline{K}_h$ (Fig. 9b) from the Tropic Heat 84 data. Peters *et al.* used the Osborn-Cox (Osborn and Cox, 1972) method which is based on the assumption that for steady and laterally homogeneous turbulent flow, the rate of production of temperature variance is balanced by the rate of destruction by molecular conduction. Moum *et al.* (1989) estimated $\overline{K}_h$ by use of the method described by Osborn (1980) which does not use measurements of the dissipation rate of temperature variance:

$$\overline{K}_h = 0.2\varepsilon/N^2$$

where ε is the rate of dissipation of turbulent kinetic energy and N is the buoyancy frequency. The primary assumptions used to derive the above empirical formula were (1) that the TKE equation is simplified with the rate

of mechanical production being balanced by the rate of buoyancy destruction and the rate of molecular dissipation, and (2) that the mixing of mass and heat can be represented by a single turbulent diffusivity. The estimates of $\overline{K}_h$ from the two sets of observations and by two different methods agree well with each other in the upper 90 m. The dissipation estimates agree with the inverse analysis estimates at a depth of 15 m, but differ increasingly with depth; the dissipation estimates are more than an order of magnitude less than the inverse estimates at a depth of 80 m.

The reasons for the difference between the dissipation and inverse estimates of $\overline{K}_m$ and $\overline{K}_h$ are uncertain. One might expect that the estimates from the Tropic Heat 84 observations would be higher than the inverse solution because the wind stress was about twice as large during Tropic Heat 84 as the long-term mean. In a surface log layer, $\overline{K}_m$ is proportional to the square root of the wind stress, so one would expect $\overline{K}_m$ from Tropic Heat 84 to be 40% larger than the long-term mean, at least near the surface. The uppermost dissipation estimates of $\overline{K}_m$ by Peters *et al.* (1988) are larger than the inverse values and the same is true for the uppermost estimates of $\overline{K}_m$ by Dillon *et al.* (1989). However, the difference between the dissipation and inverse estimates increases with depth with the dissipation estimates about an order of magnitude less than the inverse estimates at a depth of 80 m. As suggested by Dillon *et al.* (1989), the dissipation estimates might underestimate $\overline{K}_m$ because they do not take into account momentum transfer by pressure forces associated with internal waves (e.g., Wijesekera and Dillon, 1991). However, pressure forces do not play a role in the transport of heat, so there must be another reason for the discrepancy between the estimates of

$\overline{K}_h$ by the inverse and dissipation methods. One possible reason is potential error in the inverse estimate of $\overline{K}_m$. Uncertainties in the estimate of $\overline{K}_h$ by the inverse method are larger than for $\overline{K}_m$ because the vertical turbulent heat transport divergence term is small compared to the leading horizontal and vertical advection terms below 70-m depth. The dissipation estimates of $\overline{K}_m$ and $\overline{K}_h$ may also be in error. The dissipation estimate of $\overline{K}_m$ is based on an approximate TKE budget which neglects the buoyancy production/destruction term. Neglect of this term for stably stratified conditions could result in an underestimate of $\overline{K}_m$ by about 25% (Osborn, 1980; Rohr and Van Atta, 1987), not nearly enough to explain the order of magnitude difference. In summary, a plausible explanation for the difference between the dissipation and inverse estimates of $\overline{K}_m$ is the neglect in the dissipation method of momentum transport by pressure fluctuations associated with internal waves. An explanation for the difference in dissipation and inverse estimates of $\overline{K}_h$ is lacking, but uncertainty in the estimates is a possibility.

Values of $\overline{K}_m$ from our analysis are consistent with one of the conclusions in Dillon *et al.* (1989), who were unable to balance a zonal momentum budget using their estimates of turbulent stresses, together with the zonal pressure gradient, zonal and vertical advection of zonal momentum from Bryden and Brady (1985), and eddy transport from Bryden and Brady (1989). To balance the system, turbulent viscosities were required to be an order of magnitude larger than those they calculated from the measurements. As discussed above, the values of $\overline{K}_m$ we obtained are an order of magnitude larger than the estimates in Dillon *et al.* (1989) between 70 and 100 m.

2.9 Richardson number

The gradient Richardson number was calculated and is shown in Fig. 10. In the long-term mean steady state, the vertical shear is mainly due to the mean zonal flow rather than the mean meridional flow, and the vertical density gradient is due to temperature rather than salinity (Wyrtki and Kilonsky, 1984). Thus, we approximate the gradient Richardson number R_g as

$$R_g(z) = -\frac{g}{\rho_\circ}\frac{\partial\rho/\partial z}{(\partial U/\partial z)^2} \tag{2.21}$$

where g is the gravitational acceleration, and $\rho(z) = \rho_\circ[1 + \alpha(T - T_\circ)]$. The gradient Richardson number is below 0.5 in the upper 80 m, reaches a maximum at the EUC core, and is about 2.0 between 150 and 200-m depth.

The low values of R_g in the upper 80 m suggest that mixing there may be controlled by critical Richardson number dynamics. The Richardson number is often interpreted as an index to turbulent mixing due to Kelvin-Helmholtz instabilities of a stratified shear flow. Instability occurs when the Richardson number falls below the critical value $R_c = 0.25$ (Miles and Howard, 1964).

Measurements over a period of a few seeks during Tropic Heat 84 also showed that R_g was near critical in the upper 80 m (Fig. 10), a short term result comparable to the long-term results presented here. We calculated the overall averaged Richardson number using the density estimates from the rapid sampling vertical profiler (RSVP) and the acoustic Doppler current profiler (ADCP) shears collected at 140°W on R/V *Wecoma* during Tropic Heat 84 (Chereskin *et al.*, 1986) and the results show values between 0.2 and 0.5 above 90 m (dashes, Fig. 10). Peters *et al.* (1988) found similar results

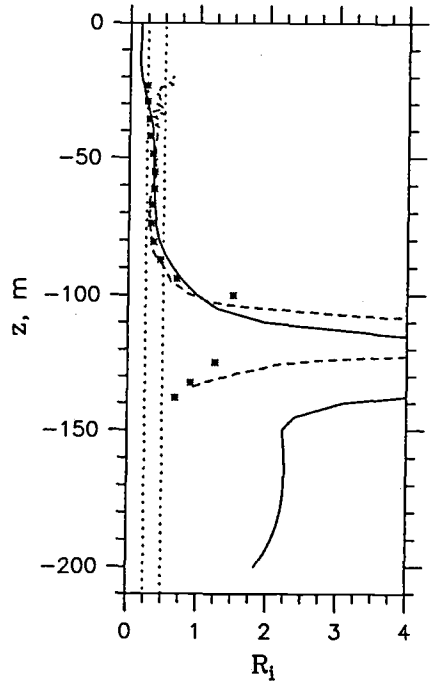

Figure 10. Gradient Richardson number from the inverse analysis (solid line) and from observations at 0°N, 140°W during Tropic Heat 84. The asterisks mark data from Peters *et al.* (1988). The dashed line is calculation from the data collected by R/V *Wecoma* described in Chereskin *et al.* (1986). The dotted lines indicate values of 0.25 and 0.50.

(asterisks, Fig. 10). Chereskin *et al.* (1986) estimated the hourly averaged Richardson number on 12-m vertical scales and found that about 75% of the values above 90 m fell between 0.2 and 0.5. Chereskin *et al.* (1986) also noted that Richardson numbers were very sensitive to the scales over which they were calculated and to the types of averaging techniques applied.

2.10 Conclusions

An inverse analysis has been applied to long-term observations in the upper 250 m of the equatorial Pacific at 152°W. The observations (Figs. 2 and 3) included zonal velocity, temperature, pressure gradient, and surface fluxes of momentum and heat. The analysis was subject to constraints (equations 2.7–2.20) which included conservation of heat and zonal momentum, boundary conditions at 200-m depth, and turbulent diffusivities greater than a background value. The analysis yielded vertical profiles in the upper 200 m of: 1) vertical velocity, 2) terms in the heat and zonal momentum balances, 3) vertical turbulent transports of momentum and heat, and 4) turbulent diffusivities for momentum and heat. Estimates of the surface fluxes of momentum and heat were also obtained.

The estimate of vertical velocity *vs.* depth (Fig. 4) is close to parabolic, zero at the surface, increasing to a maximum value of $2.7 \times 10^{-5}\,\mathrm{m\,s^{-1}}$ at a depth of 100 m and decreasing to $0.3 \times 10^{-5}\,\mathrm{m\,s^{-1}}$ at 200 m. In the region from 125 to 200-m depth, vertical velocity is equal to the product of zonal velocity and isotherm slope; i.e., the flow is along isothermal (or isopycnal) surfaces in this region. There is significant cross-isotherm flow above 125 m.

Our estimate of vertical velocity is in good agreement with the mean of previous observational estimates when allowance is made for variation with longitude of the depth of the maximum. This variation is associated with the shallowing of the thermocline and the EUC toward the east from 152°W. Our results are in poor agreement with a general circulation model (Philander *et al.*, 1987) which yields a maximum of 5.2×10^{-5} m s^{-1} at a depth of 50 m at 152°W.

The zonal momentum balance (Fig. 5) in the high shear zone above the EUC core (0 to 130 m) at 152°W is dominated by the zonal pressure gradient force, the vertical turbulent transport divergence and vertical advection, with a small but significant additional contribution from horizontal advection. Below the EUC core (130 to 200 m) the dominant terms are vertical and horizontal advection. All terms are insignificant compared to the residual at 200-m depth. The integral of the zonal pressure gradient in the upper 200 m is close to the wind stress.

The heat balance (Fig. 6) between 70 and 200 m depth is dominated by zonal and vertical advection. In the upper 70 m, vertical turbulent heat transport divergence and the divergence of meridional eddy transport of heat are also important terms in the heat balance; the vertical and horizontal advection terms decrease to zero and near zero respectively as the surface is approached.

The inverse analysis yielded estimates of the turbulent fluxes of momentum and heat as a function of depth (Fig. 7). The estimated turbulent momentum flux is 0.048 N m^{-2} at the surface and decreases approximately linearly to 0.012 N m^{-2} at a depth of 80 m. The estimated surface momentum

flux is close to the value $0.050\,\mathrm{N\,m^{-2}}$ (Wyrtki and Meyers, 1976) prescribed for the inverse analysis. The turbulent heat flux is $97\,\mathrm{W\,m^{-2}}$ at the surface and is approximately constant in the upper 80 m. The estimated turbulent heat flux is $95\,\mathrm{W\,m^{-2}}$ at a depth of 80 m and decreases approximately linearly with depth to $16\,\mathrm{W\,m^{-2}}$ at 170 m. The estimated surface heat flux is more than twice as large as the $40\,\mathrm{W\,m^{-2}}$ (Weare et al., 1981; Esbensen and Kushnir, 1981) prescribed from the inverse analysis. The larger value is plausible because the Weare et al. and Esbensen and Kushnir estimates are based on averages over horizontal grids of approximately 5° longitude by 5° latitude (centered off the equator) on either side of the equator which would include regions of higher cloudiness and lower heating than on the equator. Our surface heat flux estimate is however sensitive to prescribed background diffusivity. A reduction of the prescribed background diffusivity from 10^{-5} to $10^{-6}\,\mathrm{m^2\,s^{-1}}$ reduces the estimated surface heat flux to $45\,\mathrm{W\,m^{-2}}$.

Turbulent diffusivities for momentum and heat, $\overline{K}_m$ and $\overline{K}_h$, were estimated as functions of depth (Fig. 8). Apart from an unrealistic subsurface maximum in $\overline{K}_h$ at 16 m, the two diffusivities are similar with surface values of $0.0047\,\mathrm{m^2\,s^{-1}}$ which decrease to $0.0010\,\mathrm{m^2\,s^{-1}}$ at a depth of 80 m. The surface estimates are consistent with near-surface log-layer estimates. Our estimates may be compared with estimates of $\overline{K}_m$ and $\overline{K}_h$ based on observations of the dissipations of turbulent kinetic energy and temperature variance (Fig. 9; Peters *et al.*, 1988; Dillon *et al.*, 1989; Moum *et al.*, 1989). Our estimates are close to the dissipation estimates near the surface. However the dissipation estimates decrease more rapidly with depth than our estimates and are approximately an order of magnitude less at a depth of 80 m. One

possible reason for the difference in estimates of $\overline{K}_m$ is that pressure fluctuations associated with internal waves may be important for transferring momentum (Dillon *et al.*, 1989). However this cannot explain the reason for the discrepancy between our estimates and the dissipation estimates of $\overline{K}_h$.

Gradient Richardson number computed from the long-term observations is less than 0.5 in the upper 80 m (Fig. 10). This result agrees with short-term observations near 140°W (Chereskin *et al.*, 1986; Peters *et al.*, 1988) and suggests that turbulent mixing in the upper 80 m may be due to Kelvin-Helmholtz instabilities generated when the Richardson number falls below a critical value.

Chapter 3

A Critical-R_i Model of Turbulent Mixing Applied to the the Upper Equatorial Pacific Ocean

Abstract

We applied a critical-R_i model of turbulence to simulate the turbulent mixing in the upper equatorial Pacific Ocean at 152°W, where the gradient Richardson number had values near-critical in the upper 80 m. The model is based on that of Price *et al.* (1986), but excludes the bulk Richardson number mixing. It was run with constant forcing and boundary conditions based on the inverse analysis of the long-term steady-state balances of zonal momentum and heat by Luan *et al.* (1993a).

The modeled steady-state velocity, temperature, turbulent fluxes and diffusivities are consistent with those of the inverse analysis. Strong transient behavior of the model with a time scale of 100 days due to vertical advection underscores the importance of spin-up of the turbulence model before investigating the effects of time-varying surface forcing. Varying the critical and the post-mixing values of gradient Richardson numbers in the model has

significant effects on the modeled steady states, although those of the latter were relatively small. The model (with constant forcing) shows a mixing barrier at the undercurrent core.

The model uses only a local gradient Richardson number criterion to parameterize mixing. A test of the model including the criterion of bulk Richardson number distorts turbulent mixing. Such a model yields larger and more intense mixing events, smaller mean vertical gradients and highly intermittent time series of modeled velocity and temperature near the surface even though all forcing terms are time-independent.

3.1 Introduction

A recent study (Luan *et al.*, 1993a) of the long-term budgets of zonal momentum and heat at 152°W on the equator showed that gradient Richardson number is close to its critical value of 0.25 in the upper 80 meters. The flow in the upper 100 m is strongly sheared vertically with a weak thermocline, and is bounded by a maximum in the equatorial undercurrent (EUC) and a strong thermocline (Fig. 11) (Knox and Halpern, 1982; Gregg *et al.*, 1985; Moum and Caldwell, 1985; Bryden and Brady, 1989). The upper equatorial Pacific shows a classic case of turbulent mixing due to shear instabilities, which is stronger and more persistent than usually found at higher latitudes.

A one-dimensional, time-dependent, critical-R_i model may be used to study turbulent mixing in the upper equatorial Pacific, because the observed gradient Richardson number is near-critical. Price *et al.* (1986) used a simple one-dimensional model of turbulence based on the critical Richardson number

to simulate diurnal cycles of turbulent mixing at mid-latitudes. Schudlich and Price (1991) used the same critical-R_i model to simulate the diurnal cycle of mixing in the equatorial Pacific. Our goals in this paper are: 1) to simplify the model of Price *et al.* (1986), 2) to use the simplied model to simulate steady-state mixing in the upper equatorial Pacific, 3) to test the sensitivity of the model to initial conditions, forcing, and mixing parameterizations, and 4) to determine conditions for numerical stability. The simplified critical-R_i model is used in Luan *et al.* (1993c) to simulate the diurnal cycle of mixing in the upper equatorial Pacific Ocean.

3.2 Long-term momentum and heat balances

Simulation of one-dimensional, steady-state turbulent mixing in the upper equatorial Pacific requires specification of boundary conditions and non-turbulence components of the momentum and heat balances. In this section we summarize the boundary conditions and balances which are used as a test-bed for the critical-R_i turbulence model described in the next section.

Luan *et al.* (1993a) concluded that in the upper 200 meters at 0°N, 152°W, the zonal momentum balance is dominated by the pressure gradient force, mean zonal and vertical advection, meridional eddy transport, and vertical turbulent diffusion. The heat balance is dominated by zonal and vertical advection, and, in the upper 30 m, by meridional eddy transport and vertical turbulent diffusion. The corresponding equations of zonal momentum and heat balances are:

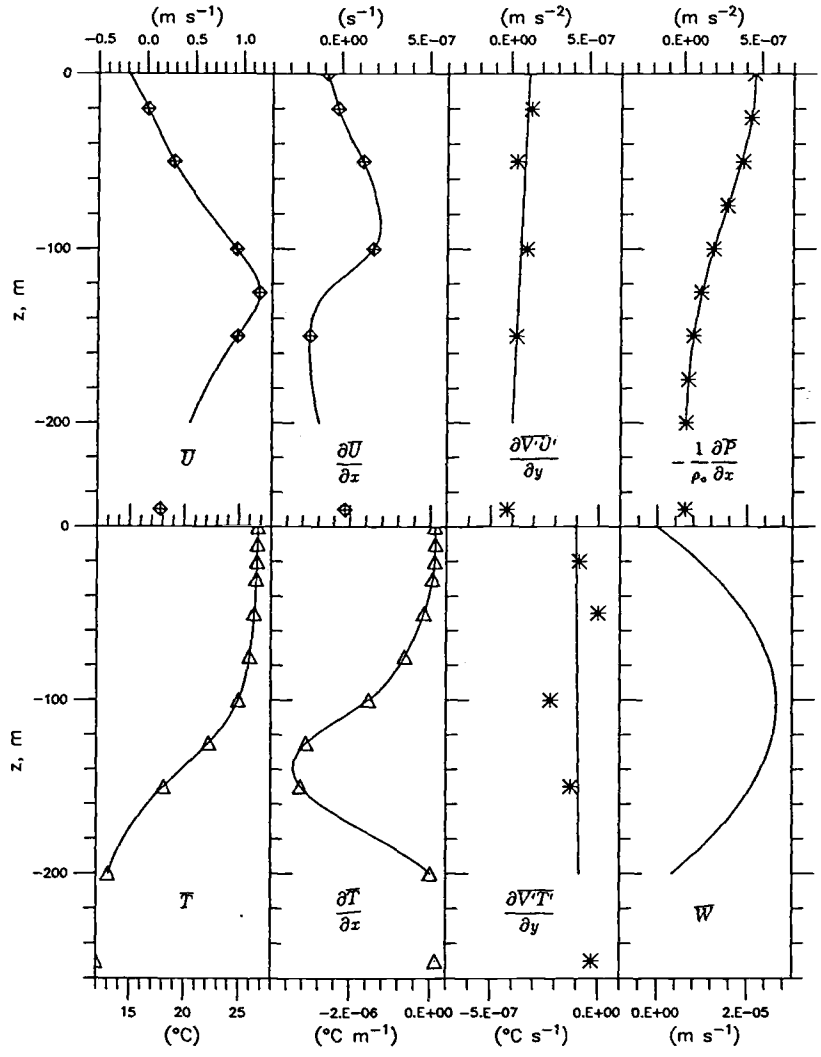

Figure 11. Long-term mean zonal velocity $\overline{U}$ and its zonal gradient $\frac{\partial \overline{U}}{\partial x}$, temperature, $\overline{T}$, its zonal gradient, $\partial \overline{T}/\partial x$, meridional eddy transports of zonal momentum, $\partial \overline{V'U'}/\partial y$ and heat, $\partial \overline{V'T'}/\partial y$, the zonal pressure gradient, $-\rho_o^{-1}\partial \overline{P}/\partial x$, and vertical velocity $\overline{W}$ at 152°W on the equator from Luan *et al.* (1993a). Data points are marked.

$$\overline{U}\frac{\partial \overline{U}}{\partial x} + \overline{W}\frac{\partial \overline{U}}{\partial z} + \frac{\partial \overline{V'U'}}{\partial y} = -\frac{1}{\rho_\circ}\frac{\partial \overline{F}_m}{\partial z} - \frac{1}{\rho_\circ}\frac{\partial \overline{P}}{\partial x} \tag{3.1}$$

$$\overline{U}\frac{\partial \overline{T}}{\partial x} + \overline{W}\frac{\partial \overline{T}}{\partial z} + \frac{\partial \overline{V'T'}}{\partial y} = -\frac{1}{\rho_\circ C_p}\frac{\partial \overline{F}_h}{\partial z} \tag{3.2}$$

where x, y and z are positive eastward, northward and upward ($z = 0$ at the sea surface), respectively; U, V and W are the velocity components corresponding to such coordinates; P is pressure, T is temperature; $\rho_\circ$ is density, and C_p is specific heat of seawater; $F_m(z)$ is the vertical turbulent flux of zonal momentum; $F_h(z)$ is the vertical turbulent heat flux including solar insolation. The long-term mean, denoted by overbars, is intended to be an average over a year or longer; the fluctuations, denoted by primes, are variations with time scales from a day to a year (Bryden and Brady, 1989). The climatological mean profiles of zonal velocity, temperature, and their zonal gradients, meridional eddy transports of zonal momentum and heat, the zonal pressure gradient, and the vertical velocity, are presented in Luan *et al.* (1993a) and shown in Fig. 11. The turbulent fluxes of momentum and heat are determined by the turbulence model described in the next section.

To model the temporal variation of upper-layer mixing in the equatorial Pacific Ocean, we rewrite Eqs. (3.1) and (3.2):

$$\frac{\partial \hat{U}}{\partial t} + \hat{U}\frac{\partial \overline{U}}{\partial x} + \overline{W}\frac{\partial \hat{U}}{\partial z} + \frac{\partial \overline{V'U'}}{\partial y} = -\frac{1}{\rho_\circ}\frac{\partial \hat{F}_m}{\partial z} - \frac{1}{\rho_\circ}\frac{\partial \overline{P}}{\partial x} \tag{3.3}$$

$$\frac{\partial \hat{T}}{\partial t} + \hat{U}\frac{\partial \overline{T}}{\partial x} + \overline{W}\frac{\partial \hat{T}}{\partial z} + \frac{\partial \overline{V'T'}}{\partial y} = -\frac{1}{\rho_\circ C_p}\frac{\partial \hat{F}_h}{\partial z} \tag{3.4}$$

$$\hat{\rho} = \rho_\circ[1 + \alpha(\hat{T} - T_\circ)] \tag{3.5}$$

where variables with hats are functions of t as well as z; those with overbars are time-independent, specified from the analysis of Luan *et al.* (1993a). Density ρ is approximated by a linear function of temperature with a constant thermal expansion coefficient α. Salinity is assumed to be constant and equal to a typical value of 35 ppt. The constant density, $\rho_\circ$, is that of sea water when the temperature takes the value of the long-term mean sea surface temperature, $T_\circ = 26.8°\mathrm{C}$ (Fig. 11), and the specified salinity of 35 ppt. Turbulent diffusivities are defined by

$$\hat{F}_m = -\rho_\circ \hat{K}_m \frac{\partial \hat{U}}{\partial z} \tag{3.6}$$

$$\hat{F}_h = -\rho_\circ C_p \hat{K}_h \frac{\partial \hat{T}}{\partial z} \tag{3.7}$$

where we assume solar insolation is completely absorbed at the sea surface. In Price *et al.* (1986) and Schudlich and Price (1992), the solar insolation was absorbed in the water column with a double exponential depth dependence.

The boundary and initial conditions are specified as follows. At the sea surface, constant fluxes of zonal momentum and heat (Luan *et al.*, 1993a) are imposed

$$\hat{F}_m(z=0,t) = -\tau_\circ^x = 0.048\ \mathrm{Nm}^{-2} \tag{3.8}$$

$$\hat{F}_h(z=0,t) = Q_{net} = -100\ \mathrm{Wm}^{-2} \tag{3.9}$$

At the bottom ($z = -h_b = -200\,\mathrm{m}$), $\hat{U}$, $\hat{T}$ will be fixed at their long-term averages

$$\hat{U}(z=-h_b,t) = \overline{U}(z=-h_b) \tag{3.10}$$

$$\hat{T}(z=-h_b,t) = \overline{T}(z=-h_b) \tag{3.11}$$

We use the long-term averages of observed zonal velocity and temperature (Fig. 11) to initialize the model

$$\hat{U}(z, t = 0) = \overline{U}(z) \tag{3.12}$$

$$\hat{T}(z, t = 0) = \overline{T}(z) \tag{3.13}$$

Sensitivity of the model results to different initial conditions are tested in Section 3.5 and found to be small.

3.3 Critical-R_i model

In the family of one-dimensional, time-dependent models of turbulence, the Price *et al.* (1986) model has a relatively simple parameterization of mixing processes. Its direct use of the critical Richardson number as a mixing criterion is preferred for simulating turbulence in the upper layers of the equatorial Pacific where values of the Richardson number were shown to be close to its critical value of 0.25 (Gregg *et al.*, 1985; Chereskin *et al.*, 1986; Luan *et al.*, 1993a).

At each time step in the Price *et al.* (1986) model, forcing and boundary conditions are imposed first, and then the resulting vertical profiles of density and currents are adjusted until the following three stability conditions are met:

$$\frac{\partial \hat{\rho}}{\partial z} \leq 0 \tag{3.14}$$

$$R_b = -\frac{g}{\rho_\circ} \frac{\Delta\rho\, h}{(\Delta\hat{U})^2 + (\Delta\hat{V})^2} \geq 0.65 \tag{3.15}$$

$$R_g(z) = -\frac{g}{\rho_\circ} \frac{\frac{\partial \hat{\rho}}{\partial z}}{(\frac{\partial \hat{U}}{\partial z})^2 + (\frac{\partial \hat{V}}{\partial z})^2} \geq R_{gc} = 0.25 \tag{3.16}$$

where z is upward. In the second condition, h is the depth of the mixed layer, and Δ is the difference in density or currents between the bottom grid of the mixed layer and that immediately below, and the mixed layer is defined as the thickness of surface layer of uniform density after the first condition is met but before the third is (see Schudlich and Price, 1992). Note the meridional component of velocity, $\hat{V}$, is not used in this paper. The first criterion is convective adjustment which simulates mixing due to density inversions from the application of forcing. The second is the bulk Richardson number mixing adjustment which parameterizes entrainment through the base of the mixed layer. The third is the local gradient Richardson number which models the shear instabilities. The first two criteria produce a slab-like surface mixed layer, while the last smoothes the discontinuity at the base of the mixed layer and yields a sheared transition layer (Price *et al.*, 1986). Mixing criteria used in Schudlich and Price (1992) are identical to those in Price *et al.* (1986).

In the model, adjustment of static instability and bulk Richardson number instability are achieved by homogenizing the properties of all layers between grid points in the surface mixed layer with the least number of the grid points below the surface mixed layer needed to meet the stability conditions. On the other hand, shear instabilities are removed by simultaneously rearranging the vertical shear and stratification within the adjacent grid points concerned, such that a new stable Richardson number, specified to be $R'_{gc} = 0.255$ [0.3 was specified by Price *et al.*(1986)], is obtained. The most unstable layer (with smallest $R_g < R_{gc} = 0.25$) is first adjusted, and new R_g are recalculated for both the layer above and the one below this most unstable layer. Then a new most unstable layer is located from the updated profile

of R_g, and removed, and R_g again updated. The process iterates until no instability exists between any adjacent levels. Model sensitivity to different values of R_{gc} and R'_{gc} are presented in Section 3.7.

We simplify the Price *et al.* (1986) model by excluding bulk Richardson number R_b mixing. It was used to model the mixed layer deepening (in slab models, Niiler and Kraus, 1977) driven either by surface stress (Kraus and Turner, 1967; Denman, 1973), or by shear across the base of the mixed layer slab (Pollard *et al.*, 1973). The studies of laboratory results (Ellison and Turner, 1959; Kato and Phillips, 1969) and simulations of observed cases (Denman and Miyake, 1973; Pollard *et al.*, 1973; Thompson, 1976 and 1977) showed no clear preference of one to the other. Price (1977) simulated the laboratory results of Kato and Phillips (1969) and Kantha *et al.* (1977), and Price *et al.* (1978) simulated observation of storm-induced mixed layer deepening, and concluded both results were realistically simulated with $R_b = 0.65$ evaluated by shear across the the mixed layer base, as was used in Price *et al.* (1986). The R_b mixing produces a surface mixed layer even with constant surface heating. However, the physics behind bulk Richardson mixing has been ambiguous (Pollard *et al.*, 1973; Phillips, 1977), compared to that behind the gradient Richardson number R_g (shear instability) mixing. The latter is supported both by laboratory experiment and by theoretical analysis (Turner, 1973; Thompson, 1980; Adamec *et al.*, 1981). From the perspective of the physics, it is hard to see why both bulk and gradient

mechanisms are needed. To represent continuous profiles, it would seem preferable to exclude bulk-R_i mixing. A test of the model with the bulk-R_i included are presented in Section 3.7.

We added to the model the option of including penetrative convection at the base of the surface mixed layer. While most of the difference in potential energy before and after convective adjustment is lost to turbulent dissipation, about 10 to 15% is used to entrain mass and momentum from below the surface mixed layer (Deardoff *et al.*, 1969; Deardoff, 1970; Davis *et al.*, 1981). We use a value of 15% in the model. The difference between using 10% and 15% is insignificant. The inclusion of penetrative convection has no effect when there is heating at the surface.

We added background diffusion of momentum and heat to the model. Based on field measurements (Peters *et al.*, 1988; Moum *et al.*, 1989; Luan *et al.*, 1993a), constant diffusivities of $K_{mb} = K_{hb} = K_b = 10^{-5}\,\mathrm{m^2\,s^{-1}}$ were chosen. At each time step, we apply background diffusion at each grid level at the same time when applying other forcing terms (right before checking for the three mixing criteria).

All mixing parameterizations in the model yield the same rates of mixing for momentum and heat, *i.e.*, $\overline{K}_m = \overline{K}_h$.

At the end of each time step, the total turbulent fluxes including the background diffusion (and the solar insolation for heat), $\hat{F}_m$ and $\hat{F}_h$, are evaluated by

$$\hat{F}_m^n(z) = \hat{F}_m^n|_{z=-200} - \rho_\circ \int_{-200}^{z} \left[\frac{\hat{U}^{n+1} - \hat{U}^n}{\Delta t} + \hat{U}^n \frac{\partial \overline{U}}{\partial x} + \overline{W} \frac{\partial \hat{U}^n}{\partial z} + \frac{\partial \overline{V'U'}}{\partial y} + \frac{1}{\rho_\circ} \frac{\partial \overline{P}}{\partial x} \right] dz \tag{3.17}$$

$$\hat{F}_h^n(z) = \hat{F}_h^n|_{z=-200} - \rho_\circ C_p \int_{-200}^{z} \left[\frac{\hat{T}^{n+1} - \hat{T}^n}{\Delta t} + \hat{U}^n \frac{\partial \overline{T}}{\partial x} + \overline{W} \frac{\partial \hat{T}^n}{\partial z} + \frac{\partial \overline{V'T'}}{\partial y} \right] dz \tag{3.18}$$

with

$$\hat{F}_m^n|_{z=-200} = -\rho_\circ K_b \frac{\partial \hat{U}^n}{\partial z}|_{z=-200} \tag{3.19}$$

$$\hat{F}_h^n|_{z=-200} = -\rho_\circ C_p K_b \frac{\partial \hat{T}^n}{\partial z}|_{z=-200} \tag{3.20}$$

where the superscript n represents evaluation at $t = n\Delta t$. Subsequently, turbulent diffusivities are evaluated as

$$\hat{K}_m^n(z) = -\frac{\hat{F}_m^n}{\rho_\circ \frac{\partial \hat{U}^n}{\partial z}} \tag{3.21}$$

$$\hat{K}_h^n(z) = -\frac{\hat{F}_h^n}{\rho_\circ C_p \frac{\partial \hat{T}^n}{\partial z}}. \tag{3.22}$$

A flow chart of the numerical algorithm and its numerical implementation are given in the Appendix. Analysis of numerical stability and convergence are also presented there. With $K_b = 10^{-5}\,\mathrm{m^2\,s^{-1}}$ and the maximum vertical velocity equal to $2.7 \times 10^{-5}\,\mathrm{m\,s^{-1}}$, the sufficient conditions for numerical stability and convergence are a vertical grid spacing of $\Delta z \leq 0.75\,\mathrm{m}$, and a time step $\Delta t \leq 7.5\,\mathrm{hr}$. Model tests show insensitivity to time step between 5 seconds and 1 hour; tests yield almost identical stable solutions with $\Delta z = 0.5\,\mathrm{m}$ and $\Delta z = 1\,\mathrm{m}$, very small artificial fluctuations with $\Delta z = 2\,\mathrm{m}$, and increasingly larger artificial fluctuations associated with numerical instability with

larger Δz ($> 2\,\mathrm{m}$) (see Appendix). However, when averaged over a period of 100 days, the simulated zonal velocity, temperature, and turbulent fluxes and diffusivities, show small differences for values of $\Delta z \leq 5\,\mathrm{m}$. Therefore, we used $\Delta t = 15\,\mathrm{min}$ and $\Delta z = 1\,\mathrm{m}$ in our discussion of model results.

3.4 Modeled steady state

Shown in Fig. 12 are time series of daily-averaged zonal velocity and temperature from a 600-day simulation with $\Delta t = 15\,\mathrm{min}$, $\Delta z = 1\,\mathrm{m}$, and constant surface heating and surface absorption of solar insolation. Transients gradually decay after the first 100 days, and eventually reach a steady state after 300 days.

There are two time scales related to the model spin-up: one due to vertical advection, and the other due to background diffusion. With the mean vertical velocity used in the model equal to $1.8 \times 10^{-5}\,\mathrm{m\,s^{-1}}$, it takes about 110 days for a water parcel to travel from the depth of 200 m to the surface. So the vertical advection time scale is about 100 days. The diffusion time scale is estimated to be about 100 years for $K_b = 10^{-5}\,\mathrm{m^2\,s^{-1}}$ as used in the model (and about 500 days for $K_b = 10^{-3}\,\mathrm{m^2\,s^{-1}}$). The diffusion time scale is very long compared to the advection time scale. Nevertheless, the dominating (shorter) advection time scale of 100 days shows that a model of turbulence should be sufficiently spun up before diurnal cycles can be studied. Otherwise, transients may be aliased into the diurnal signals.

Mean vertical profiles of modeled zonal velocity and temperature were averaged between day 500 and 600 (dashed lines in Fig. 13). The departure of the simulated mean steady-state zonal velocity from its observed long-

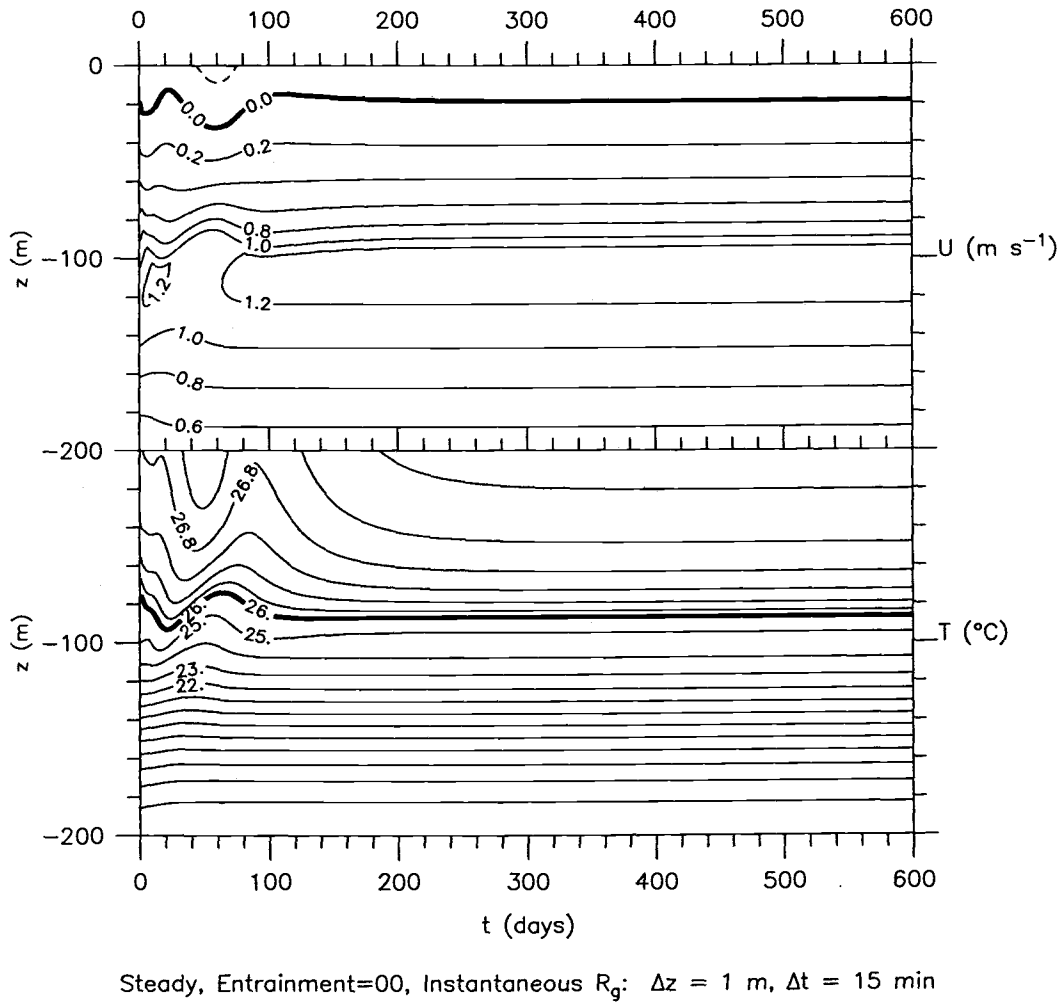

Figure 12. Model contours for the standard case of $\hat{U}$ (upper panel) and $\hat{T}$ (lower panel) *vs.* time. The contour interval of zonal velocity is $0.02\,\mathrm{m\,s^{-1}}$ with the dark line being zero. Contour intervals of temperature are 1°C below 26°C and 0.2°C above it, with the 26°C isotherm being dark.

term mean at the sea surface is $0.12\,\mathrm{m\,s^{-1}}$. Besides these differences, the simulated profile of zonal velocity preserves most features of the observed long-term mean, except in the region just above the undercurrent core, which is discussed below. The simulated temperature profile agrees with that of the observed long-term mean within 0.5°C (Fig. 13). Therefore, the steady state of simulated velocity and temperature stays close to their observed long-term means.

As required by the model, the simulated mean gradient Richardson number $\hat{R}_g$ stays at its critical value of 0.25 within the mixing zone above 100 m. $\hat{R}_g$ becomes infinitely large at the undercurrent core and stays above 0.25 in the 100 to 200 m range (Fig. 14). In the model, shear instabilities generate mixing only above the depth of zonal velocity maximum.

Just above the depth of simulated zonal velocity maximum, the simulated vertical gradients of both zonal velocity and temperature increase rapidly to peaks, due to the jump of the gradient Richardson number from its critical value to infinity. There exists a mixing barrier in the model at the depth of the zonal velocity maximum. In the real ocean, time varying forcing and internal waves would tend to smooth the transition to background diffusion below the more actively mixed surface layer.

The modeled mean vertical fluxes of turbulent momentum and heat and turbulent diffusivities are consistent with their counterpart from the inverse solution in the actively mixed surface layer above the zonal velocity maximum (Fig. 13). Near and below the depth of the zonal velocity maximum, the turbulent fluxes reduce to the prescribed background diffusion.

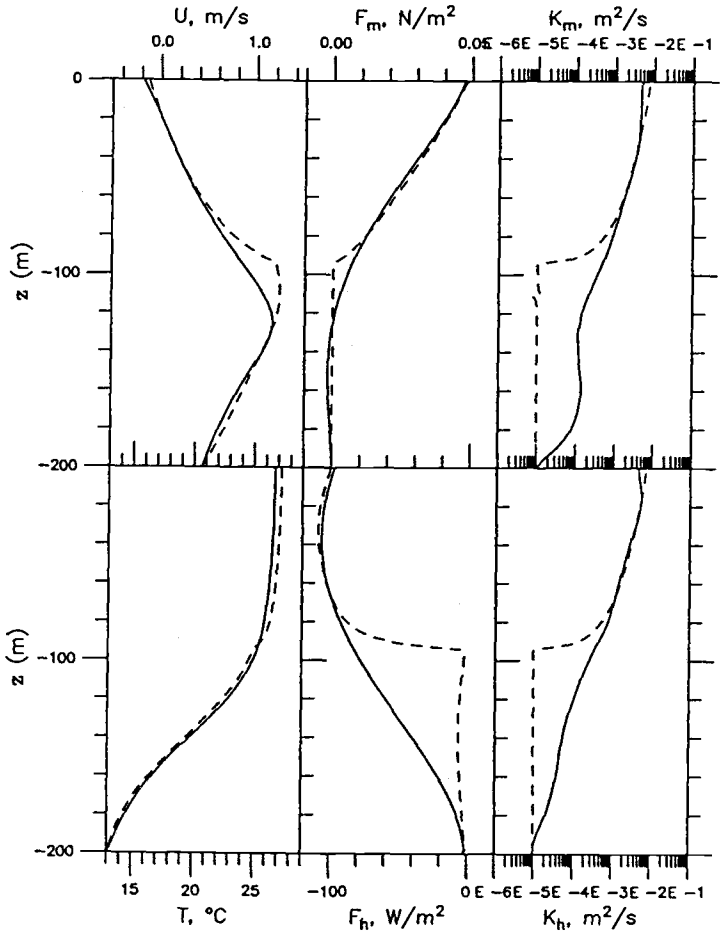

Figure 13. Profiles of zonal velocity, temperature, turbulent fluxes of zonal momentum and heat, and turbulent diffusivities, averaged between day 500 and 600 from the model (dashes), compared with the results of the inverse analysis by Luan *et al.* (1993a) (solid).

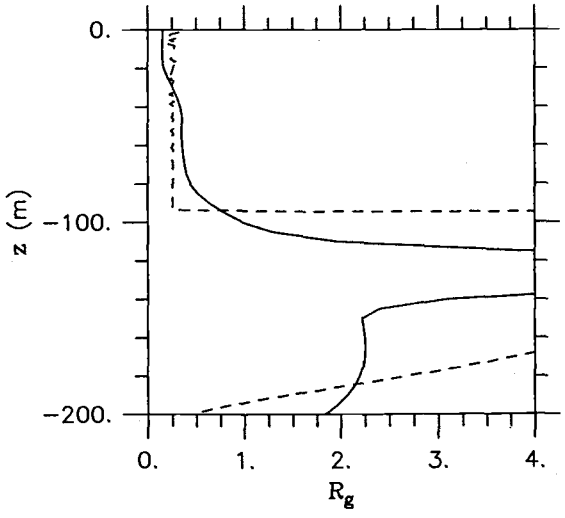

Figure 14. The profile of gradient Richardson number averaged between day 500 and 600 from the model (dashes), compared with the results of the inverse analysis by Luan *et al.* (1993a) (solid).

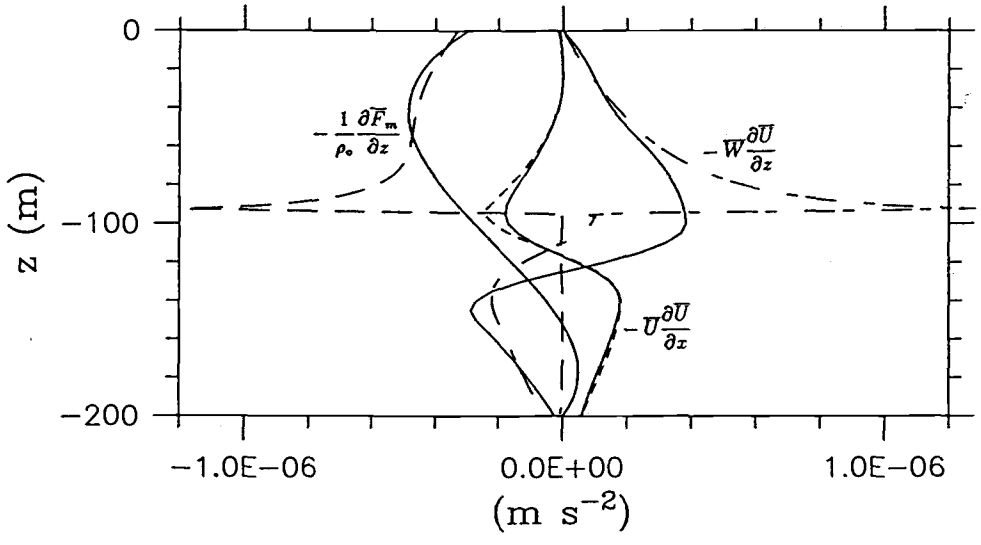

Figure 15. Components of the zonal momentum balance. The convergence of vertical turbulent zonal momentum flux, and vertical and zonal advections of the zonal momentum, all averaged over the last 100 days of the 600-day model simulation (dashed) are compared with those at 152°W on the equator from the inverse analysis (solid, from Luan *et al.*, 1993a).

Three modeled terms of the zonal momentum and heat balance equations, *i.e.*, the zonal and vertical advection, and the vertical convergences of turbulent fluxes, are calculated and compared (Fig. 15 and 16). The advection terms are close to their long-term means because the difference between $\hat{U}$ and $\overline{U}$ is small and $\partial\overline{U}/\partial x$ and $\partial\overline{T}/\partial x$ are specified to remain unchanged. The vertical velocity in the model is also specified to be identical to the inverse solution; therefore, the modeled vertical advection terms are close to the inverse solutions, except between the depths of 80 and 130 m around the zonal velocity maximum, where there are spikes due to those in vertical gradients of zonal velocity and temperature. The simulated convergences of turbulent fluxes of zonal momentum and heat agree with the inverse solutions in the upper 80 m. But they also have spikes balancing those of the vertical advections just above the depth of zonal velocity maximum, and decrease to near-zero background diffusion below, in comparison with the smooth and slightly larger inverse solutions.

3.5 Sensitivity to initial conditions

The model was run with different combinations of the initial profiles of zonal velocity and temperature, with all other factors being unchanged. Even though the simulations go through various times of adjustment, they all reached approximate steady states close to that in Fig. 12. In other words, the model is convergent.

The time series of one such model run is shown in Fig. 17. In this case, the initial conditions of zonal velocity and temperature were uniform in depth, $\hat{U}(z, t = 0) = -0.5\,\mathrm{m\,s^{-1}}$ and $\hat{T}(z, t = 0) = 14\,^{\circ}\mathrm{C}$, with a time step of 15 min

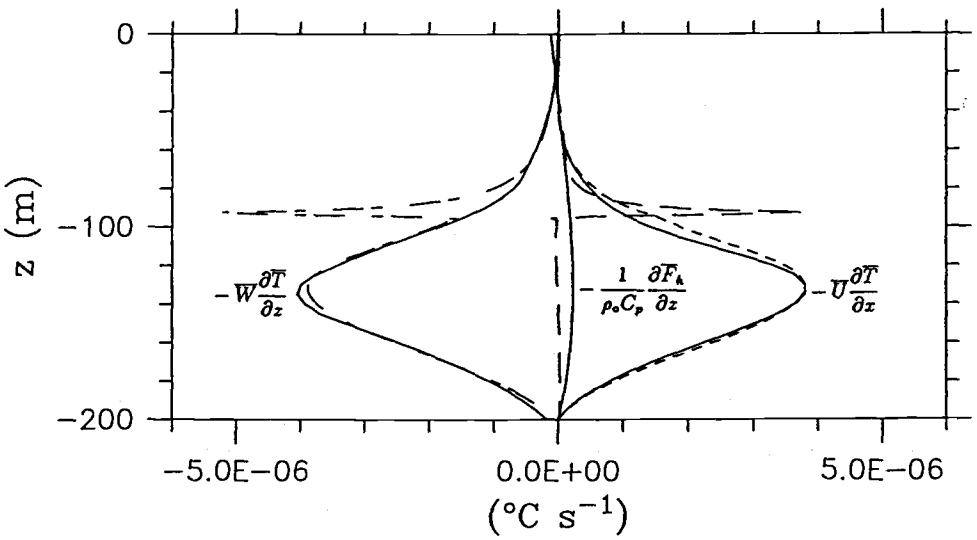

Figure 16. Components of the heat balance. The convergence of vertical turbulent heat flux, and zonal and vertical advection of heat, all averaged over the last 100 days of the 600-day model simulation (dashed) are compared with those at 152°W on the equator from the inverse analysis (solid, from Luan *et al.*, 1993a).

and a vertical grid spacing of 1 m. The vertical advection was responsible for the swift adjustment in the first 400 days or so (Fig. 12). The remaining detailed differences, such as still weaker stratification and slower undercurrent in this case, were slowly smoothed out by the background diffusion. Comparison of model runs with a variety initial conditions show that the period of model transition to steady state is proportional to the difference between the initial state and the steady state. This again demonstrates the importance of model spin-up for studying diurnal cycles in the upper layer of the equatorial oceans.

The convergence to the steady state in this model is plausible. Even when the initial conditions are changed dramatically, the boundary conditions and forcings remain the same. The easterly wind at the surface interacts through mixings with the eastward pressure gradient. While the surface heating raises the temperature of the upper layer through turbulent transfer, upwelling carries cold water up. These balancing forces bring about a sub-surface maximum of the eastward flow together with a thermocline. The vertical gradients of velocity and temperature are adjusted through mixing due to occurrence of shear instabilities. Meanwhile, the model was forced at the bottom with the mean values of long-term velocity and temperature observed at 152°W on the equator. These bottom constraints provide the model with reference values for velocity and temperature. Eventually, the model will reach the steady state through dynamic adjustments dictated by these boundary conditions and forcings regardless of the initial states.

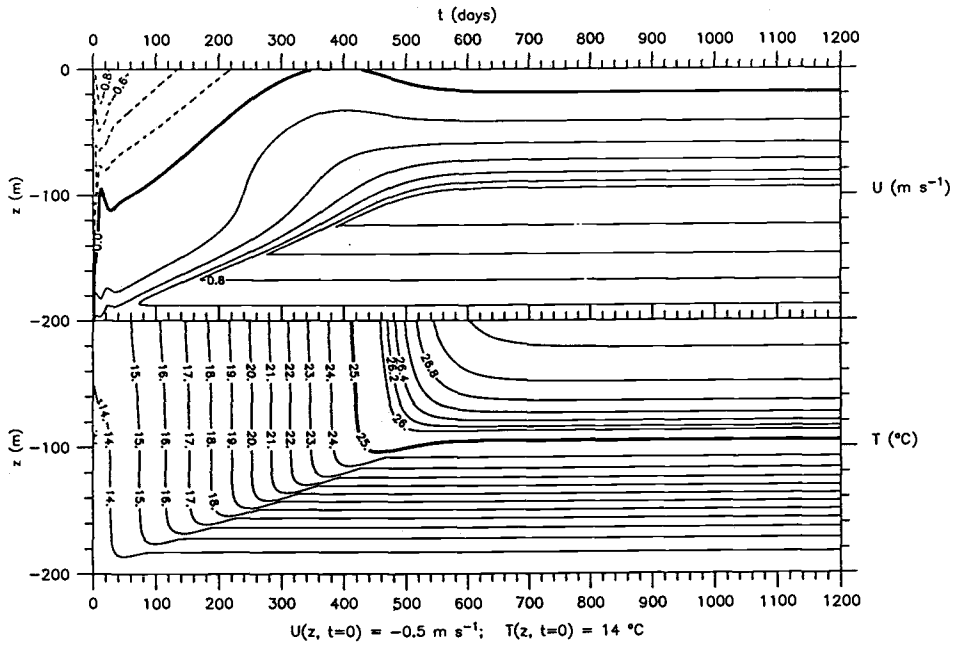

Figure 17. Convergence of the model steady state tested by changing initial conditions on zonal velocity and temperature. In this case, the initial conditions of zonal velocity and temperature were $\hat{U}(z, t = 0) = -0.5\,\mathrm{m\,s^{-1}}$ and $\hat{T}(z, t = 0) = 14\,^{\circ}\mathrm{C}$, with a time step of 15 min and a vertical grid spacing of 1 m. After about 600 days, the model returns back to the same steady state as in Fig. 12.

3.6 Sensitivity to forcing

Sensitivity of model results to forcing terms are tested. We define the standard case as the model run of 600 days with $\Delta t = 15\,\mathrm{min}$ and $\Delta z = 1\,\mathrm{m}$. At the end of model day 600 of the standard case, forcing terms are multiplied by a factor of 0.5 or 1.5, and the model is run for another 300 model days, *i.e.*, from day 600 to day 900, with all other parameters unchanged. Results are averaged over the last 100 days of the perturbed 300-day simulation and compared with those averaged over the last 100 days before the perturbation (Fig. 18). The model simulations for each perturbation may not necessarily reach steady states within the 300 model days.

To quantify the sensitivity of the model to forcing, we use five pairs of indicators (Table. 2). The first pair are the depth of zonal velocity maxima, D_U, and the depth of surface mixed layers, D_T. They measure the changes in the shapes of vertical profiles of zonal velocity and temperature. For the standard case, the depth of zonal velocity maximum is 110 m, and the depth of surface mixed layer is 25 m. The second pair are the rms differences over the 200-m column between the last 100-day averages of the zonal velocity and temperature of the perturbed cases and those of the pre-perturbation, U^{rms} and T^{rms}, respectively. They measure the amount of departure from the standard steady state due to perturbation of forcing terms. The smaller these rms values, the closer the perturbed cases to the standard case. The third pair are the rms values over the 200-m column of daily averaged time rates of changes of velocity and temperature of the perturbed cases over the same 100-day period, $(\frac{\partial U}{\partial t})^{rms}$ and $(\frac{\partial T}{\partial t})^{rms}$, respectively. These values measure how

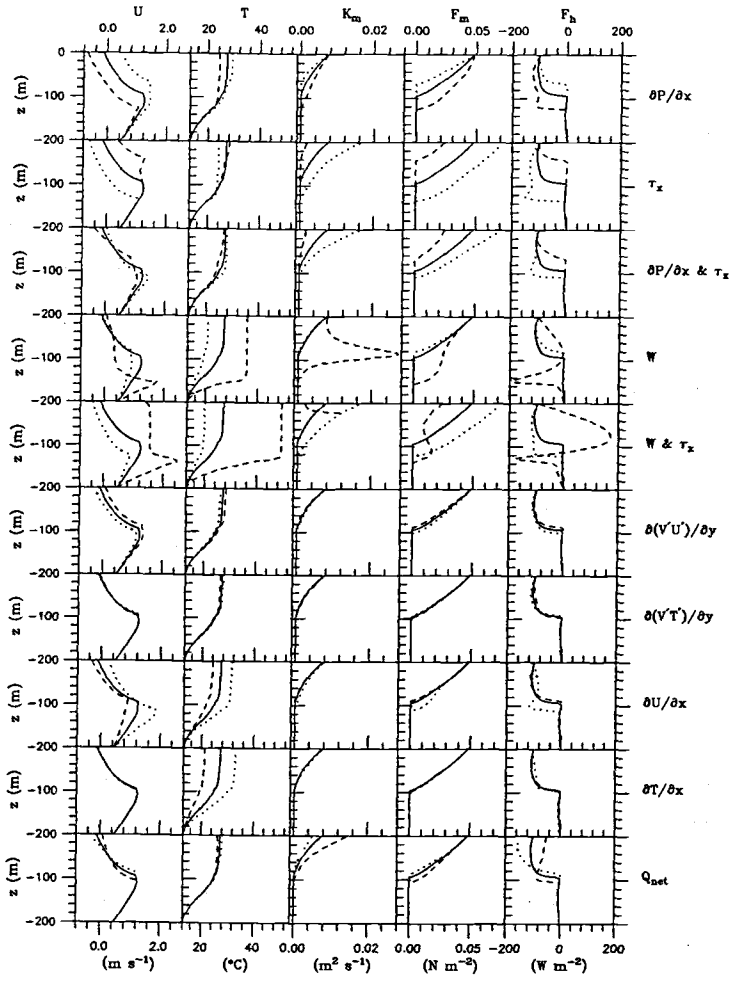

Figure 18. Responses of the model to 50% increase (dotted) and 50% decrease (dashed) of the terms indicated to the right. The model was perturbed at the end of the standard 600-day simulation and continued for 300 more days (from day 600 through day 900), results between day 800 and day 900 were then averaged and, compared to the results averaged over the last 100 days of the 600-day simulation (solid) of the standard case (Fig. 12).

fast the model adjusts to reach new balances of zonal momentum and heat over the 200-m column. Smaller rms time rates of changes indicate model is closer to new steady-state balances. The forth pair are the differences between the last 100-day averages of the zonal velocity and temperature at the surface of the perturbed cases and of the pre-perturbation, U_s^{rms} and T_s^{rms}, respectively. They measure the amount of departure of the surface mixed layers of the perturbed cases from that of the standard case. The smaller these differences, the closer the perturbed cases to the standard case. The fifth pair are the rms values of daily averaged time rates of changes of velocity and temperature at the surface of the perturbed cases over the last 100-day period. $(\frac{\partial U_s}{\partial t})^{rms}$ and $(\frac{\partial T_s}{\partial t})^{rms}$, respectively. These values measure how fast the model adjusts to new balances at the surface. Smaller rms time rates of changes at the surface indicate model is closer to new steady-state balances at the surface.

Decrease of the pressure gradient leaves a residual in westward wind stress. Thus, the surface layer is accelerated in the westward direction and more strongly sheared. The increase in shear causes more mixing to yield a colder surface layer and larger westward surface jet, and a deeper thermocline and undercurrent core. The excess in wind stress eventually decreased the undercurrent speed through vertical mixing. The increase of the pressure gradient essentially yields effects opposite to those of its similar increase.

The decrease (increase) of wind stress yields approximately the same effects as the increase (decrease) of zonal pressure gradient, except that the depth of the zonal velocity maximum responds more strongly to wind stress changes. One may expect stronger trades to bring about a stronger east-

Case	D_U (m)	U^{rms} (10^{-2} m/s)	$(\frac{\partial U}{\partial t})^{rms}$ (10^{-3} m/s^2)	U_s^{rms} (10^{-2} m/s)	$(\frac{\partial U_s}{\partial t})^{rms}$ (10^{-3} m/s^2)	D_T (m)	T^{rms} (10^{-1} °C)	$(\frac{\partial T}{\partial t})^{rms}$ (10^{-3} °C/s)	T_s^{rms} (10^{-1} °C)	$(\frac{\partial T_s}{\partial t})^{rms}$ (10^{-3} °C/s)
Standard	-110	0	1	0	2	-25	0	0	0	0
$\frac{\partial \bar{P}}{\partial x}$ decreases 50%	-126	52	29	54	649	-26	19	30	28	54
$\frac{\partial \bar{P}}{\partial x}$ increases 50%	-68	46	2	61	3	-24	12	2	20	6
τ_x decreases 50%	-42	48	1	52	3	-9	5	0	12	3
τ_x increases 50%	-135	57	43	46	17	-42	19	46	30	73
$\frac{\partial \bar{P}}{\partial x}$ & τ_x decreases 50%	-116	15	2	26	5	-9	10	2	6	6
$\frac{\partial \bar{P}}{\partial x}$ & τ_x increases 50%	-110	12	8	15	7	-43	8	7	6	14
$\bar{W}$ decreases 50%	-156	49	108	17	81	-69	100	309	87	408
$\bar{W}$ increases 50%	-107	17	1	4	1	-25	49	1	63	3
$\bar{W}$ & τ_x decreases 50%	-138	100	255	153	253	-109	199	713	222	1061
$\bar{W}$ & τ_x increases 50%	-124	45	23	26	5	-45	53	13	73	21
$\frac{\partial \bar{U}}{\partial x}$ decreases 50%	-89	24	10	19	7	-25	26	6	33	17
$\frac{\partial \bar{U}}{\partial x}$ increases 50%	-115	34	70	35	90	-28	35	55	40	109
$\frac{\partial \bar{T}}{\partial x}$ decreases 50%	-110	2	7	1	12	-25	47	4	61	11
$\frac{\partial \bar{T}}{\partial x}$ increases 50%	-110	3	50	3	81	-27	46	39	57	90
$\frac{\partial \overline{V'U'}}{\partial y}$ decreases 50%	-109	16	4	19	6	-25	7	3	11	8
$\frac{\partial \overline{V'U'}}{\partial y}$ increases 50%	-112	17	6	18	8	-26	8	4	11	10
$\frac{\partial \overline{V'T'}}{\partial y}$ decreases 50%	-110	3	2	3	3	-27	4	2	6	5
$\frac{\partial \overline{V'U'}}{\partial y}$ increases 50%	-110	2	1	3	2	-24	4	2	6	4
Q_{net} decreases 50%	-110	12	2	20	3	-54	5	3	9	6
Q_{net} increases 50%	-110	9	1	18	2	-14	4	1	9	2

Table 2. Indicators of sensitivity of model to forcing. D_U and D_T–depths of zonal velocity maxima and surface mixed layers, respectively; U^{rms} and T^{rms}–rms differences over the 200-m column between the last 100-day averages of the zonal velocity and temperature of the perturbed cases and those of the pre-perturbation, respectively; $(\frac{\partial U}{\partial t})^{rms}$ and $(\frac{\partial T}{\partial t})^{rms}$–rms values over the 200-m column of daily averaged time rates of changes of velocity and temperature of the perturbed cases over the last 100 days, respectively; U_s^{rms} and T_s^{rms}–differences between the last 100-day averages of the zonal velocity and temperature at the surface of the perturbed cases and of the pre-perturbation, respectively; $(\frac{\partial U_s}{\partial t})^{rms}$ and $(\frac{\partial T_s}{\partial t})^{rms}$–rms values of daily averaged time rates of changes of velocity and temperature at the surface of the perturbed cases over the last 100-day period, respectively.

ward zonal pressure gradient, and *vice versa*, with some time lags. When we run the model with simultaneous perturbations of pressure gradient and wind stress, we see mild changes and the model almost reaches steady states within the 300 days of simulations.

The effects of changing the wind stress and pressure gradient are different on turbulent mixing. Comparing the above perturbation cases, we find that turbulent diffusivities increase as wind intensifies, but such changes of turbulent diffusivities due to changes in pressure gradient alone are not as large. This is because the pressure gradient affects the flow as a body force, but the surface wind can only have its effects felt at lower depths through turbulent mixing.

Decrease in the vertical velocity reduces upward transport of colder water into the surface layer above the undercurrent core. This creates a large imbalance in heat balance near the 140-m depth, where zonal advection carries warmer water from the west. Density inversion and hence convection occur, raising surface temperature. And the surface layer and the undercurrent core extend to 140 m depth. Steady state is not reached at the end of 300-day simulation. Increase in the vertical velocity produces the opposite effects.

We also test the cases when vertical velocity and the surface wind stress are both increased or reduced simultaneously in the model. Such changes are plausible, because intensifying (weakening) easterly winds at the surface of the equatorial ocean are accompanied by increasing (decreasing) upwelling due to Ekman transport. The results of such simultaneous perturbations show that their effects add: the responses of model are much larger than

those when changing only one of them a time. Therefore, the surface wind and upwelling cannot balance each other, unlike the balancing of the wind stress and the zonal pressure gradient.

The perturbations of either the meridional eddy transport of zonal momentum or that of heat have very limited effects on the steady state, because they are relatively small in the balances. The model is close to steady state by the end of the 300-day simulations of these perturbed forcings.

Decrease in the zonal gradient of zonal velocity yields acceleration of the zonal velocity above the undercurrent. Shear and hence mixing are intensified in the surface layer, yielding a deeper thermocline and undercurrent core. The increase in zonal velocity below the 100-m depth due to the deeper undercurrent causes increase in heating due to zonal advection, hence increase in surface temperature through mixing. The model is moderately unsteady during the last 100 days of the perturbation simulation. Increase of zonal gradient of zonal velocity yields opposite effects.

The perturbations of the zonal gradient of temperature hardly affect the momentum balance, but greatly affect the heat. In the model, the vertical gradient of temperature is adjusted through mixing in order for the vertical advection of heat to balance the change in the zonal advection when the zonal temperature gradient is changed. This differentiates the perturbation of the zonal gradient of temperature from the perturbation of all the other terms, which affect both the momentum and heat balances demonstrating coupling between the balances.

Varying the net surface heat flux from 50 to 150 $W\,s^{-1}$, both net heating, causes moderate changes in the simulated zonal velocity and minor changes in temperature. The simulations are almost steady.

3.7 Sensitivity to mixing parameterizations

In this section, all the model simulations are carried out for 600 days with the same forcing and same $\Delta t = 15$ min and $\Delta z = 1$ m, as for the case used in Section 3.4 and shown in Fig. 12, except for the to-be-specified changes in the mixing parameterizations.

Turbulent mixing induced by shear instabilities does not stop immediately when adjusted gradient Richardson number R'_g reaches the critical value R_{gc}, but continues until R'_g is larger than the critical value, R'_{gc} ($> R_{gc} = 0.25$). Price *et al.*(1986) reported that their choice of $R'_{gc} = 0.30$ versus, say, 0.25, was strictly for numerical convenience and had no appreciable consequence in the solutions. We used $R'_{gc} = 0.255$ in our simulations. However, there are arguments in favor larger values for R'_{gc}, for example, one, by Stull (1991). We tested values of $R'_{gc} = 0.30$ and 0.50 and plotted the profiles of some averaged properties in Fig. 19. Results for $R'_{gc} = 0.30$ are insignificantly different from those for $R'_{gc} = 0.255$; results for $R'_{gc} = 0.50$ show slightly more mixing than those for $R'_{gc} = 0.255$. Computation time to run the model decreases as values of R'_{gc} increase.

The critical value for the Richardson number R_{gc} has been determined both by theory and experiments and generally taken as 0.25 (Turner, 1973; Thompson, 1980; Adamec *et al.*, 1981; Peters *et al.*, 1988; Chereskin *et al.*,

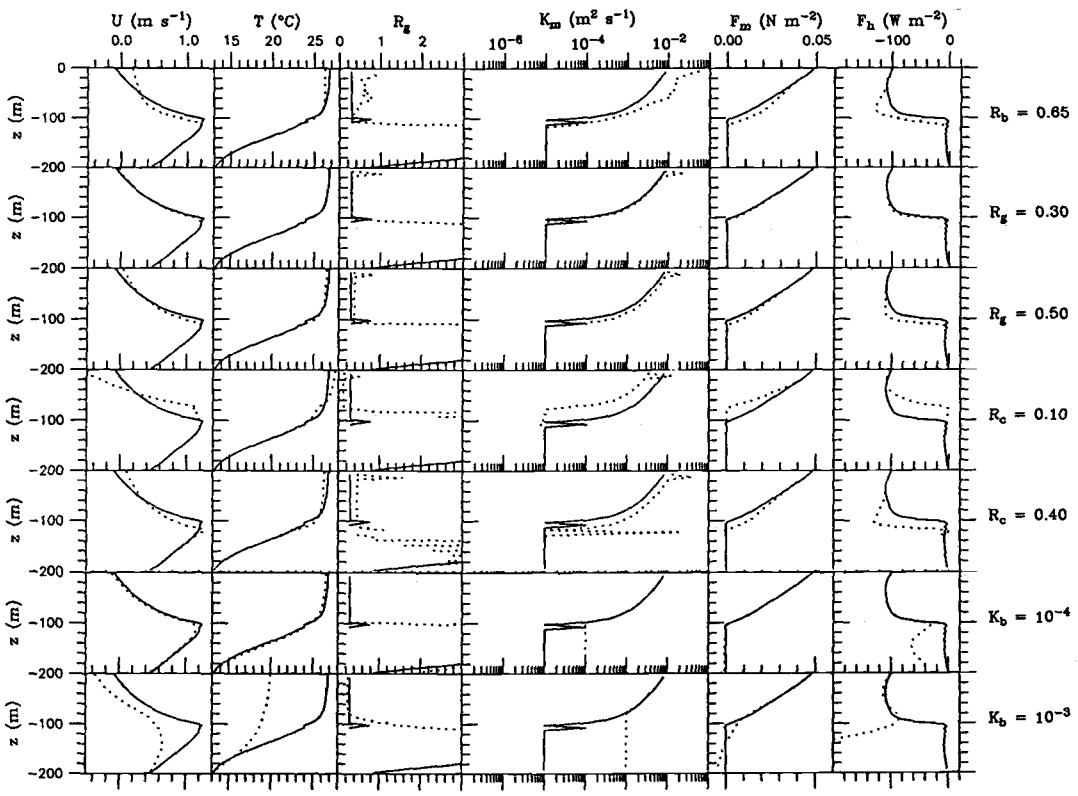

Figure 19. Sensitivity of the modeled velocity U, temperature T, the gradient Richardson number R_g, turbulent diffusivity K_m and turbulent fluxes of momentum F_m and heat F_h to changes in mixing parameters plotted in dotted lines. Changing the post-mixing gradient Richardson number to (a) $R'_{gc} = 0.30$, and (b) $R'_{gc} = 0.50$, both with the critical Richardson number $R_{gc} = 0.25$; changing the critical value of gradient Richardson number to (c) $R_{gc} = 0.10$ with $R'_{gc} = 0.105$, and (d) $R_{gc} = 0.40$ with the $R'_{gc} = 0.405$; increasing the background diffusivity to (e) $K_b = 10^{-4}$, and (f) $K_b = 10^{-3}\,\mathrm{m^2\,s^{-1}}$; (g) including the bulk Richardson number mixing ($R_b = 0.65$). All results are compared with those of the standard case (solid lines) (with $R_{gc} = 0.25$, $R'_{gc} = 0.255$, $K_b = 10^{-5}\,\mathrm{m^2\,s^{-1}}$, and R_b mixing excluded. Heat flux for $K_b = 10^{-3}\,\mathrm{m^2\,s^{-1}}$ was off scale below the 130-m depth.

1986). Nevertheless, we tested the model with $R_c = 0.10$ and 0.40 (Fig. 19). As the critical value of the Richardson number R_c increases, the surface mixing layer deepens, and the shear in the surface layers decreases. In particular, the results for $R_{gc} = 0.1$ suggests that the background forcing and the observations are incompatible with this value of R_{gc}. The manipulations of critical Richardson numbers cannot avoid the insufficient turbulent mixing near the undercurrent core, where the gradient Richardson number is very large (discussed in Section 3.4).

The sufficient conditions for numerical stability and convergence of the explicit numerical difference scheme depends on the prescribed vertical velocity $\overline{W}(z)$ and the prescribed constant background diffusivity K_b:

$$K_b - \frac{\overline{W}}{2}\Delta z \geq 0 \tag{3.23}$$

$$1 - \left[\frac{2K_b}{(\Delta z)^2} + \frac{\partial \overline{U}}{\partial x}\right]\Delta t \geq 0 \tag{3.24}$$

Detailed description and analysis are given in the Appendix. For $K_b = 10^{-5}\,\mathrm{m^2\,s^{-1}}$, $\max[\overline{W}(z)] = 2.7 \times 10^{-5}\,\mathrm{m\,s^{-1}}$, and $\max(\partial\overline{U}/\partial x) = 2 \times 10^{-7}\,\mathrm{s^{-1}}$, as used in the model, we obtain $\Delta z \leq 0.75\,\mathrm{m}$ from (3.23), and $\Delta t \leq 7.5\,\mathrm{hr}$ from (3.24).

We test $K_b = 10^{-4}$ and $10^{-3}\,\mathrm{m^2\,s^{-1}}$ and compare the results with those for $K_b = 10^{-5}$, with $\Delta z = 1\,\mathrm{m}$ and $\Delta t = 15\,\mathrm{min}$ (Figs. 19 and 20). The simulated steady-state zonal velocity and temperature are close to each other for K_b between 10^{-5} and $10^{-4}\,\mathrm{m^2\,s^{-1}}$, but not so for larger values of K_b, such as $10^{-3}\,\mathrm{m^2\,s^{-1}}$, which is excessively diffusive below the depth of zonal velocity maximum. The diffusion time scales are 10 years and 1 year for $K_b = 10^{-4}$ and $10^{-3}\,\mathrm{m^2\,s^{-1}}$, respectively (Fig. 20). Therefore, increasing

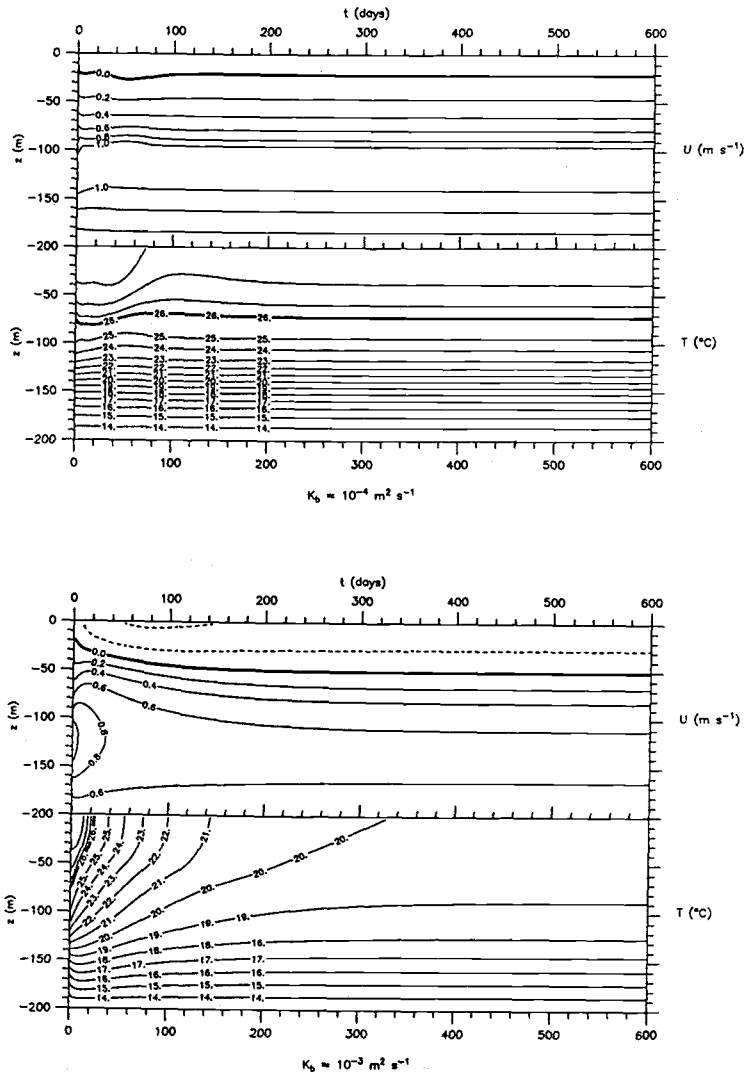

Figure 20. Time series of daily averaged zonal velocity and temperature modeled with the prescribed background diffusivity (a) $K_b = 10^{-4}\,\mathrm{m^2 s^{-1}}$ and (b) $K_b = 10^{-3}\,\mathrm{m^2 s^{-1}}$, instead of $K_b = 10^{-5}\,\mathrm{m^2 s^{-1}}$ used in the standard case (Fig. 12).

the value of the constant background diffusivity smooths the structure near the undercurrent core, and increases turbulent fluxes below. As discussed in Luan *et al.* (1993a), $K_b = 10^{-5}\,\mathrm{m^2\,s^{-1}}$ is a more appropriate value below the undercurrent core based on observational results.

We have excluded the bulk mixing of the original Price model in all our simulations. The results discussed in the previous sections show that the combination of convection and shear instability have reasonably parameterized the turbulent transfers in the equatorial ocean above the undercurrent core. Removal of the bulk Richardson number mixing further reduces the number of adjustable parameters in the model.

A time series of modeled zonal velocity and temperature, with bulk Richardson number mixing included, is shown in Fig. 21. The inclusion of R_b mixing causes periodic (about 7 days in this example) fluctuation of $\hat{U}$ and $\hat{T}$ in the surface layer, even though all forcing terms are time-independent. In the model, vertical shear gradually build up below the surface mixed layer until R_b becomes unstable. When unstable R_b occurs, the model makes an often large adjustment instantaneously in the time step, causing the mixed layer to deepen (not shown). Then shear starts to build up again and so on. The time interval between the two major consecutive adjustments of unstable R_b is the period of fluctuations shown in Fig. 21. which is in part related to model forcing. During the phase of shear buildup, the base of the surface mixed layer is raised up by erosion due to R_g (shear instabilities) mixing at and below the base.

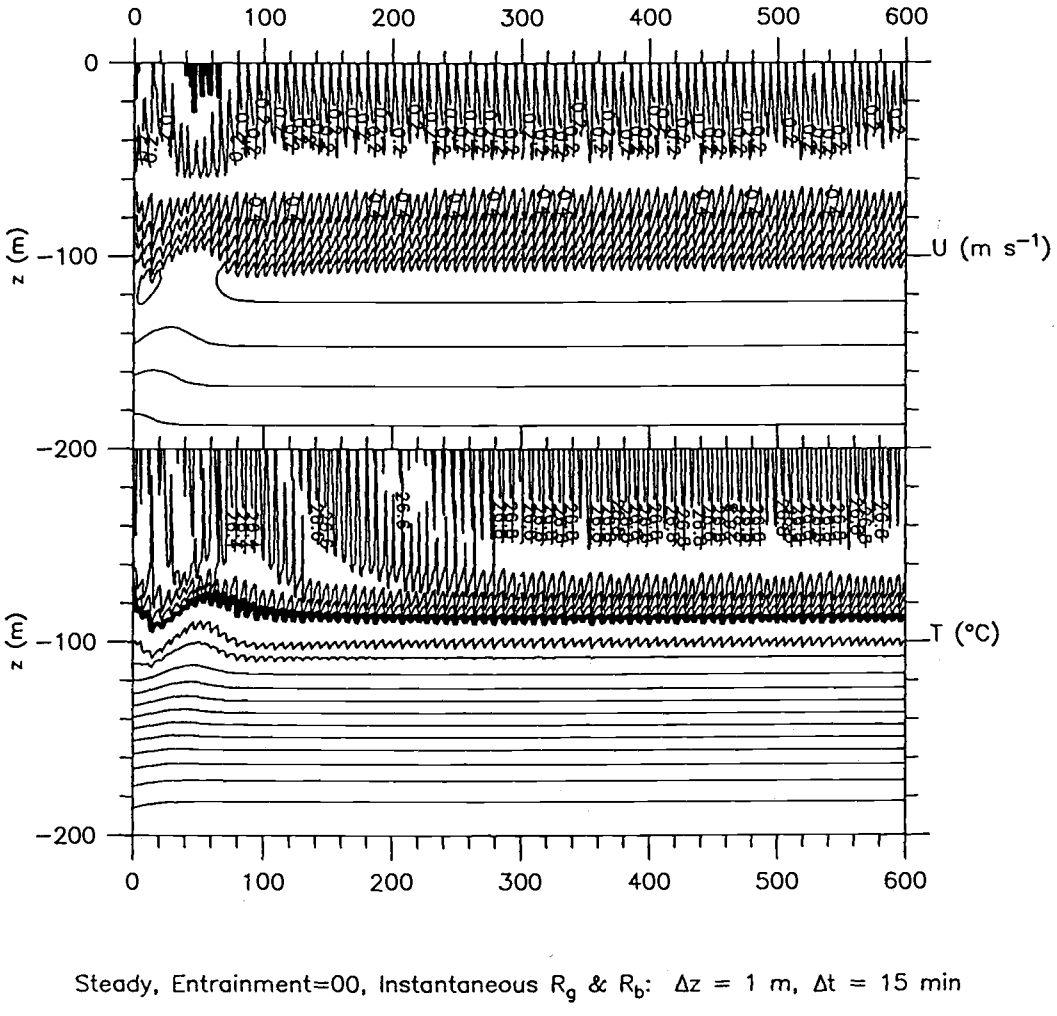

Figure 21. Same as Fig. 12 but with bulk Richardson number R_b mixing included.

The inclusion of R_b criterion also creates much more mixing in the surface mixed layer. The model diffusivities are much larger, the surface mixing layer is deeper, and the vertical shear in the upper layer is much smaller, than when bulk mixing is turned off in the model (Fig. 19). This provides additional support for the exclusion of the bulk Richardson number mixing.

3.8 Conclusions

We modified the turbulent mixing model of Price *et al.* (1986) to obtain a critical-R_i model that includes parameterizations of convective adjustment, shear instability mixing, and a prescribed background diffusion of constant diffusivity, but excludes the bulk Richardson number mixing. The model was then applied to simulate the turbulent mixing of zonal momentum and heat in the upper 200 m of the equatorial Pacific at 152°W. The model was run with constant forcing and boundary conditions based on the inverse analysis of the long-term steady-state balances of zonal momentum and heat by Luan *et al.* (1993a).

The modeled steady-state velocity, temperature, turbulent fluxes and diffusivities are consistent with those of the inverse analysis. Tests of different initial conditions suggest the model converges to the long-term steady state. The model reponds to changes in forcing reasonably.

There are two spin-up processes in the model. The dominating one is due to vertical advection with a time scale of about 100 days, which is responsible for a swift model adjustment toward the steady state. And the secondary one is due to diffusion with a time scale of about 10 years, which is responsible

for a slow model adjustment to the steady state. The transient behavior demonstrated by the modeled time series underscores the importance that a model of turbulence be fully spun up before investigating effects of time-varying surface forcing.

The model showed a build-up of vertical gradients of zonal velocity and temperature just above the undercurrent core where the gradient Richardson number is far above its critical value. (We expect application of seasonally varying, rather than the time-independent, forcing to the model, to smooth the spikes to some extent.) Increasing the prescribed background diffusivity of $1 \times 10^{-5} \mathrm{m}^2\,\mathrm{s}^{-1}$ to $1 \times 10^{-4} \mathrm{m}^2\,\mathrm{s}^{-1}$ smoothes the high vertical gradients near the core somewhat. The value $1 \times 10^{-5} \mathrm{m}^2\,\mathrm{s}^{-1}$ is supported by experiments for depths below the undercurrent core.

Sensitivity tests showed that varying critical values of the gradient Richardson numbers has a significant effect on the model results. In particular, the results for $R_c = 0.1$ suggests that the background forcing and the observations are incompatible with this value of R_c. Varying the post-mixing Richardson number from 0.255 to 0.30 shows no significant differences in the model results; but model results for the larger value of 0.50 show slightly more mixing in the surface layer. Nevertheless, all these variations in Richardson number still show the build-up of vertical gradients of velocity and temperature above the undercurrent core.

We have tested the inclusion of the bulk Richardson mixing criterion used by Price *et al.* (1986) and Schudlich and Price (1992). The inclusion of the R_b criterion caused frequent near-surface fluctuations in the time series of modeled velocity and temperature, even when all forcing terms are

time-independent. The frequency of fluctuations is partially related to model forcing. The inclusion of the R_b criterion also created larger mixing rates, hence larger diffusivities, and smaller near-surface vertical gradients in modeled velocity and temperature, all physically unrealistic.

Chapter 4

A Model of Diurnal Mixing in the Upper Equatorial Pacific Ocean

Abstract

The observed unique properties of high shear, low gradient Richardson number, zero inertial rotation, and strong diurnal variations of the upper equatorial Pacific Ocean provide an ideal setting for testing models of turbulent mixing. In this paper we use simple one-dimensional critical-R_i models to simulate the diurnal cycle of turbulent transfers between the surface and the equatorial undercurrent and compare the results with observations. The models are driven by diurnal solar radiation and time-independent wind stress and other forcing terms obtained from a previous analysis of the long-term momentum and heat balances at 0°N, 152°W. Diurnal variations are examined after the model reaches a steady state.

The simulated diurnal cycle of turbulent mixing in the upper layer has two prominent phases: during the day, the solar insolation creates stratification that interrupts the strong turbulent transfers between the westward wind

and the eastward EUC core; during the night, the surface cooling restablishes their interaction through a 100-m deep water column. The diurnal cycle of turbulent dissipation compares well to the Tropic Heat 1984 measurements. Detailed differences, such as the faster downward penetration of mixing in the model than observed, are likely caused by the instantaneous removal of shear instability within each time step in the model.

The model uses only a local gradient Richardson number criterion to parameterize mixing. The inclusion of a bulk Richardson number criterion (as used in previous model simulations) distorts the turbulent mixing not only in the case of steady forcing (Luan *et al.*, 1993b) and also in this case of diurnal solar radiation. The model periodically (7 days on average) results in an intense mixing event, then allows the gradual build-up of shear until the next catastrophic mixing event (even when all forcing terms are time-independent). The model produces smaller mean vertical gradients and highly intermittent time series of modeled velocity and temperature near the surface. It seems inconsistent to include both the bulk and the gradient Richardson number as mixing criteria in a model of turbulence.

4.1 Introduction

Strong diurnal cycles of currents, temperature, and dissipation of turbulent kinetic energy, were detected during Tropic Heat measurements of November 1984 (TH84) at 140°W in the upper equatorial Pacific (Gregg *et al.*, 1985; Moum and Caldwell, 1985; Chereskin *et al.*, 1986; Toole *et al.*, 1987; Peters *et al.*, 1988; Dillon *et al.*, 1989, Moum *et al.*, 1989). During daytime

when solar heating stablized the upper layer, only weak turbulent dissipation was detected and was limited to the top 10 meters most of that time. During nighttime when surface cooling deepened the surface mixed layer and destablized the flow further down, dissipation of order $10^{-7}\,m^2\,s^{-3}$ was observed to extend to depths of 80 m. The observed dissipation rate on the equator was 100 times larger with much deeper penetration below the nighttime mixed layer depth than at mid-latitides (Shay and Gregg, 1986; Price *et al.*, 1986).

The upper equatorial Pacific was observed to be strongly sheared vertically, with surface heating, a westward wind stress, a thermocline, an energetic equatorial undercurrent (EUC) with a maximum speed at about 120 m (Knox and Halpern, 1982; Gregg *et al.*, 1985; Moum and Caldwell, 1985). The gradient Richardson number, R_i, was low and close to its critical value, $R_{ic} = 0.25$, in the upper water column as deep as 100 m, another property rarely seen in the mid-latitudes.

The long-term steady state of the upper equatorial Pacific Ocean is similar to the state observed during the short-term cruises (Fig. 22). A recent study of data at 152°W showed high shear and low R_i (also close to 0.25) in the upper 80 m, implying persistent strong turbulent mixing at the equator on a long-term basis (Luan *et al.*, 1993a).

The properties of high shear, low Richardson number, and zero Coriolis force, in the upper equatorial Pacific, provide the motivation to test models of turbulence and improve our knowledge of mixing processes in the ocean. The model of Price *et al.* (1986) (hereafter, PWP) is a simple critical-R_i model based upon the critical Richardson number (shear instabitlities) as its mixing

mechanism. It is a one-dimensional, time-dependent, mixed-layer model of upper ocean, and requires the fewest adjustable parameters in models of its class. PWP used the model to simulate diurnal cycles of turbulent mixing at mid-latitude. Schudlich and Price (1992) (hereafter, SP) simulated the diurnal mixing cycle observed during the 12 days of TH84 at 140°W using the PWP model. Luan *et al.* (1993b) (hereafter, LPS) simulated the long-term mean vertical turbulent transfers of zonal momentum and heat at 154°W on the equator, using a modification of the PWP model, which includeed the steady-state dynamical terms of the momentum and heat balances derived from observations (Luan *et al.*, 1993a).

LPS showed that when the model included steady-state pressure gradient and advective terms and was initialized with the long-term mean values of zonal velocity and temperature, the model still rapidly adjusted itself during an initial 100 day period, then gradually transited to a steady state within the next 200 days. The modeled steady states are independent of initial conditions, but depend on the zonal pressure gradient, wind stress, zonal and vertical advection of zonal momentum and heat. In contrast, SP included no horizontal advection terms, began with observed profiles, and allowed their model to spin up for one day with the wind stress ramped from zero to their specified values in their 5 to 12-day simulations.

LPS found that the use of the bulk Richardson number (R_b) mixing (used by PWP and SP) in the LPS model caused multi-day (about 7 days) irregular fluctuations in the simulated time series of current and temperature down to the depth of EUC core. The inclusion of R_b mixing resulted in mean diffusvities near the surface much higher than oberved by LPS.

Then rise the following questions: What effects does the diurnal heating have on the steady state simulated by LPS? What does the simulated diurnal cycle of turbulent mixing look like, and how does it compare with the TH84 measurements? What are the effects of including R_b mixing on the diurnal cycles?

Our objectives are to model the diurnal cycle using the simple critical-R_i model by neglecting bulk Richardson number mixing and applying realistic forcing. We obtain from the model the steady-state averages, and compare them with observations and results from other models. In Section 4.2 we briefly summarize the governing equations and forcing of the model and compare with those used by SP. In Section 4.3 we describe the specific mixing model and show the differences from that of PWP used by SP. In Section 4.4 we show the effect of diurnal heating on the mean fields, examine the simulated diurnal cycle after the model reaches steady state, and compare it to observations of TH84. The effect of including the R_b mixing is examined in Section 4.5. Conclusions are given in Section 4.6.

4.2 Forcing

Luan *et al.* (1993a) studied the long-term balances of zonal momentum and heat at 152°W in the upper equatorial Pacific:

$$\frac{\partial \hat{U}}{\partial t} + \hat{U}\frac{\partial \overline{U}}{\partial x} + \overline{W}\frac{\partial \hat{U}}{\partial z} + \frac{\partial \overline{V'U'}}{\partial y} = -\frac{1}{\rho_\circ}\frac{\partial \overline{P}}{\partial x} - \frac{1}{\rho_\circ}\frac{\partial \hat{F}_m}{\partial z} \tag{4.1}$$

$$\frac{\partial \hat{T}}{\partial t} + \hat{U}\frac{\partial \overline{T}}{\partial x} + \overline{W}\frac{\partial \hat{T}}{\partial z} + \frac{\partial \overline{V'T'}}{\partial y} = -\frac{1}{\rho_\circ C_p}\frac{\partial \hat{F}_h}{\partial z} \tag{4.2}$$

$$\hat{\rho}(z) = \rho_\circ[1 + \alpha(\hat{T} - T_\circ)] \tag{4.3}$$

where x, y and z are positive eastward, northward and upward ($z = -h_b = -200\,\mathrm{m}$ at the bottom and $z = 0$ at the sea surface), respectively; U, V and W are the velocity components corresponding to the coordinates (x, y, z), respectively; and P is pressure, T is temperature; $F_m(z)$ is the vertical turbulent fluxe of zonal momentum; $F_h(z)$ is the vertical turbulent heat flux including the solar insolation. The constants are the specific heat of seawater C_p, thermal expansion coefficient α, reference density ρ_o, and reference temperature T_o, usually taken as the sea surface temperature. The quantities with overbars are time-independent (Fig. 22), given by Luan *et al.* (1993a), and those with hats are functions of t and z.

This study includes the upper 200 m of the ocean, as in LPS. The zonal pressure gradient is a time-independent Gaussian profile least-squares fit to the results of Mangum and Hayes (1984) with a surface value of $4.6 \times 10^{-7}\,\mathrm{m\,s^{-2}}$ and a depth scale of 107 m (Fig. 22). The vertical velocity is a cubic function of depth obtained from the inverse analysis of long-term balances of zonal momentum and heat by Luan *et al.* (1993a). It is also time-independent and non-negative (upwelling) with a maximum value of $2.7 \times 10^{-5}\,\mathrm{m\,s^{-1}}$ at 100-m depth and zero at the surface.

As in LPS, we include the zonal advection in the model, based on time-independent values of zonal gradients of zonal velocity and temperature computed from data (Fig. 22) (Luan *et al.*, 1993a), and time-independent values of meridional meso-scale eddy transports of zonal momentum and heat (Fig. 22) (Bryden and Brady, 1989). The zonal advection of heat is one of the two dominant terms in the heat balance (the other is vertical advection) between the depths of 90 and 190 m.

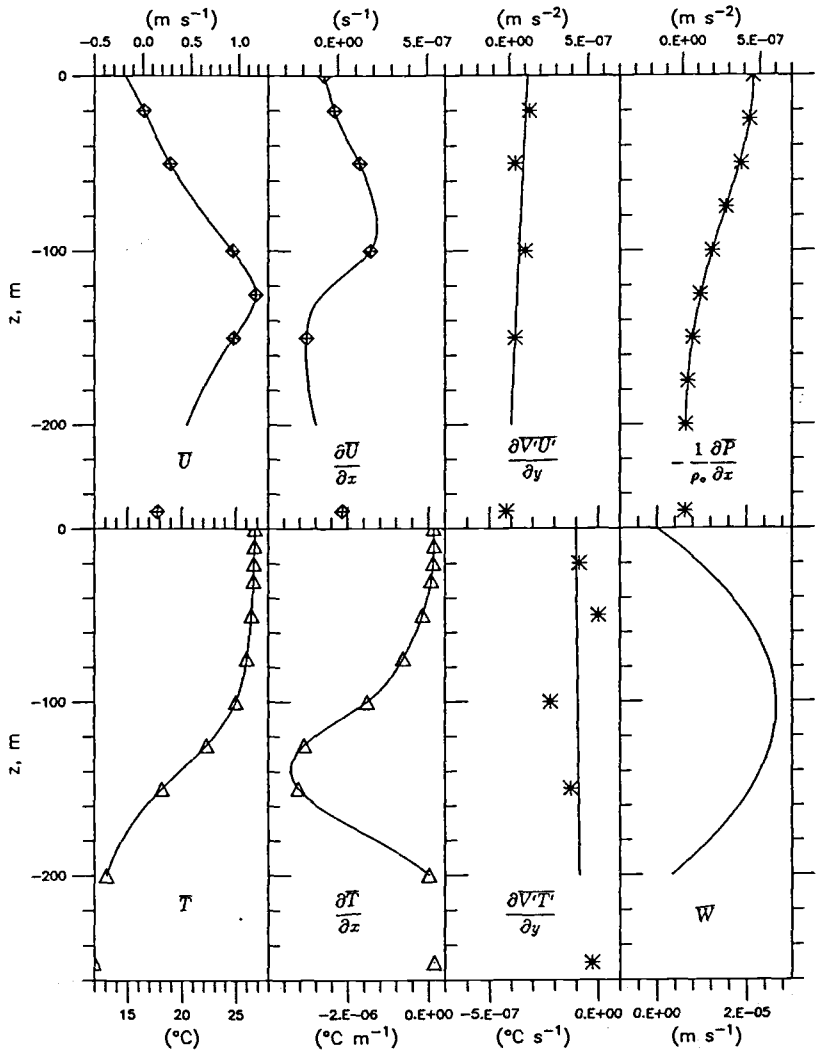

Figure 22. Long-term mean zonal velocity $\overline{U}$ and its zonal gradient $\frac{\partial \overline{U}}{\partial x}$, temperature, $\overline{T}$, its zonal gradient, $\partial \overline{T}/\partial x$, meridional eddy transports of zonal momentum, $\partial \overline{V'U'}/\partial y$ and heat, $\partial \overline{V'T'}/\partial y$, the zonal pressure gradient, $-\rho_o^{-1}\partial \overline{P}/\partial x$, and vertical velocity $\overline{W}$ (from Luan *et al.*, 1993a). Data points are marked. The data of each observed quatity are interpolated using fourth order splines vertically.

The vertical turbulent fluxes of zonal momentum, $\hat{F}_m$, and heat, $\hat{F}_h$, defined positive upward, are determined by the model of mixing described in the next section, except at the surface, where they are the specified wind stress and heat flux at the surface, respectively. A constant (negative westward) wind stress is used, with a climatological mean value of $\tau_\circ^x = -0.048\,\mathrm{N\,m^{-2}}$. (Wyrtki and Meyers, 1976; Esbensen and Kushnir, 1981; Hellerman *et al.*, 1983; Luan *et al.*, 1993a). That is, $\hat{F}_m(t, z = 0) = \overline{F}_m = -\tau_\circ^x = -0.048\,\mathrm{N\,m^{-2}}$. The vertical heat flux $\hat{F}_h$ is composed of two parts:

$$\hat{F}_h = \hat{I} + \hat{\mathcal{F}}_h \tag{4.4}$$

where $\hat{\mathcal{F}}_h$ is due to turbulent mixing determined, as $\hat{F}_m$, according to the model described in next section, and $\hat{I}$ is the solar insolation described below. Turbulent diffusivities, $\hat{K}_m$ and $\hat{K}_h$, are defined, repectively, by

$$\hat{F}_m = -\rho_\circ \hat{K}_m \frac{\partial \hat{U}}{\partial z} \tag{4.5}$$

$$\hat{F}_h(z) = -\rho_\circ C_p \hat{K}_h \frac{\partial \hat{T}}{\partial z} = \hat{I} + \hat{\mathcal{F}}_h \tag{4.6}$$

The components of $\hat{\mathcal{F}}_h$ at the surface are

$$\hat{\mathcal{F}}_h(t, z = 0) = Q_l + Q_s + Q_b \tag{4.7}$$

where Q_l, Q_s, and Q_b, are the latent heat flux, sensible heat flux, and back radiation from the sea surface. The solar insolation, $\hat{I}$, is modeled with a double exponential depth dependence

$$\hat{I}(z, t) = Q_i(t)\,(I_1 e^{z/\lambda_1} + I_2 e^{z/\lambda_2}) \tag{4.8}$$

where, subscripts 1 and 2 refer to the short- and long-wave components of insolation, respectively. We use typical values for the equatorial water (Jerlov type IB): $I_1 = 0.6$ and $\lambda_1 = 1\,\mathrm{m}$, and $I_2 = 1 - I_1 = 0.4$ and $\lambda_2 = 17\,\mathrm{m}$ (Jerlov, 1968; Paulson and Simpson, 1977). When $\lambda_1 \to \infty$ and $\lambda_2 \to \infty$, the solar irradiance in Eq. (4.8) becomes non-penetrative, *i.e.*, the incoming solar insolation is completely absorbed by the sea surface, as used by LPS with a constant $\hat{F}_h$. Temporal variation of the solar heat flux is modeled by $Q_i(t)$, which is primarily determined by the height of the sun. The climatology in Weare *et al.* (1981) gave a mean solar radiation of about $\overline{Q_i} = -240\,\mathrm{W\,m^{-2}}$ in the region of interest. From the analysis of Luan *et al.* (1993a), a slightly larger value is used, $\overline{Q_i} = -270\,\mathrm{W\,m^{-2}}$. The diurnal variation is idealized to be sinusoidal during a 12-hour day, with a peak $Q_i = -850\,\mathrm{W\,m^{-2}}$ at noon, and $Q_i = 0$ during a 12-hour night (Fig. 23). The sum of heat fluxes other than solar heating at the sea surface is $Q_l + Q_s + Q_b = 170\,\mathrm{W\,m^{-2}}\,\mathrm{W\,m^{-2}}$ (cooling), or

$$\hat{\mathcal{F}}_h(t, z = 0) = 170\,\mathrm{W\,m^{-2}}\,\mathrm{W\,m^{-2}} \tag{4.9}$$

which does not vary with time. Thus, the net heat flux at the surface

$$\hat{F}_h(t, z = 0) = Q_{net} = Q_i + Q_l + Q_s + Q_b \tag{4.10}$$

has a daily average of $\overline{Q}_{net} = -100\,\mathrm{W\,m^{-2}}$ (heating) (Luan *et al.*, 1993a), which was used by LPS as a constant surface forcing. One diurnal cycle of Q_i, and the constant $Q_l + Q_s + Q_b$, are shown in Fig. 23.

At the bottom, $\hat{U}$, $\hat{T}$ are fixed at their long-term averages (Luan *et al.*, 1993a). We initialize the model with the long-term mean values of observed zonal velocity and temperature.

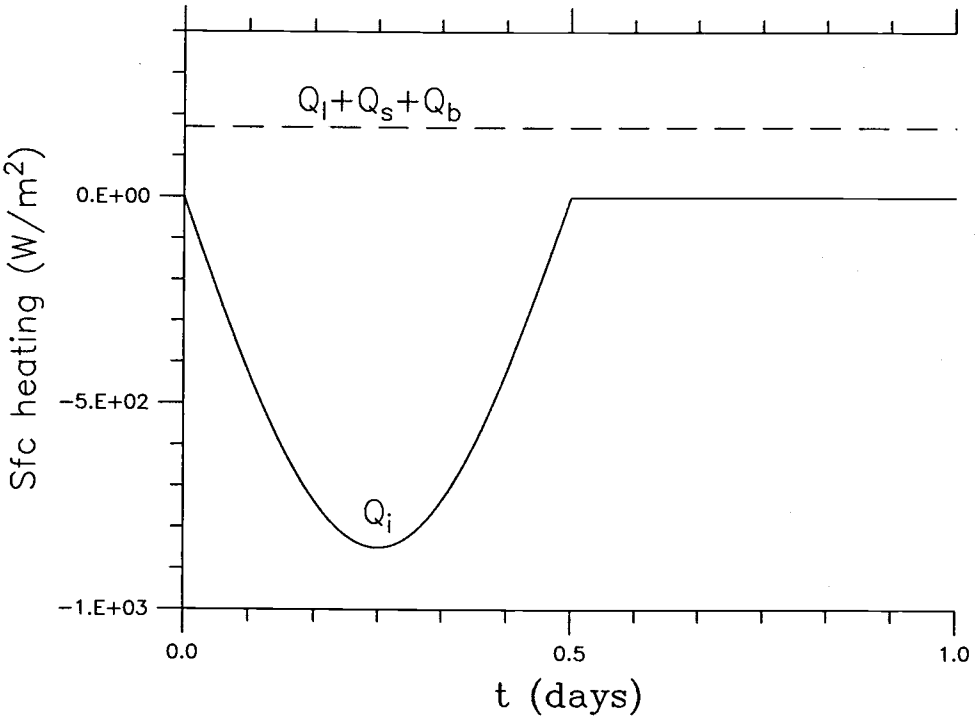

Figure 23. One diurnal cycle of solar insolation at the sea surface. Solar insolation, Q_i, which is sinusoidal during a 12-hour daytime with a peak of 850 W M^{-2} at noon and zero during the 12-hour night. The sum $Q_l + Q_s + Q_b$ has a constant heat loss of 170 W M^{-2}. The daily average of net surface heat flux $\overline{Q}_{net} = \overline{Q}_i + Q_l + Q_s + Q_b = -100$ W M^{-2} (net heating).

4.3 Critical-R_i model

The vertical turbulent fluxes of zonal momentum, $\hat{F}_m$, and heat, $\hat{\mathcal{F}}_h$, are determined by the model of mixing. The critical-R_i mixing model employed here is described in detail in LPS. It is summarized here. Aspects of the model important for diurnal simulation are elaborated here.

In the model (LPS), vertical mixing occurs at each time step until two instabilities are removed:

$$\frac{\partial \hat{\rho}}{\partial z} > 0, \tag{4.11}$$

$$R_g(z) = -\frac{g}{\rho_o}\frac{\hat{\rho}_z}{\hat{u}_z^2 + \hat{v}_z^2} < 0.25, \tag{4.12}$$

where the meridional component of velocity, $\hat{v}$, is not used in this paper, nor in LPS and SP. The first is convective adjustment which simulates mixing due to density inversion. The second is the local gradient Richardson number mixing which models shear instability mixing. The first instability produces a slab-like surface mixed layer during surface cooling, while the second smoothes the discontinuities of velocity, density, and temperature, and yields sheared transition layers. The maximum depth at which shear instability adjustment occurs is called the transition layer depth. The model also includes a background diffusion of both zonal momentum and heat with a constant diffusivity $K_b = 1 \times 10^{-5}\,\mathrm{m^s\,s^{-1}}$ based on analysis in Luan *et al.* (1993a).

The full version of the PWP model as used by SP included the bulk Richardson number mixing, a criterion given by

$$R_b(z) = -\frac{g}{\rho_o}\frac{\Delta\hat{\rho}\,h}{(\Delta\hat{u})^2 + (\Delta\hat{v})^2} < 0.65, \tag{4.13}$$

where the meridional component of velocity, $\hat{v}$, is not used in this paper, nor in LPS and SP. Bulk-R_i mixing was applied after the convective adjustment but before the gradient R_g adjustment described above. Here, h is the depth of the mixed layer, and Δ is the difference in density or currents between the bottom grid of the mixed layer and that immediately below, and the mixed layer is defined as the thickness of surface layer of uniform density after the first condition is met but before the third is (see SP). The LPS model included the R_b criterion as an option for purpose of model comparison.

The model evaluates $\hat{F}_m$ and $\hat{F}_h$ at the end of each time step $t = (n+1)\Delta t$ using

$$\begin{aligned}
\hat{F}_m^n(z) &= \hat{F}_m^n|_{z=-200} - \rho_\circ \int_{-200}^{z} \left[\frac{\hat{U}^{n+1} - \hat{U}^n}{\Delta t} \right. \\
&\quad \left. + \hat{U}^n \frac{\partial \overline{U}}{\partial x} + \overline{W} \frac{\partial \hat{U}^n}{\partial z} + \frac{\partial \overline{V'U'}}{\partial y} + \frac{1}{\rho_\circ} \frac{\partial \overline{P}}{\partial x} \right] dz \qquad (4.14) \\
\hat{F}_h^n(z) &= \hat{F}_h^n|_{z=-200} - \rho_\circ C_p \int_{-200}^{z} \\
&\quad \left[\frac{\hat{T}^{n+1} - \hat{T}^n}{\Delta t} + \hat{U}^n \frac{\partial \overline{T}}{\partial x} + \overline{W} \frac{\partial \hat{T}^n}{\partial z} + \frac{\partial \overline{V'T'}}{\partial y} \right] dz \qquad (4.15) \\
\hat{F}_m^n|_{z=-200} &= -\rho_\circ K_b \frac{\partial \hat{U}^n}{\partial z}|_{z=-200} \qquad (4.16) \\
\hat{F}_h^n|_{z=-200} &= -\rho_\circ C_p K_b \frac{\partial \hat{T}^n}{\partial z}|_{z=-200} \qquad (4.17)
\end{aligned}$$

where Δt is time step, Δz is vertical grid size, and the superscript n represents evaluation at $t = n\Delta t$. Subsequently, we evaluate the turbulent heat flux according to (4.4)

$$\hat{\mathcal{F}}_h^n(z) = \hat{F}_h^n - \hat{I}^n \qquad (4.18)$$

Turbulent diffusivities are evaluated from

$$\hat{K}_m^n(z) = -\frac{\hat{F}_m^n}{\rho_\circ \frac{\partial \hat{U}^n}{\partial z}} \tag{4.19}$$

$$\hat{K}_h^n(z) = -\frac{\hat{F}_h^n}{\rho_\circ C_p \frac{\partial \hat{T}^n}{\partial z}}. \tag{4.20}$$

The dissipation rate of turbulent kinetic energy, ε, is calculated from

$$\varepsilon = \mathcal{P} + \mathcal{B} \tag{4.21}$$

where the shear production $\mathcal{P} = \frac{1}{\rho}\hat{F}_m \frac{\partial \hat{U}}{\partial z}$ and the buoyancy production $\mathcal{B} = -\hat{\mathcal{F}}_h g\alpha/(\rho_\circ C_p)$. Hence, at the end of each time step, the dissipation rate can be computed from the turbulent fluxes evaluated above

$$\varepsilon^n(z) = \frac{1}{\rho}\hat{F}_m^n \frac{\partial \hat{U}^n}{\partial z} - \frac{g\alpha}{\rho_\circ C_p}\hat{\mathcal{F}}_h^n \tag{4.22}$$

4.4 Results and comparison with observations

The critical-R_i model with diurnal heating as described above was run for 600 days with a time step $\Delta t = 15$ min and vertical grid spacing $\Delta z = 1$ m. The results show a 100-day spin-up (a time scale related to the vertical velocity) followed by a 300-day transit to steady state, the same features described by LPS for constant heating.

a. Steady state

Fig. 24 shows the averages of the zonal velocity, temperature, turbulent fluxes and diffusivities, over last 100 days for simulations with diurnal and constant heating. The zonal velocity and temperature are compared with the

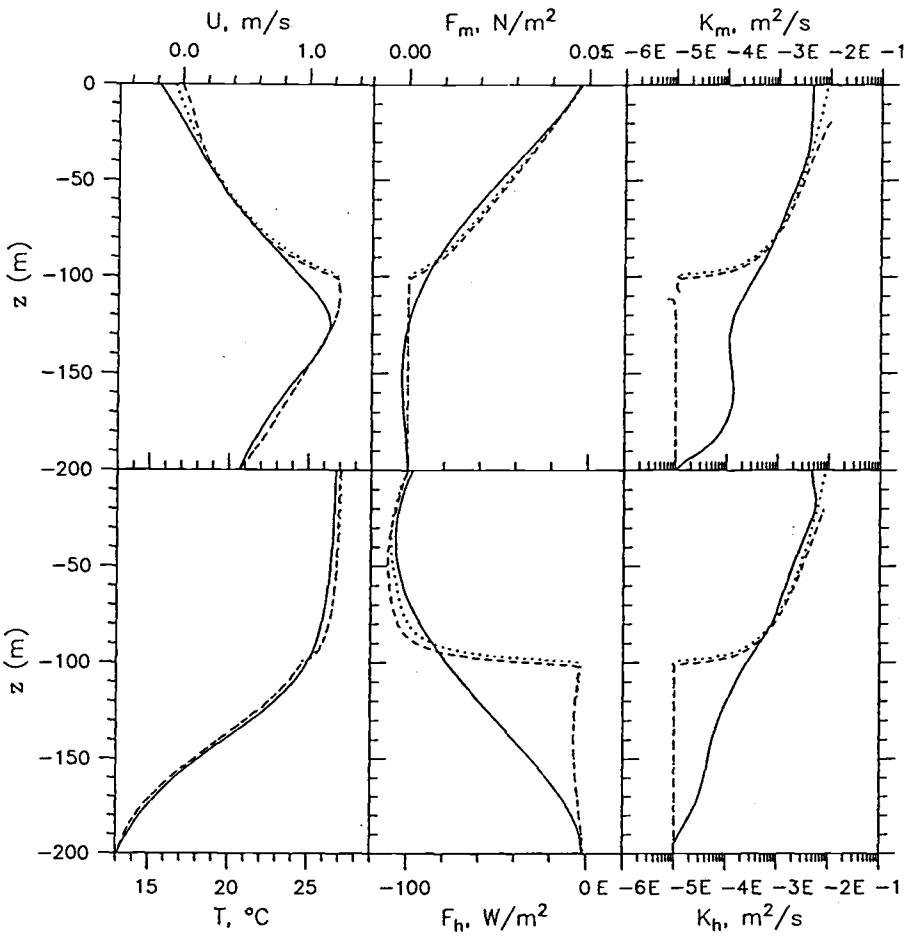

Figure 24. Averages of the zonal velocity, temperature, turbulent fluxes and diffusivities, over last 100 days for simulations with diurnal (dashed) and constant (dotted) surface heating, compared with the long-term mean zonal velocity and temperature (solid), also used as initial conditions in both simulations (Fig. 22), and the inverse solutions for turbulent fluxes and diffusivities (solid) obtained by Luan *et al.* (1993a).

long-term mean observations (Fig. 22), which are used as initial conditions. Comparison os also make with the inverse solutions for turbulent fluxes and diffusivities obtained by Luan *et al.* (1993a).

The two steady-state simulations (Fig. 24), one with diurnal surface heating and the other with constant heating, are very similar. Surface velocity and temperature differ by only $0.06\,\mathrm{m\,s^{-1}}$ and 0.05°C, respectively. Near-surface mixing is slightly stronger in the diurnal simulation as is shown by smaller vertical gradients of velocity and temperature, larger fluxes of momentum and heat and larger values of diffusivities.

Both simulations shown in Fig. 24 agree reasonably well with the observed velocity and temperature profiles and with the fluxes and diffusivities from the inverse analysis (Luan *et al.*, 1993a). The differences between the diurnal and observed surface velocity and temperature are $0.2\,\mathrm{m\,s^{-1}}$ and 0.3°C, respectively. The main disagreement occurs near the base of the critical-R_i mixing layer at 100 m, below which mixing occurs only as the result of constant background diffusion. The discountinuity in mixing introduces discountinuities in all of the profiles. In the real ocean, non-steady forcing and shear instabilities due to internal waves acts to smooth the profiles below 100 m. The differences between the simulations and the observations are probably insignificant in the upper 90 m.

These results show that the diurnal variation in surface heat fluxes have little effect on the simulated steady state of current and temperature. The small effects are due to the nighttime cooling phase of the diurnal cycle, which increases average turbulent mixing by a small amount above the EUC.

b. Diurnal cycle

Properties of the diurnal cycle in the upper equatorial Pacific are shown in Figs. 25, 26 and 27. The time series of the hourly-averaged net surface heat flux and time-depth contours of zonal velocity and temperature is in Fig. 25, the turbulent fluxes in Fig. 26, and the turbulent dissipation rate in Fig. 27, from the last two days of the 600-day simulation to examine the properties of the diurnal cycle in the upper equatorial ocean. Since the model reaches steady state after 300 days, any effects of the transition phase are avoided. Our model day begins at sunrise. The simulated variables are averaged for all the time steps carried out in the hour preceding each hourly output.

The daytime phase of the diurnal cycle in the simulation is similar to that at mid-latitudes, in agreement with SP. In the first hours after sunrise, the net surface heat flux gradually turns from net cooling to net heating and convection is shut down. Most of the solar insolation is absorbed by the top one meter. As the day progresses, solar insolation increases, and the upper layer is stabilized. The temperature field shows warming throughout the upper 50 m. Meanwhile, the continuous westward wind, althought partly balanced by the zonal pressure gradient, causes accumulation of shear in the surface layer. Soon, shear instabilities develop and mix the westward momentum and heat of the surface layer to slightly greater depths. Below such depths, the water is decoupled from the westward wind, and the eastward currents are accelerated. This in turn enhances wind stirring by increasing shear beneath the depth of wind stirring. Such a phenomenon is confirmed by the

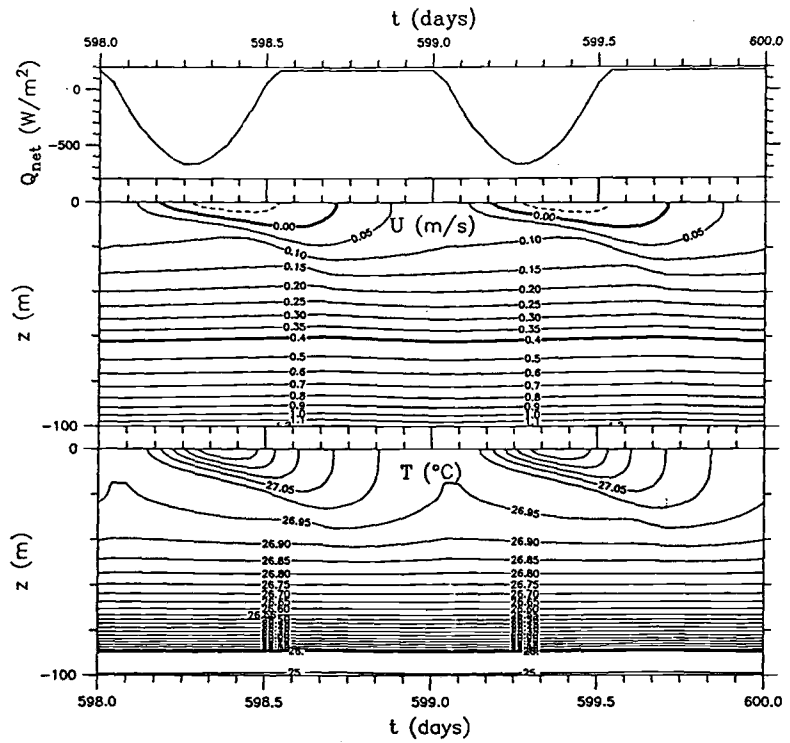

Figure 25. Time series of hourly-averaged net heat flux across the sea surface, zonal velocity and temperature in the upper 50 m, from the last two days of simulation. During daytime, stratification in the surface layers traps higher shear; at dusk surface cooling causes convection and the region of high shear moves downwards through mixing due to shear instabilities. High shear at the bottome of the mixed layer, defined as the depth at which temperature is 0.1°C smaller than the sea surface, results in high rates of production of turbulent kinetic energy, and hence, dissipation maxima. By the next dawn, stratification and shear again start to build up in the surface layer due to solar heating.

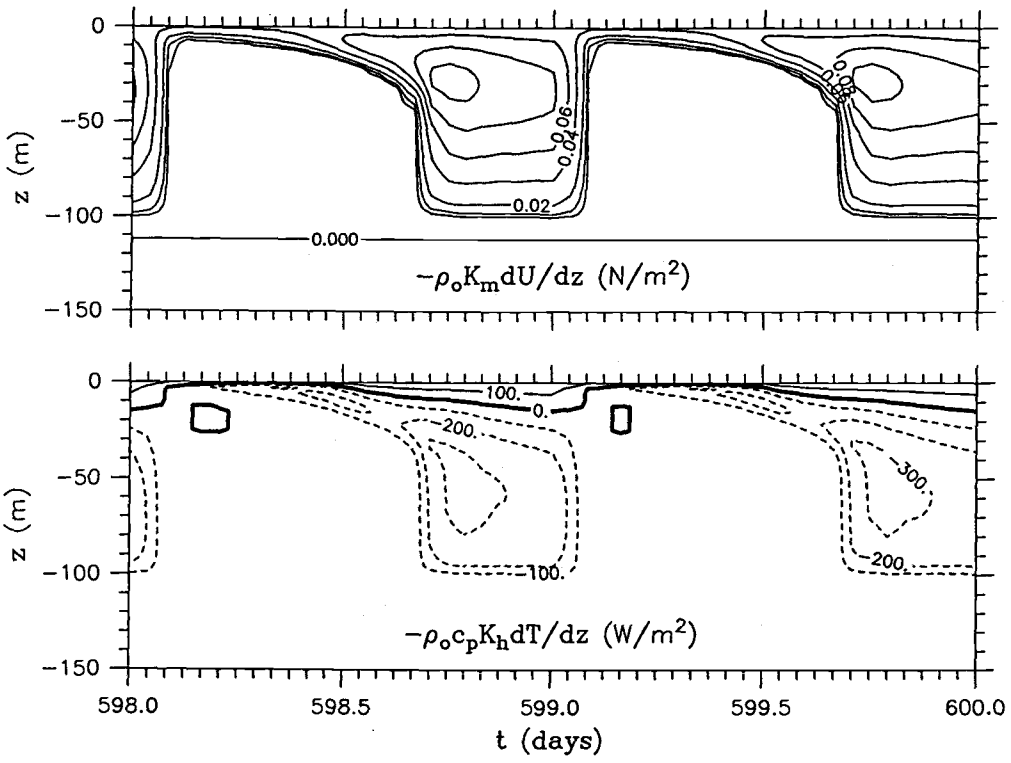

Figure 26. Time series of hourly averaged turbulent fluxes of zonal momentum and heat (excluding solar heat flux), from the last two days of simulation. During daytime, weak turbulent mixing is trapped in the top few meters, none below. During nighttime, strong turbulence occurs well below the 50 m surface mixed layer and penetrate as deep as 100 m, just above the depth of zonal velocity maximum.

daytime turbulent fluxes (Fig. 26) and dissipation rate (Fig. 27), which show the depth of wind stirring to increase from about 5 m at the beginning to about 15 m at the end of the daytime phase.

The amplitude of diurnal warming at the surface is 0.32°C (Fig. 25). For the 12-hour day of solar insolation, surface warming starts two hours after sunrise, and continues until mid-afternoon. At that time, SST begins to decrease due to mixing and deepening of the surface layer. Thus, warming of the water at the very surface occurs over about a quarter of a day, followed by cooling for the reminder. SP also reported a similar timing of surface warming, and a marked saw-toothed time series of their simulated sea surface temperature.

Westward surface currents are present for about half a day, because the westward wind is partially balanced by the zonal pressure gradient in the surface layer. The westward jet at the surface appears during the 13-hour period starting two hours before local noon and ending an hour before midnight (Fig. 25). The westward jet maximum of $0.08\,\mathrm{m\,s^{-1}}$ occurs at mid-afternoon, exactly when sea surface temperature reaches its maximum. The temporal change of surface velocity is locked in phase with that of surface temperature at all times. The amplitude of the diurnal variation of the surface current is $0.17\,\mathrm{m\,s^{-1}}$.

Daytime values of the turbulent fluxes and dissipation rate are small except in the top 5 to 15 m where wind stirring is active (Figs. 26 and 27. The surface mixing layer shallows to the top few meters from about 100 m within a couple of hours after sunrise, and deepens slowly during the daytime, due to the build-up of wind-driven shear at the base of the mixing layer.

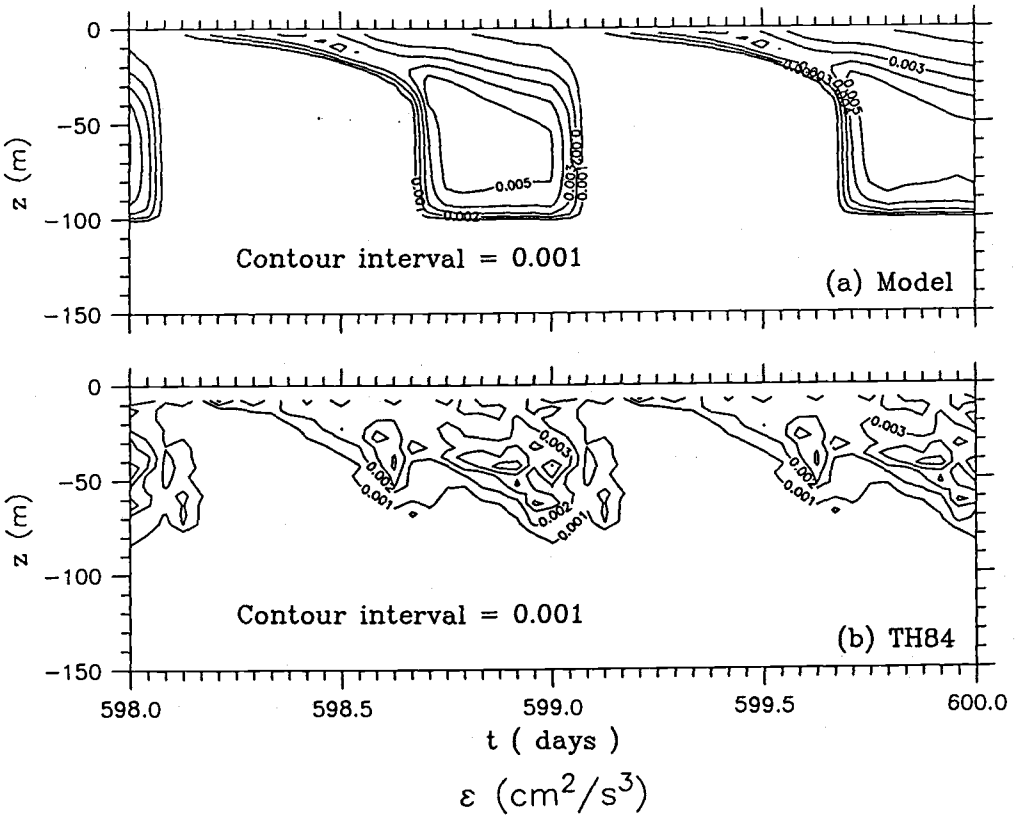

Figure 27. Modeled dissipation rate compared with Tropic Heat 84 measurements. Time series of (a) hourly averaged dissipation rate of turbulent kenetic energy from the last two days of simulation, compared to (b) that of a canonical day formed by averaging 8 days of measurements at 140°W on the equator during Tropic Heat 84. The model yields the diurnality of the turbulent dissipation rate but with larger magnitudes and faster downward propagation of phase during nighttime.

About an hour before sunset, the total surface heat flux changes sign. Together with continued wind mixing, surface cooling destabilizes the upper layer and convection deepens the surface mixing layer. The shear maximum gradually migrates down, tracking the base of the surface mixing layer (Fig. 25). The downward migration of the shear maximum is accompanied by the downward migration of large values of turbulent fluxes and dissipation (Figs. 26 and 27).

Within the two hours before midnight, mixing pierces through a subsurface layer of above-critical gradient Richardson number and erased all the changes accumulated in the upper layer during daytime. At that time, wind stress and surface heat flux establish their exchange of zonal momentum and heat with the EUC, and the surface mixing layer deepens to about 100 m. This long channel of exchange is nearly "short-circuited" because the gradient Richardson number in that water column is near or at its critical value of 0.25 (not shown).

Between midnight and sunrise, eastward momentum is transferred upward at rates as high as $0.1\,\mathrm{N\,m^{-2}}$, to balance the westward momentum inserted into the surface layer by a westward wind stress of $0.048\,\mathrm{N\,m^{-2}}$ (Fig. 26). Meanwhile, the ocean loses heat at the surface and meanwhile transports heat downward, which has been heated during daytime, at rates as high as $300\,\mathrm{W\,m^{-2}}$ (Fig. 26). The simulated turbulent momentum transfer cannot penetrate through the EUC core where the gradient Richardson number is infinite by definition, evidenced by the 112-m depth of zero vertical flux of zonal momentum.

The process of deep (100-m) mixing lasts about 8 to 9 hours before being interrupted a couple of hours after sunrise the next morning. At that time, the depth of the (convective) surface mixed layer reaches its maximum depth of 18 m.

In summary, the diurnal cycle of turbulent mixing has two prominent phases. The change from surface cooling to surface heating interrupts the deep nighttime turbulent transfers. The subsequent switch to surface cooling re-establishes the growth of a surface mixing layer to a depth of 100 m during nighttime.

c. Comparison with observations

The dissipation rate on the equator at 140°W was measured during a 12-day period in 1984 (TH84, Moum *et al.*, 1989). During this period, the westward wind stress was twice the value used in our model, the peak solar insolation was about $1000\,\mathrm{W\,m^{-2}}$, and the other heating terms produced a nearly constant heat loss of $200\,\mathrm{W\,m^{-2}}$ (Moum *et al*, 1989). The daily average of total surface heat fluxes were about $120\,\mathrm{W\,m^{-2}}$, close to the value of $100\,\mathrm{W\,m^{-2}}$ used in our model simulation. We discard the first four days of measurements which are affected by strong advectiv processes, and average the measured dissipation rate over the last 8 days to form a cannonical diurnal cycle. We plot two of such cannonical cycles in Fig. 27.

The simulated turbulent dissipation rate has values and time-depth contours similar to the observed (Fig. 27). They both demonstrate similar diurnal cycles, have a magnitude of $5 \times 10^{-7}\,\mathrm{m^2\,s^{-3}}$, and penetrate well below the surface layer for periods of 8 to 12 hours during nighttime. However,

there are some differences. TH84 results show a more gradual downward penetration of dissipation during nighttime. The penetration of dissipation observed during TH84, almost linear in time, continues until sunrise when it reached a maximum depth of 85 m. Then turbulent activities diminished in the 2 to 4 hours after sunrise. On the other hand, the nighttime phase of the model results show a linear propagation for the first 3 to 4 hours, and a rather abrupt penetration to its maximum depth of 100 m within the next hour, followed by a continuation of the maximum dissipation before sunrise. Turbulent activities end within the first 2 hours after sunrise, sooner than the measurements show.

In summary, the simulated diurnal cycle of turbulent mixing is consistent with that of the measured during TH84, despite some differences. The differences suggest that the parameterization of turbulence in the model may yield faster downward penetration of mixing. One of the possible causes for the faster penetration of mixing is the instantaneous removal of shear instability, or the Kelvin-Helmholtz instabilities, at each time step in the model. In reality, even though the time scale for a single KH overturn may be the buoyancy period, that instability may induce others for which several periods may be needed for mixing to be completed. Priliminary efforts to modify the model to include this more gradual mixing have shown promising results.

4.5 Inclusion of bulk-R_i mixing

Bulk Richardson number mixing was used in PWP and SP. The model used in this paper has excluded the R_b mixing mechanism. LPS tested the inclusion of R_b mixing with time-independent forcing. They reported fluctuations with intervals of approximately 7 days were accompanied by very energetic "mixing" events associated with the R_b instabilities. R_b criterion also caused much more excessive mixing in the model. Similarly, SP showed a marked saw-tooth type of changes in their time series of simulated velocity and temperature. They reported that ensemble-averages of simulated dissipation rate modeled the diurnal variaton of TH84 measurements well. But their hourly results showed extreme intermittency, which was somewhat sensitive to the size of time step of the model (SP).

We repeat the simulation including the R_b criterion with diurnal surface heating and all other forcing unchanged from above. Despite the presence of diurnal heating, the contours of daily averaged velocity and temperature are overwhelmed by the energetic similar 7-day bursts of mixing reaching as deep as the EUC core (Fig. 28).

One of the energetic 7-day bursts occurs just before midnight on day 594, as shown in the ten-day time series of hourly averaged zonal velocity, temperature, turbulent fluxes and dissipation (Fig. 29). Before the burst, there is a gradual migration of relatively large vertical shear and stratification toward the surface layer. Near midnight on day 594, the bulk Richardson number R_b becomes critical, and the R_b mixing adjustment produces a uniform surface layer 80-m deep, and perturbs layers as deep as the EUC core at 118 m.

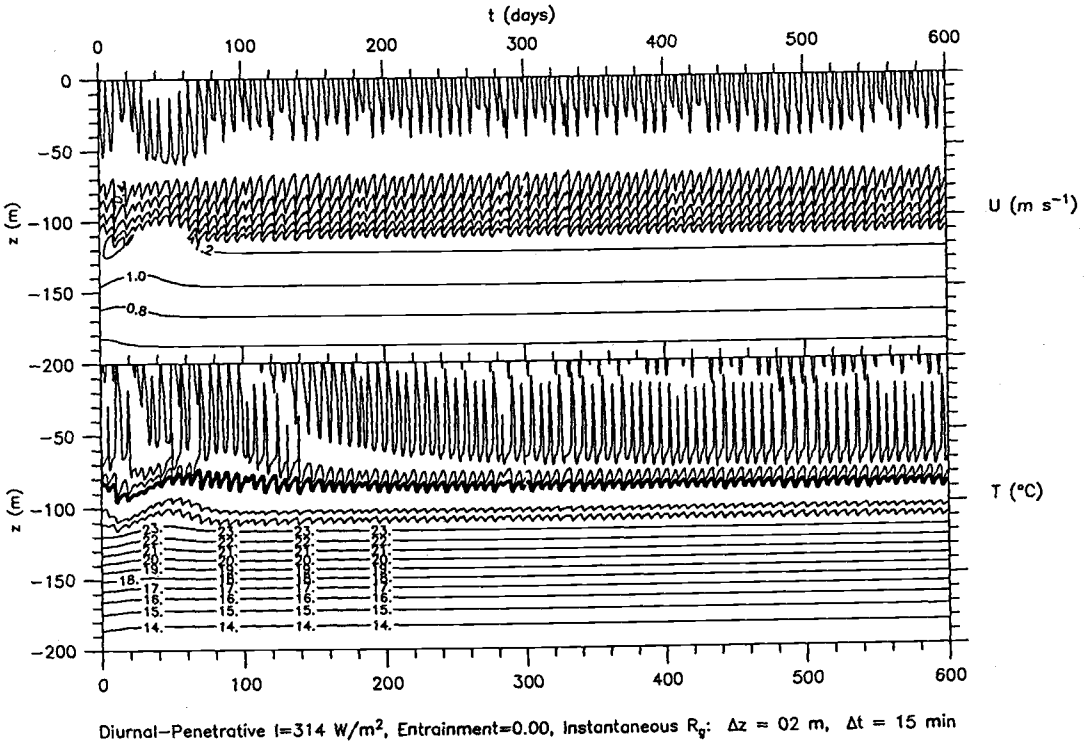

Figure 28. Time series of simulated zonal velocity and temperaure with the same forcing as described in Section 4.2 but with bulk Richardson number mixing included. The results show the 7-day fluctuations similar to those with constant surface heating (Luan *et al.*, 1993b).

The R_b mixing adjustment pushed down the undercurrent core by more than 10 m. After the adjustment, the vertical shear and stratification start their gradual upward migration from the base of the new mixed layer to the surface layer. The migration continues for about 7 days when the next energetic R_b burst of mixing occurs.

There are three other bursts with moderate strengths, one in each day of 591, 597, and 599, during this 10-day period (Fig. 29). There are also bursts with small magnitudes occurring from late morning to late afternoon on a daily basis (Fig. 29). Each of these bursts of mixing are due the R_b mixing mechanism. None of the diurnal cycles are the same due to the irregular occurence of the R_b instabilities on time scales of multiple days.

Bursts of mixing usually occur with a duration of an hour or so. There is good similarity between the bursts we observe in this simulation and the extreme intermittence in the short-term (hourly) variation of dissipation reported by SP. The bursts cause the saw-tooth shaped time series in the diurnal variations of simulated velocity and temperature, just as SP showed in their time series.

The inclusion of bulk Richardson number mixing also distorted the diurnal circle (Fig. 29). Turbulent transfers are usually subdued during the next day or two following each major burst. A reversal of the upward transfer of eastward momentum even occurs between the depths of 50 and 70 m for about 8 hours (from late morning to late afternoon) the day after the biggest burst. Long-term averages of the simulation show a surface layer of smaller vertical gradients. Thus, it is suggested that mixing is overdone by the critical R_b adjustments. Only one of the ten days, *i.e.*, that before the

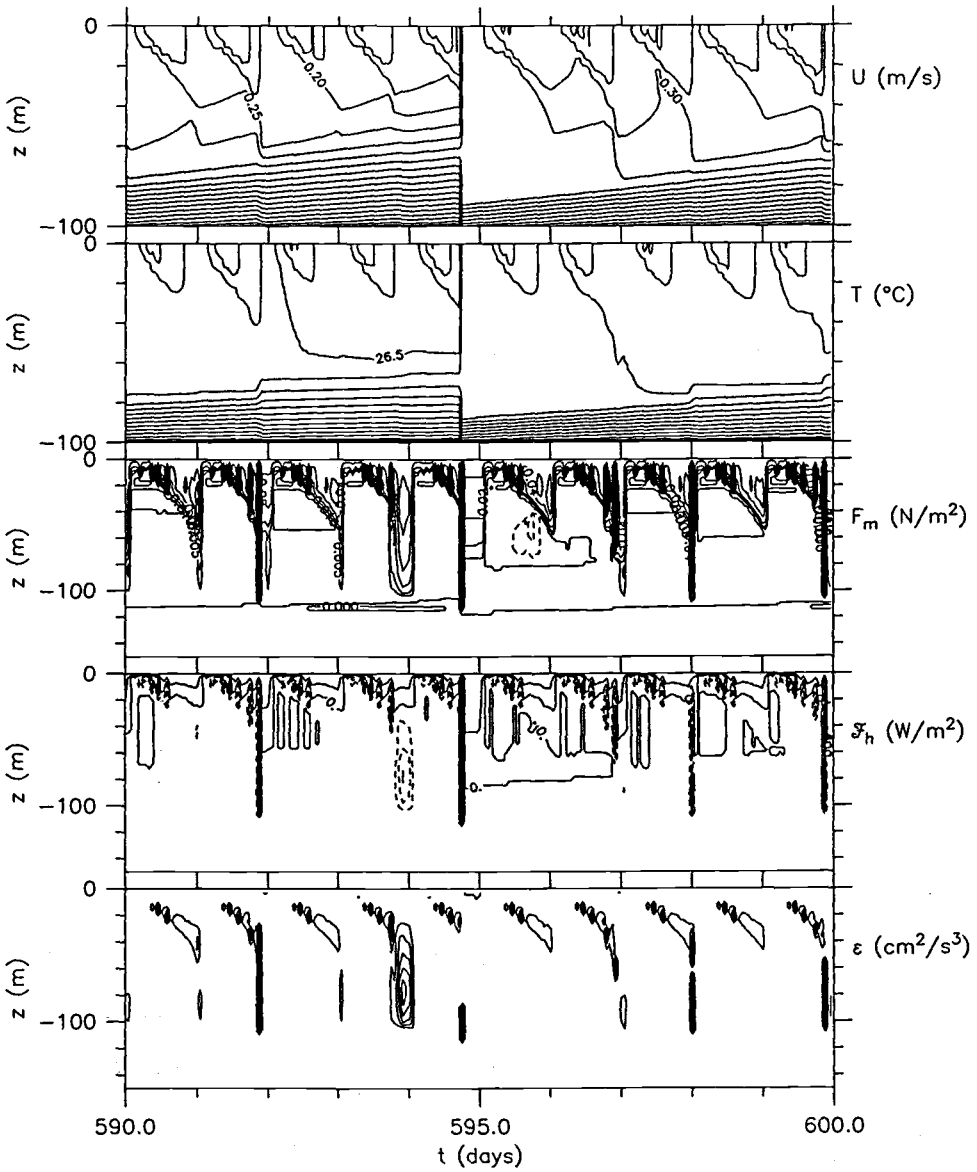

Figure 29. Time series of hourly averaged zonal velocity, temperature, turbulent fluxes of zonal momentum and heat (excluding solar heat flux), and dissipation rate of turbulent kenetic energy, from the last two days of simulation with bulk Richardson number mixing included shown in Fig. 28.

biggest burst, shows a time series of turbulent mixing close to those shown in Figs. 25 to 27 from the simulation with R_b mixing excluded. Therefore, we conclude that the shear instability mixing, which has sound physical and experimental basis, can be fully represented by gradient Richardson number mixing, and that the inclusion of bulk Richardson number mixing leads to highly unrealistic results.

4.6 Conclusions

Diurnal cycles in the upper equatorial Pacific are studied by use of a simple critical-R_i model of turbulence. First the model was spun up with constant forcing obtained from analysis of long-term zonal momentum and heat balances at 152°W in the upper equatorial Pacific Ocean. Model mixing with diurnal surface heating is slightly stronger above the equatorial undercurrent core than that without diurnal variation.

The simulated diurnal cycle of turbulent mixing in the upper layer has two prominent phases. Solar insolation interrupts the strong turbulent transfers in the upper 100 m during daytime. Surface cooling re-establishes mixing through the upper 100 m by midnight. Diurnal forcing at the surface cannot, by definition, overcome the mixing barrier at the EUC core, where large values of gradient Richardson number shut down the turbulent transfers.

The simulated diurnal cycle of turbulent dissipation is consistent with that measured during TH84. The difference in the speed of downward penetration of mixing may be caused by the instantaneous removal of shear instability, or the Kelvin-Helmholtz instabilities, at each time step in the

model. In reality, even though the time scale for a single KH overturn may be the buoyancy period, that instability may induce others for which several periods may be needed for mixing to be completed.

The inclusion of bulk Richardson number mixing distorts turbulent mixing and the diurnal cycle. Bulk Richardson number mixing yields highly intermittent and unrealistically energetic exchanges in the surface layer. This, in turn, introduces spurious multi-day fluctuations and short-term saw-tooth variations in the simulated time series. The model test shows that critical R_b mixing is excessive.

Bibliography

Adamec, D., R. L. Elsberry, R W. Garwood, and R. L. Haney, 1981: An embedded mixed-layer-ocean circulation model. *Dyn. Atmos. Oceans*, **6**, 69-96.

Bryden, H. L. and E. C. Brady, 1985: Diagnostic model of the three- dimensional circulation in the upper equatorial Pacific Ocean. *J. Phys. Oceanogr.*, **15**, 1255–1273.

Bryden, H. L. and E. C. Brady, 1989: Eddy momentum and heat fluxes and their effects on the circulation of the equatorial Pacific Ocean. *J. Mar. Res.*, **47**, 55–79.

Chereskin, T. K., J. N. Moum, P. J. Stabeno, D. R. Caldwell, C. A. Paulson, L. A. Regier and D. Halpern, 1986: Fine-scale variability at 140°W in the equatorial Pacific. *J. Geophys. Res.*, **91**, 12,887–12,897.

Davis, R. E., R. de Szoeke and P. Niiler, 1981. Variability in the upper ocean during MILE. Part II: Modeling the mixed layer response. *Deep-Sea Res.*, **28A(12)**, 1453–1475.

Deardorff, James W.. 1970. Convective velocity and temperature scales for the unstable planetary boundary layer and for Rayleigh convection. *J. Atmos. Sci.*, **27**, 1211–1213.

Deardorff, J. W., G. E. Willis and D. K. Lilly, 1969. Laboratory investigation of non-steady penetrative convection. *J. Fluid Mech.*, **35**, 7–31.

Denman, K. L., 1973. A time-dependent model of the upper ocean. *J. Phys. Oceanogr.*, **3**, 173–184.

Denman, K. L., and M. Miyake, 1973. Upper layer modification at ocean station Papa: observations and simulation. *J. Phys. Oceanogr.*, **3**, 185–196.

Dillon, T. M., J. N. Moum, T. K. Chereskin and D. R. Caldwell, 1989: Zonal momentum balances at the equator. *J. Phys. Oceanogr.*, **19**, 561–570.

Ellison, T. H., and J. S. Turner, 1959: Turbulent entrainment in stratified flows. *J. Fluid Mech.*, **6**, 423–448.

Enfield, D. B., 1986: Zonal and seasonal variations of the near-surface heat balance of the equatorial Pacific Ocean. *J. Phys. Oceanogr.*, **16**, 1038–1054.

Esbensen, S. K. and Y. Kushnir, 1981: The heat budget of the global ocean: An atlas based on estimates from surface marine observations. *Rep.*, **29**, Climate Res. Inst., Oregon State Univ., Corvallis, 1981.

Gregg, M. C., H. Peters, J. C. Wesson, N. S. Oakey, and T.J. Shay, 1985: Intensive measurements of turbulence and shear in the equatorial undercurrent. *Nature*, **318**, 140–144.

Halpern, D., H. P. Freitag, 1987: Vertical motion in the upper ocean of the equatorial Eastern Pacific. *Oceanologica Acta*, **1987**. Proceedings International Symposium on Equatorial Vertical Motion, Paris, 6–10 May 1985, 19–26.

Halpern, D., R. A. Knox, D. S. Luther and S. G. Philander, 1989: Estimates of equatorial upwelling between 140° and 110°W during 1984. *J. Geophys. Res.*, **94**, 8018–8020.

Halpern, D. and R. H. Weisberg, 1989: Upper ocean thermal and flow fields at 0°, 28°W (Atlantic) and 0°, 140°W (Pacific) during 1983–1985. *Deep-Sea Res.*, **36**, 407–418.

Hansen, D. V. and C. A. Paul, 1984: Genesis and effects of long waves in the equatorial Pacific. *J. Geophys. Res.*, **89**, 10431–10440.

Hansen, D. V. and C. A. Paul, 1987: Vertical motion in the eastern equatorial Pacific inferred from drifting buoys. *Oceanologica Acta*, **1987**. Proceedings International Symposium on Equatorial Vertical Motion, Paris, 6–10 May 1985. 19–26.

Hanson, R. J. and K. H. Haskell, 1982: Two algorithms for the linearly constrained least squares problem. *ACM Trans. on Math. Software*, **Sept.**, 1982.

Haskell, K. H. and R. J. Hanson, 1981: An algorithm for linear least squares problems with equality and nonnegativity constraints. *Math. Prog.*, **21**, 98–118.

Hebert, D., J. N. Moum, C. A. Paulson and D. R. Caldwell, 1991: The role of the turbulent stress divergence in the equatorial Pacific zonal momentum balance. *J. Geophys. Res.*, **96**, 7127–7136.

Hellerman, S. and M. Rosenstein, 1983: Normal monthly wind stress over the world ocean with error estimates. *J. Phys. Oceanogr.*, **13**, 1093–1104.

Jerlov, N. G., 1968: Optical Oceanography. *Elsevier Press*, **194pp.**, 1968.

Kantha, L. H., O. M. Phillips, and R. S. Azad, 1977: On the turbulent entrainment at a stable density interface. *J. Fluid Mech.*, **79**, 753–768.

Kato, H., and O. M. Phillips, 1969: On the penetration of a turbulent layer into stratified fluid. *J. Fluid Mech.*, **37**, 643–655.

Knox, R. A. and D. Halpern, 1982: Long-range Kelvin wave propagation of transport variations in Pacific Ocean equatorial currents. *J. Mar. Res.*, **40**(Suppl.), 329–339.

Kraus, E. B., and J. S. Turner, 1967: A one-dimensional model of the seasonal thermocline. II. The general theory and its consequences. *Tellus*, **19**, 98–106.

Lawson and Hanson, 1974: Solving least-square problems. *Printice Hall*, **Chap. 23**, 158–173.

Levitus, S., 1982: Climatological atlas of the world ocean. *NOVA Prof. Pap.*, **13**, 173pp.. 1982.

Luan, S., C. A. Paulson and P. T. Strub, 1993a: Long-Term Budgets of Momentum and Heat in the Upper Equatorial Pacific. *To be submitted*, , 0000–0000.

Luan, S., C. A. Paulson and P. T. Strub, 1993b: A Critical-R_i Model of Turbulent Mixing Applied to the the Upper Equatorial Pacific. *To be submitted*, , 0000–0000.

Luan, S., C. A. Paulson and P. T. Strub, 1993c: Models of the Diurnal Cycle of Mixing in the the Upper Equatorial Pacific. *To be submitted*, , 0000–0000.

Mangum, L. J. and S. P. Hayes, 1984: The vertical structure of the zonal pressure gradient in the eastern equatorial Pacific, *J. Geophys. Res.*, **89**, 10,441–10449.

Mellor, G. L. and T. Yamada, 1982: Development of a turbulence closure model for geophysical fluid problems. *Rev. Geophys. Space Phys.*, **20**, 851–875.

Miles, J. W. and L. N. Howard, 1964: Note on a heterogeneous shear flow. *J. Fluid Mech.*, **20**, 331–336.

Moum, J. N., and D. R. Caldwell, 1985: Local influences on shear-flow turbulence in the equatorial ocean. *Science*, **230**, 315–316.

Moum, J. N., D. R. Caldwell, and C. A. Paulson, 1989: Mixing in the equatorial surface layer and thermocline. *J. Geophys. Res.*, **94**, 2005–2021.

Munk, W. H., 1966: Abyssal recipes. *Deep-Sea Res.*, **13**, 707–730.

Niiler, P. P., and E. B. Kraus, 1977. One-dimensional models. *Modelling and Prediction of the Upper Layers of the Ocean*, E. B. Kraus, Ed., Pergamon Press, **285pp.**, 1977.

Osborn, T. R., 1980: Estimate of the local rate of vertical diffusion from dissipation measurements. *J. Phys. Oceanogr.*, **10**, 83–89.

Osborn, T. R. and C. S. Cox, 1972: Oceanic fine structure. *Geophys. Fluid Dyn.*, **3**, 321–345.

Pacanowski, R. C. and S. G. H. Philander, 1981: Parameterization of vertical mixing in numerical models of tropical oceans. *J. Phys. Oceanogr.*, **11**, 1443–1451.

Pares-Sierra, A. F., M. Inoue, and J. J. O'Brien, 1985: Estimates of oceanic horizontal heat transport in the tropical Pacific. *J. Geophys. Res.*, **90**, 3293–3303.

Paulson, C. A. and J. J. Simpson, 1977: Irradiance measurements in the upper ocean. *J. Phys. Oceanogr.*, **7**, 952–956.

Peters, H, M. C. Gregg, and J. M. Toole, 1988: On the parameterization of equatorial turbulence. *J. Geophys. Res.*, **93**, 1199–1218.

Philander, S. G. H. and R. C. Pacanowski, 1986a: A model of the seasonal cycle in the tropical Atlantic Ocean. *J. Geophys. Res.*, **91**, 14192–14206.

Philander, S. G. H., and R. C. Pacanowski, 1986b: The mass and heat budgets in a model of the tropical Atlantic. *J. Geophys. Res.*, **91**, 14212–14220.

Philander, S. G. H., W. Hurlin and R. C. Pacanowski, 1986: Properties of long equatorial Rossby waves in models of the seasonal cycle in the tropical Atlantic and Pacific Oceans. *J. Geophys. Res.*, **91**, 14207–14211.

Philander, S. G. H., W. Hurlin and A. D. Seigel, 1987: A model of the seasonal cycle in the tropical Pacific Ocean. *J. Phys. Oceanogr.*, **17**, 1986–2002.

Phillips, O. M., 1977. Entrainment. *Modelling and Prediction of the Upper Layers of the Ocean*, E. B. Kraus, Ed., Pergamon Press, **285pp.**, 1977.

Pollard, R. T., T. B. Rhines, and R. O. R. Y. Thompson, 1973: The deepening of the wind-mixed layer. *Geophys. Fluid Dyn.*, **4**, 381–404.

Price, J. F., 1977: Observation and simulation of storm-driven mixed-layer deepening. *Ph.D. dissertation*, University of Miami, Coral Gables, **192pp.**, 1977.

Price, J. F., C. N. K. Mooers, and J. C. Van Leer, 1978: Observation and simulation of storm-induced mixed-layer deepening. *J. Phys. Oceanogr.*, **8**, 582–599.

Price, J. F., R. A. Weller and R. Pinkel, 1986: Diurnal cycling: observations and models of the upper ocean response to diurnal heating, cooling, and wind mixing. *J. Geophys. Res.*, **91**, 8411–8427.

Richtmyer, R. D., and K. W. Morton, 1967: Difference methods for initial-value problems. *Interscience Publishers*, **405pp.**, 1967.

Rohr, J. and C. Van Atta, 1987: Mixing efficiency in stably stratified growing turbulence. *J. Geophys. Res.*, **92**, 5481–5488.

Schudlich, R. R., and J. F. Price, 1992. Diurnal cycles of current, temperature, and turbulent dissipation in a model of the equatorial upper ocean. *J. Geophys. Res.*, **97**, 5409–5422.

Shay, T. J., and M. C. Gregg, 1986: Convectively driven turbulent mixing in the upper ocean. *J. Phys. Oceanogr.*, **16**, 1777–1798.

Stull, R. B., 1991. An introduction to boundary layer meteorology. *Kluwer Academic Publishers*, **666pp.**, 1991.

Thompson, R. O. R. Y., 1976: Climatological numerical models of the surface mixed layer of the ocean. *J. Phys. Oceanogr.*, **6**, 496–503.

Thompson, R. O. R. Y., 1977: Reply. *J. Phys. Oceanogr.*, **7**, 470–471.

Thompson, R. O. R. Y., 1980: Efficiency of conversion of kinetic energy to potential energy by a breaking internal gravity wave. *J. Geophys. Res.*, **85**, 6631–6635.

Toole, J. M., H. Peters, and M. C. Gregg, 1987: Upper ocean shear and density variability at the equator during Tropic Heat. *J. Phys. Oceanogr.*, **17**, 1397–1406.

Wacongne, S., 1989: Dynamical regimes of a fully nonlinear stratified model of the Atlantic equatorial undercurrent. *J. Geophys. Res.*, **94**, 4801–4815.

Wacongne, S., 1990: On the difference in strength between Atlantic and Pacific undercurrents. *J. Phys. Oceanogr.*, **20**, 792–799.

Weare, B. C., P. T. Strub and M. D. Samuel, 1981: Annual mean surface heat fluxes in the tropical Pacific Ocean. *J. Phys. Oceanogr.*, **11**, 705–717.

Wijesekera, H. W., and T. M. Dillon, 1991: Internal waves and mixing in the upper equatorial Pacific Ocean. *J. Geophys. Res.*, **96**, 7115–7125.

Wyrtki, K., 1965: The average annual heat balance of the North Pacific Ocean and its relation to ocean circulation. *J. Geophys. Res.*, **70**, 4547–4559.

Wyrtki, K., 1981: An estimate of equatorial upwelling in the Pacific. *J. Phys. Oceanogr.*, **11**, 1205–1214.

Wyrtki, K. and B. Kilonsky, 1984: Mean water current structure during the Hawaii-to-Tahiti Shuttle Experiment. *J. Phys. Oceanogr.*, **14**, 242–254.

Wyrtki, K. and G. Meyers, 1976: The trade wind field over the Pacific Ocean. *J. Applied Meteoro.*, **15**, 698–704.

Appendices

Appendix A

The Least Squares Problem for Inverse Analysis

To express Eqs. (2.7), (2.8), and (2.9) in matrix form, we define the following depth arrays

$$\hat{z}_w = \left[\frac{z}{h_b} \quad (\frac{z}{h_b})^2 \quad (\frac{z}{h_b})^3 \right] \tag{A.1}$$

$$\hat{z} = \left[1 \quad \frac{z}{h_b} \quad (\frac{z}{h_b})^2 \quad (\frac{z}{h_b})^3 \quad (\frac{z}{h_b})^4 \right] \tag{A.2}$$

$$\frac{d\hat{z}}{dz} = \left[0 \quad 1 \quad 2\frac{z}{h_b} \quad 3(\frac{z}{h_b})^2 \quad 4(\frac{z}{h_b})^3 \right] \frac{1}{h_b} \tag{A.3}$$

and vectors of the unknown polynomial coefficients

$$\hat{w} = \left[w_1 \quad w_2 \quad w_3 \right]^T \tag{A.4}$$

$$\hat{f} = \left[f_0 \quad f_1 \quad f_2 \quad f_3 \quad f_4 \right]^T \tag{A.5}$$

$$\hat{g} = \left[g_0 \quad g_1 \quad g_2 \quad g_3 \quad g_4 \right]^T \tag{A.6}$$

Hence, Eqs. (2.7), (2.8), and ((2.9) become

$$\overline{W} = \hat{z}_w \cdot \hat{w} \tag{A.7}$$

$$\overline{F}_m = \rho_o \hat{z} \cdot \hat{f} \tag{A.8}$$

$$\overline{F}_h = \rho_o C_p \hat{z} \cdot \hat{g} \tag{A.9}$$

and

$$\frac{\partial \overline{F}_m}{\partial z} = \rho_\circ \frac{d\tilde{z}}{dz} \cdot \tilde{f} \tag{A.10}$$

$$\frac{\partial \overline{F}_h}{\partial z} = \rho_\circ C_p \frac{d\tilde{z}}{dz} \cdot \tilde{f} \tag{A.11}$$

The equations of zonal momentum and heat balances, (2.10) and (2.11), can be written

$$\left(\frac{\partial \overline{U}}{\partial z}\tilde{z}_w\right)_i \cdot \tilde{w} + \left(\frac{d\tilde{z}}{dz}\right)_i \cdot \tilde{f} = M_i + R_{mi} \tag{A.12}$$

$$\left(\frac{\partial \overline{T}}{\partial z}\tilde{z}_w\right)_i \cdot \tilde{w} + \left(\frac{d\tilde{z}}{dz}\right)_i \cdot \tilde{g} = H_i + R_{hi} \tag{A.13}$$

where subscript "$_i$" indicates evaluations at the 10 depth levels, $z = z_i = 0$, -10, -20, -30, -50, -75, -100, -125, -150, -200, for $i = 1, 2, \cdots, 10$, and

$$M_i = -\left(\overline{U}\frac{\partial \overline{U}}{\partial x} - \frac{\partial \overline{V'U'}}{\partial y} - \frac{1}{\rho_\circ}\frac{\partial \overline{P}}{\partial x}\right)_i \tag{A.14}$$

$$H_i = -\left(\overline{U}\frac{\partial \overline{T}}{\partial x} + \frac{\partial \overline{V'T'}}{\partial y}\right)_i \tag{A.15}$$

The boundary conditions and other constraints on turbulent fluxes are divided by depth scale h_b so that the corresponding equations have same dimensions as the momentum or heat equations (2.10) and (2.11), respectively. The boundary conditions and constraints (2.12) through (2.20) are

$$\tilde{z} \cdot \tilde{f} h_b^{-1} = -\frac{\tau_x}{\rho_\circ h_b} + R_\tau \tag{A.16}$$

$$\tilde{z} \cdot \tilde{g} h_b^{-1} = \frac{Q_{net}}{\rho_\circ C_p h_b} + R_Q \tag{A.17}$$

at $z = 0$, and

$$\tilde{z} \cdot \tilde{f} h_b^{-1} = 0 \tag{A.18}$$

at $z = -h_{core}$, and

$$\frac{d\tilde{z}}{dz} \cdot \tilde{f} = 0 \tag{A.19}$$

$$\frac{d\tilde{z}}{dz} \cdot \tilde{g} = 0 \tag{A.20}$$

$$\tilde{z} \cdot \tilde{f} h_b^{-1} = -\frac{K_b}{h_b} \frac{\partial \overline{U}}{\partial z} \tag{A.21}$$

$$\tilde{z} \cdot \tilde{g} h_b^{-1} = -\frac{K_b}{h_b} \frac{\partial \overline{T}}{\partial z} \tag{A.22}$$

at $z = -h_b$, and

$$-\text{sign}(\frac{\partial \overline{U}}{\partial z}) \tilde{z} \cdot \tilde{f} h_b^{-1} \geq \frac{K_b}{h_b} \left| \frac{\partial \overline{U}}{\partial z} \right| \tag{A.23}$$

$$-\tilde{z} \cdot \tilde{g} h_b^{-1} \geq \frac{K_b}{h_b} \frac{\partial \overline{T}}{\partial z} \tag{A.24}$$

at $z = z_j = j\Delta z$, for $j = 0, 1, 2, \cdots, 40$, where $\Delta z = 5\,\text{m}$. The sign function sign(x) = 1 if $x \geq 0$, and -1 if $x < 0$.

We construct the linear system for $\tilde{w}$, $\tilde{f}$, and $\tilde{g}$ as

$$\tilde{A} \cdot \tilde{x} - \tilde{B} = \tilde{R} \tag{A.25}$$

$$\tilde{E} \cdot \tilde{x} - \tilde{F} = 0 \tag{A.26}$$

$$\tilde{G} \cdot \tilde{x} - \tilde{H} \geq 0 \tag{A.27}$$

where the vector of unknowns

$$\tilde{x} = \begin{pmatrix} \tilde{w} \\ \tilde{f} \\ \tilde{g} \end{pmatrix} \tag{A.28}$$

the first set includes the 22 equations of (A.12), (A.13), (A.16), and (A.17)

$$\check{A} = \begin{pmatrix} \left[\frac{\partial \overline{U}}{\partial z} i\hat{w}\right]_i & \left[\frac{d\hat{z}}{dz}\right]_i & \hat{0} \\ \left[\frac{\partial \overline{T}}{\partial z} i\hat{w}\right]_i & \left[\frac{d\hat{z}}{dz}\right]_i & \hat{0} \\ \hat{0} & h_b^{-1}\hat{z}\,|_{z=0} & \hat{0} \\ \hat{0} & \hat{0} & h_b^{-1}\hat{z}\,|_{z=0} \end{pmatrix} \tag{A.29}$$

$$\check{B} = \begin{pmatrix} M_i \\ H_i \\ -\frac{\tau_x}{\rho_o h_b} \\ \frac{Q_{net}}{\rho_o C_p h_b} \end{pmatrix} \tag{A.30}$$

and the vector of residuals

$$\check{R} = \begin{pmatrix} R_{mi} \\ R_{hi} \\ R_\tau \\ R_Q \end{pmatrix} \tag{A.31}$$

the second set includes the 5 equations of (A.18) through (A.22)

$$\check{E} = \begin{pmatrix} \hat{0} & h_b^{-1}\hat{z}\,|_{z=-h_{core}} & \hat{0} \\ \hat{0} & \frac{d\hat{z}}{dz}\,|_{z=-h_b} & \hat{0} \\ \hat{0} & \hat{0} & \frac{d\hat{z}}{dz}\,|_{z=-h_b} \\ \hat{0} & h_b^{-1}\hat{z}\,|_{z=-h_b} & \hat{0} \\ \hat{0} & \hat{0} & h_b^{-1}\hat{z}\,\big|_{z=h_b} \end{pmatrix} \tag{A.32}$$

$$\hat{F} = \begin{pmatrix} 0 \\ 0 \\ 0 \\ -\frac{K_b}{h_b}\frac{\partial \overline{U}}{\partial z}\Big|_{z=-h_b} \\ -\frac{K_b}{h_b}\frac{\partial \overline{T}}{\partial z}\Big|_{z=-h_b} \end{pmatrix} \tag{A.33}$$

and, the third set includes the 82 inequalities of (A.23) and (A.24)

$$\hat{G} = \begin{pmatrix} \hat{0} & -h_b^{-1}\left[\text{sign}(\frac{\partial \overline{U}}{\partial z})\hat{z}\right]_j & \hat{0} \\ \hat{0} & \hat{0} & -h_b^{-1}\left[\hat{z}\right]_j \end{pmatrix} \tag{A.34}$$

$$\hat{H} = \begin{pmatrix} \frac{K_b}{h_b}\left|\frac{\partial \overline{U}}{\partial z}\right|_j \\ \frac{K_b}{h_b}\left[\frac{\partial \overline{T}}{\partial z}\right]_j \end{pmatrix} \tag{A.35}$$

We multiply all the rows of momentum equations in (A.25), (A.26), and (A.27) with a weight, $\lambda > 0$, to obtain solutions that give optimal improvement in the residuals. The weighted least squares problem, denoted by superscript ($'$), becomes

$$\hat{A}' \cdot \hat{x} - \hat{B}' = \hat{R}' \tag{A.36}$$

$$\hat{E}' \cdot \hat{x} - \hat{F}' = 0 \tag{A.37}$$

$$\hat{G}' \cdot \hat{x} - \hat{H}' = 0 \tag{A.38}$$

where, in particular,

$$\hat{R}' = \begin{pmatrix} \lambda R_{mi} \\ R_{hi} \\ \lambda R_{\tau} \\ R_Q \end{pmatrix} \tag{A.39}$$

We apply the inverse analysis to the linear system constructed above. The technique employed to solve the linear least squares problem with both equality and inequality constraints is due to Lawson and Hanson (1974). The numerical algorithms developed by Haskell and Hanson (1981) and Hanson and Haskell (1982) are used.

The method minimizes the weighted sum of residuals squared, $\lambda^2 \sum_{i=1}^{10} R_{mi}^2 + \sum_{i=1}^{10} R_{hi}^2 + \lambda^2 R_\tau^2 + R_Q^2$. in a least squares sense, and yields solutions for the unknown coefficients, w_1, w_2, w_3, f_i and g_i, and hence $\overline{W}(\mathrm{z})$, $\overline{F}_m(\mathrm{z})$ and $\overline{F}_h(\mathrm{z})$.

Appendix B

Sensitivity Tests of Inverse Solutions

In this section the solutions obtained by use of the inverse analysis are tested for their sensitivity to variations in specified parameters and observations. The solutions obtained in Section 2.3 are called the standard case. For the standard case $\overline{W}$ is represented by a cubic function of depth, zero at the surface, $\overline{F}_m$ and $\overline{F}_h$ by fourth order polynomials, background diffusivity $K_b = 1 \times 10^{-5}\,\mathrm{m^2 s^{-1}}$, and the weight applied to the momentum equations $\lambda = 4$. The inverse analysis minimizes the weighted sum of residuals squared, $\lambda^2 \sum_{i=1}^{10} R_m(z_i)^2 + \sum_{i=1}^{10} R_h(z_i)^2 + \lambda^2 R_\tau^2 + R_Q^2$, where z_i = 0, -10, -20, -30, -50, -75, -100, -125, -150, and -200 m, for $i = 1, 2, \cdots, 10$. We first test the sensitivity to different weights including different values of λ, second to different degrees of polynomial representations of vertical velocity and turbulent fluxes, third to different values for the background diffusivity, and fourth and last to variations of the observed forcing and surface boundary conditions.

To qualitatively describe the sensitivity, the rms values of the residuals, $R_m(z)$ and $R_h(z)$. are defined as

$$R_m^{rms} = \left[\frac{1}{h_b}\int_{-h_b}^{0} R_m^2(z)\,dz\right]^{\frac{1}{2}} \tag{B.1}$$

$$R_h^{rms} = \left[\frac{1}{h_b}\int_{-h_b}^{0} R_h^2(z)\,dz\right]^{\frac{1}{2}} \tag{B.2}$$

where $h_b = 200\,\mathrm{m}$. When the residuals are included in the turbulent transport terms, the rms values of $\overline{F}_m$, $\overline{F}_h$, $\overline{K}_m$ and $\overline{K}_h$ are computed as

$$F_m^{rms} = \left[\frac{1}{h_b}\int_{-h_b}^{0}\left(\overline{F}_m - \rho_\circ\int_{-h_{core}}^{z} R_m(\zeta)\,d\zeta\right)^2 dz\right]^{\frac{1}{2}} \tag{B.3}$$

$$F_h^{rms} = \left[\frac{1}{h_b}\int_{-h_b}^{0}\left(\overline{F}_h + \rho_\circ C_p K_b\frac{\partial\overline{T}(-h_b)}{\partial z} - \rho_\circ C_p\int_{-h_{core}}^{z} R_h(\zeta)\,d\zeta\right)^2 dz\right]^{\frac{1}{2}} \tag{B.4}$$

$$K_m^{rms} = \left[\frac{1}{h_b}\int_{-h_b}^{0}\left(\frac{\overline{F}_m}{\rho_\circ} - \int_{-h_{core}}^{z} R_m(\zeta)\,d\zeta\right)^2\left(\frac{\partial\overline{U}}{\partial z}\right)^{-2} dz\right]^{\frac{1}{2}} \tag{B.5}$$

$$K_h^{rms} = \left[\frac{1}{h_b}\int_{-h_b}^{0}\left(\frac{\overline{F}_h}{\rho_\circ C_p} + K_b\frac{\partial\overline{T}(-h_b)}{\partial z} - \int_{-h_{core}}^{z} R_h(\zeta)\,d\zeta\right)^2\left(\frac{\partial\overline{T}}{\partial z}\right)^{-2} dz\right]^{\frac{1}{2}} \tag{B.6}$$

where $h_{core} = 125\,\mathrm{m}$. The rms values defined by equations B.3 to B.4 are the rms differences between solid and dashed lines in Fig. 7 for $\overline{F}_m$ and $\overline{F}_h$. The integration relative to the depth of the core is to avoid division by zero.

The standard-case rms values are denoted by the subscript "$_\circ$". The standard-rms values are: $R_{\circ m}^{rms} = 0.5\times10^{-7}\,\mathrm{m\,s^{-2}}$, $R_{\circ h}^{rms} = 0.2\times10^{-6}\,^\circ\mathrm{C\,s^{-1}}$, $F_{\circ m}^{rms} = 0.002\,\mathrm{N\,m^{-2}}$, $F_{\circ h}^{rms} = 5\,\mathrm{W\,m^{-2}}$, $K_m^{rms} = 1.9\times10^{-4}\,\mathrm{m^2\,s^{-1}}$, and $K_h^{rms} = 0.5\times10^{-4}\,\mathrm{m^2\,s^{-1}}$.

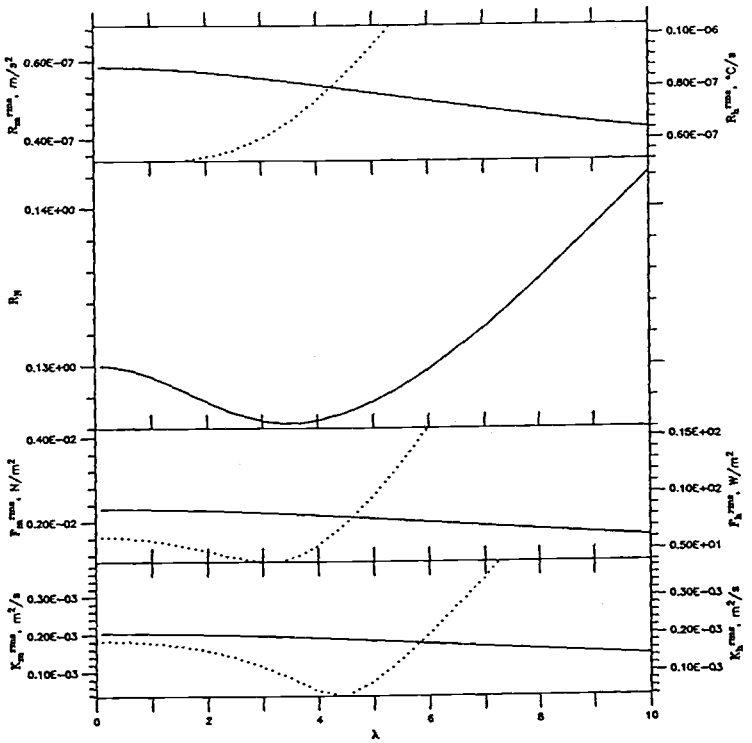

Figure 30. Root-mean-square (rms) values of residuals for momentum, R_m (solid), heat, R_h (dashed), normalized sum, R_n, turbulent fluxes, $\overline{F}_m$ (solid) and $\overline{F}_h$ (dashed), and turbulent diffusivities, $\overline{K}_m$ (solid) and $\overline{K}_h$ (dashed), all plotted as a function of the weighting parameter λ, a factor multiplied the momentum equation as part of the inverse analysis. The normalized sum, $R_n = R_m^{rms}/(5 \times 10^{-7}\,\mathrm{m\,s^{-2}}) + R_h^{rms}/(4 \times 10^{-6}\,^{\circ}\mathrm{C\,s^{-1}})$, where the normalization factors are the maxima of the terms in the momentum and heat balances (Figs. 5 and 6). The plot for R_m^{rms} and R_h^{rms} is scaled so that the bottoms represent their minimum values (at $\lambda = 0.01$ for R_h^{rms}, at 100 for R_m^{rms}), and the tops represent two times their minima, respectively. The plot for F_m^{rms} and F_h^{rms} is similarly scaled except that the tops are 4 times their minima, respectively.

Because the momentum and heat balance equations have different dimensions and terms of different magnitude, the momentum equation and constraints are multiplied by the weight λ (see Section 2.3) to optimize the reduction of residuals. The rms values of the residuals do not necessarily reach a minimum for the same value of the weight lambda. Variation of the rms values, and the sum of normalized rms values of momentum and heat, $R_n = R_m^{rms}/(5 \times 10^{-7}\,\mathrm{m\,s^{-2}}) + \mathrm{R_h^{rms}}/(4 \times 10^{-6},^{\circ}\mathrm{C\,s^{-1}})$, as a function of λ, are shown in Fig. 30. The values of R_m^{rms}, F_m^{rms}, and K_m^{rms} are much less sensitive to changes in λ than those of R_h^{rms}, F_h^{rms}, and K_h^{rms}. In particular, for $\lambda > 2$, increasing λ yields very gradual reduction of the momentum residuals, but causes abrupt increase of the heat residuals. The solutions for vertical velocity, turbulent fluxes and turbulent diffusivities are shown in the top panel of Fig. 31, and numerical values are given in Table 3, for $\lambda = 1$, 4, and 8. The results for $\lambda = 1$ and 4 are nearly indistinguishable, but there are significant effects on $\overline{K}_m$ and $\overline{K}_h$ for $\lambda = 8$. The combined normalized rms value, R_n, is the sum of the ratios of the rms values of the momentum and heat residuals to the estimated maximum magnitudes of the leading terms in the balances, $5 \times 10^{-7}\,\mathrm{m\,s^{-2}}$ for momentum, and $4 \times 10^{-6}\,^{\circ}\mathrm{C\,s^{-1}}$ for heat. A minimum in the combined normalized residual R_n determines on optimum choice for λ, which is $\lambda = 3.5$, which we rounded to $\lambda = 4$ for the standard case.

Sensitivity of the inverse solutions to uniform weighting with depth was also tested. The momentum and heat balance equations were evaluated at depths with equal intervals of $\Delta z = 5\,\mathrm{m}$, rather than at the standard case's 10 specified depth levels of 0, -10, -20, -50, -75, -100, -125, -150, -200 m. The effect of uniform-depth weighting is shown by dotted lines in the second

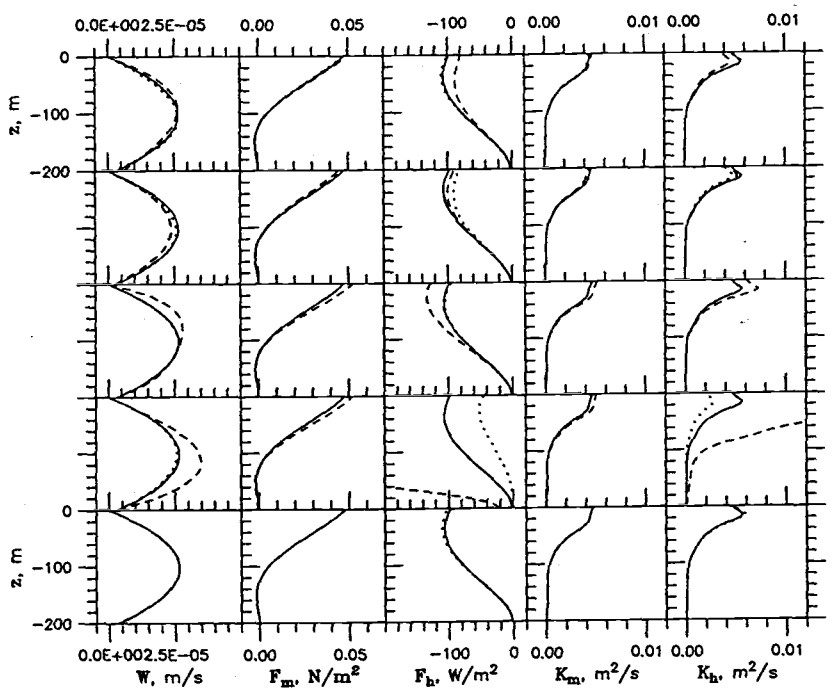

Figure 31. Sensitivity of the inverse solutions for vertical velocity, turbulent fluxes and turbulent diffusivities to: row 1–the weighting parameter $\lambda = 1, 4, 8$; row 2–$\Delta z = 5$, ten specified depths, equal equation weighting; row 3–degree of polynomial representation of $\overline{W}$ is 2, 3, 4; row 4–background diffusivity $K_b = 10^{-6}, 10^{-5}, 10^{-4}\,\mathrm{m^2\,s^{-1}}$; row 5–without surface boundary conditions, with surface boundary conditions. In each of the above, the first case is a dotted line, the second is solid and the third is dashed, *i.e.*, $\lambda = 1$ is dotted, $\lambda = 4$ is solid, *etc.* The solid lines are the standard case.

row of panels in Fig. 31. The resulting vertical velocity maximum is only 3% smaller, and the turbulent heat flux 10 to 20% smaller, than those of the standard-case solutions. The turbulent momentum flux and turbulent diffusivities show little changes. The rms values of the residuals show no significant changes (Table 3). Although the method of evaluation at uniform $\Delta z = 5\,\mathrm{m}$ intervals add more equations to the system, it adds no additional information because the added equations are evaluated by interpolating the observations.

We also tested the effects of weighting every equation of the system equally. Equal-equation weighting is achieved by multiplying each equation by a constant such that the largest of the coefficients for the 13 unknowns (w_1, w_2, w_3, f_i and g_i for $i = 0, 1, \ldots, 4$) for that particular equation is one and the rest are between 1 and -1. The results of this weighting are shown as dashed lines in the second row of panels in Fig. 31. Equal-equation weighting yields a vertical velocity maximum and turbulent fluxes larger than the standard case and those for momentum are changed negligibly (Table 3).

The effect on the inverse solutions of different degrees of polynomial representations for $\overline{F}_m$, $\overline{F}_h$ and $\overline{W}$ was tested. The degrees of the polynomial representations are controlled by two factors. The degrees are required to be sufficiently high to accurately represent the vertical structure in the solutions but are limited by the rank of the linear system. The weighted sum of residuals squared $[\lambda^2 \sum_{i=1}^{10} R_m(z_i)^2 + \sum_{i=1}^{10} R_h(z_i)^2 + \lambda^2 R_\tau^2 + R_Q^2]$, the ratio of the number of unknowns to the rank of the linear system, the maximum vertical velocity, and the values of R_m^{rms}, R_h^{rms}, F_m^{rms}, F_h^{rms}, K_m^{rms}, K_h^{rms}, are plotted in Fig. 32 as functions of the degree of polynomials representing $\overline{W}$,

$\overline{F}_m$, and $\overline{F}_h$. As the polynomial degree for $\overline{F}_m$ and $\overline{F}_h$ increases from 3 to 7, the linear system has more degrees of freedom to reduce the weighted sum of residuals squared. However, such an increase in the degrees of freedom causes the number of unknowns to exceed the rank of the system, and hence makes the system under-determined; it also causes excessive high wavenumber oscillations which appear as increases in the rms residuals for the heat balance, $\overline{F}_m$ and $\overline{F}_h$.

Based on the results shown in Fig. 32, we chose for the standard case a cubic polynomial for representation of $\overline{W}$ and quartic polynomials for representation of $\overline{F}_m$ and $\overline{F}_h$. The weighted sum of residuals squared (top panel) decreases very slowly for higher degree polynomials and there is merit in choosing a low degree to make the problem over- rather than under-determined (panel 2, Fig. 32).

Response of the inverse solutions to variation of the background diffusivity, K_b, was determined for the range of K_b an order of magnitude smaller and larger than the standard-case value of $1 \times 10^{-5}\,\mathrm{m^2\,s^{-1}}$. The rms residuals are plotted *vs.* K_b in Fig. 33. There is negligible variation in the residuals for $K_b < 2 \times 10^{-5}\,\mathrm{m^2\,s^{-1}}$. The increase in the residuals for $K_b > 2 \times 10^{-5}\,\mathrm{m^2\,s^{-1}}$ suggests, consistent with observations (Peters *et al.*, 1988; Dillon *et al.*, 1989; Moum *et al.*, 1989), that K_b should be less than this value. The response of vertical velocity and turbulent fluxes and diffusivities to changing the standard value of K_b by $\pm$ an order of magnitude is shown in the fourth row of panels of Fig. 31. There is negligible effect of the variation of K_b by $\pm$ an order of magnitude on $\overline{F}_m$ and $\overline{K}_m$. There are large, unrealistic anomalies

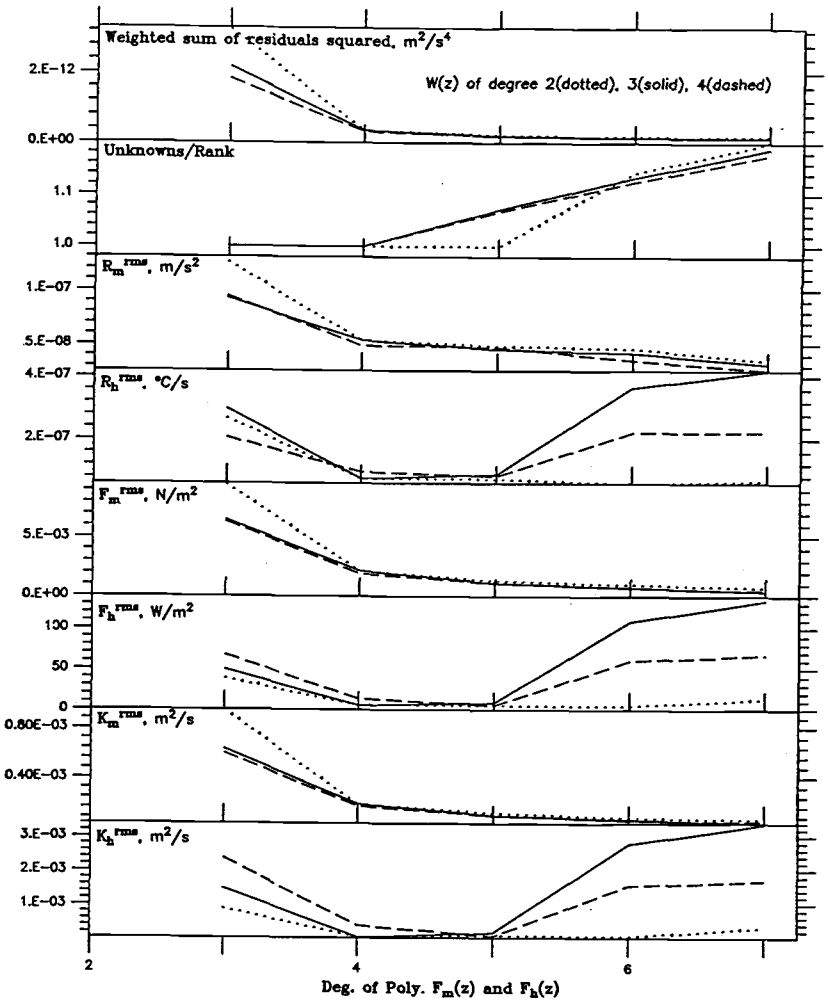

Figure 32. The weighted sum of residuals squared, $\lambda^2 \sum_{i=1}^{10} R_m(z_i)^2 + \sum_{i=1}^{10} R_h(z_i)^2 + \lambda^2 R_\tau^2 + R_Q^2$, the ratio of the number of unknowns to the rank of the linear system, and the rms values of residuals R_m, R_h, F_m, F_h, K_m, K_h, as functions of the degree of polynomials representing $\overline{F}_m$ and $\overline{F}_h$ with $\overline{W}$(z) being represented by polynomials of degree one (dotted), three (solid) or four (dashed).

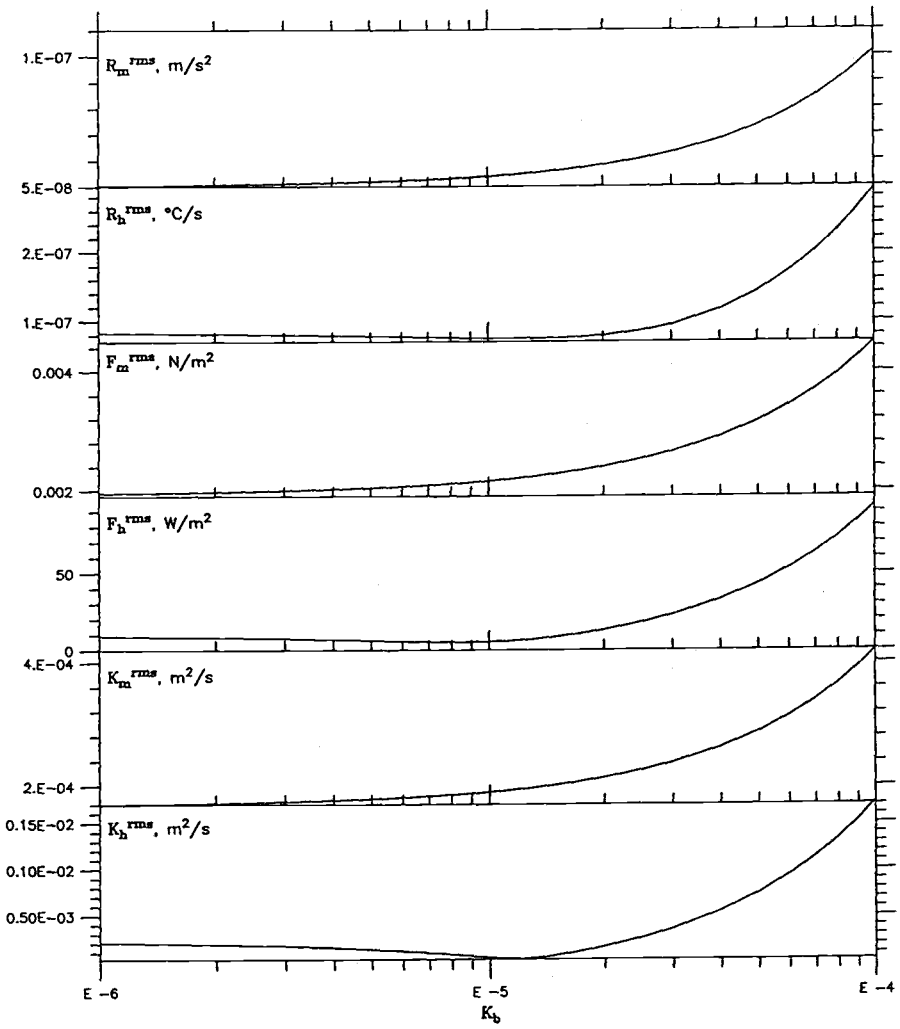

Figure 33. The rms values of the residuals, R_m, R_h, F_m, F_h, K_m and K_h as a function of prescribed background diffusivity K_b.

in $\overline{F}_h$ and $\overline{K}_h$ for $K_b = 1 \times 10^{-4}\,\mathrm{m^2\,s^{-1}}$, consistent with the discussion above that this value is too large. For $K_b = 1 \times 10^{-4}\,\mathrm{m^2 s^{-1}}$, there is negligible effect on $\overline{W}$, but $\overline{F}_h$ and $\overline{K}_h$ are about 50smaller than the standard case. The large effect on $\overline{F}_h$ and $\overline{K}_h$ of varying K_b is because turbulent heat flux is a small term in heat balance between 70 and 200-m depth (Fig. 6). The specification of K_b determines the value of $\overline{F}_h$ and $\overline{K}_h$ at 200 m. The variation of $\overline{F}_h$ and $\overline{K}_h$ with z is very weakly constrained by the heat balance between 70 and 200-m depth, which leads to the large effects of K_b on $\overline{F}_h$ and $\overline{K}_h$. The inverse solutions for $\overline{F}_h$ and $\overline{K}_h$ are uncertain by about $\pm 50\%$ because of the sensitivity of $\overline{F}_h$ and $\overline{K}_h$ on the choice of K_b.

The effect on the inverse solutions of removing the surface flux conditions, (2.12) and (2.13), was tested. The solutions for vertical velocity, turbulent momentum and heat flux and the turbulent diffusivities are negligibly affected as is shown in the bottom panel of Fig. 31. The effect on the rms residuals is also negligible as shown in Table 3. The insensitivity of the inverse solutions to specified surface fluxes of momentum and heat shows that the results, including estimates of surface fluxes, are essentially determined by oceanic conditions.

Sensitivity tests of the inverse solutions to variations in the forcing terms $\partial\overline{U}/\partial x$, $\partial\overline{V'U'}/\partial y$, $-\rho_\circ^{-1}\partial\overline{P}/\partial x$, $\overline{U}$ (and $\partial\overline{U}/\partial z$), $\partial\overline{T}/\partial x$, $\partial\overline{T}/\partial z$, τ_x, and Q_{net} are plotted in Fig. 34. These terms were perturbed by multiplying one at a time by factors of 1.5 (dotted line) and 0.5 (dashed line), respectively. The profiles of vertical velocity, turbulent fluxes and turbulent diffusivities are plotted for each of the perturbations together with the standard case (solid)

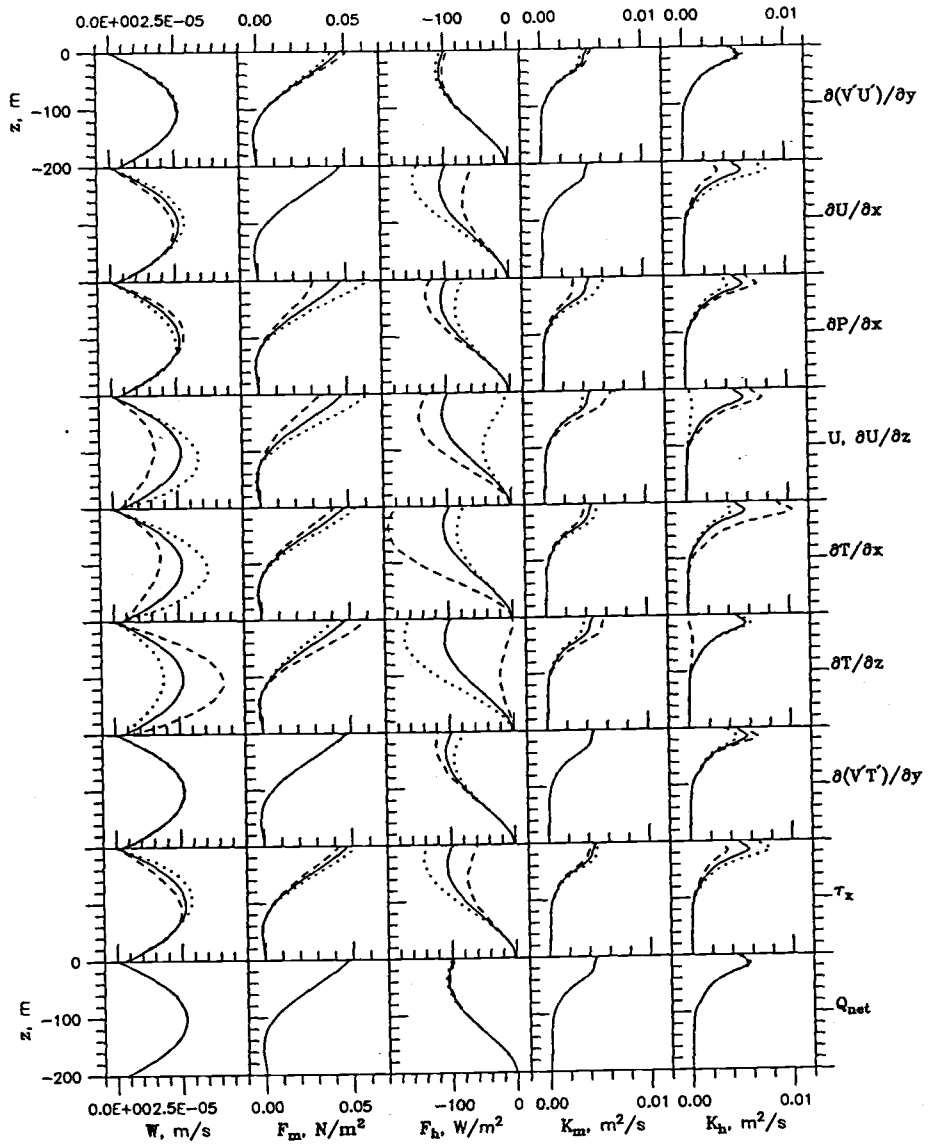

Figure 34. Responses of vertical velocity, turbulent fluxes and diffusivities to 50% increases (dotted) or 50% decreases (dashed) of $\partial\overline{V'U'}/\partial y$, $\partial\overline{U}/\partial x$, $-\rho_o^{-1}\partial\overline{P}/\partial x$, $\overline{U}$ (and $\partial\overline{U}/\partial z$), $\partial\overline{T}/\partial x$, $\partial\overline{T}/\partial z$, $\partial\overline{V'T'}/\partial y$, τ_o^x, and Q_{net}. The solid lines are the standard solutions from Figs. 4, 7, and 8, respectively.

in Fig. 34. Vertical velocity is most sensitive to changes in zonal velocity, and zonal and vertical gradients of temperature. The vertical turbulent flux of zonal momentum, $\overline{F}_m$, is most sensitive to changes in zonal pressure gradient, zonal velocity and vertical temperature gradient. The vertical turbulent flux of heat, $\overline{F}_h$, is sensitive to changes in a variety of variables, the largest of which are vertical temperature gradient, horizontal temperature gradient, zonal velocity and its vertical gradient, and horizontal temperature gradient. Turbulent viscosity, $\overline{K}_m$, is sensitive to the same variables as $\overline{F}_m$. Similarly, the turbulent diffusivity for heat, $\overline{K}_h$, is sensitive to the same variables as $\overline{F}_h$.

It is important to recognize that the sensitivities of the inverse results to various forcing variables (Fig. 34) should not be interpreted as error estimates. All of the forcing variables were perturbed by $\pm 50\%$ and many of the variables are known more accurately. For example, the long-term mean vertical temperature gradient is perhaps known to about 5% accuracy and long-term mean velocity is known to about 20%. The sensitivities can be converted into error estimates by appropriate scaling.

In summary, we have reasonably chosen for the inverse analysis described in Section 2.3 the weighting, the degrees of polynomial representations of the vertical velocity and turbulent fluxes of zonal momentum and heat, and the background diffusivities. The sensitivity tests to $\pm 50\%$ changes in the forcing variables provides the basis for estimating errors in the results of the inverse analysis.

Case	R_m^{rms} (10^{-8} m s^{-2})	R_h^{rms} (10^{-8} °C s^{-1})	F_m^{rms} (10^{-3} N m^{-2})	F_h^{rms} (W m^{-2})	K_m^{rms} (10^{-4} m^2 s^{-1})	K_h^{rms} (10^{-4} m^2 s^{-1})
Standard	5.4	7.5	2.2	5.4	1.9	0.5
$\lambda = 1$	5.8	5.2	2.3	5.8	2.0	1.8
$\lambda = 8$	4.6	17.5	1.8	30.8	1.6	5.2
$\Delta z = 5$ m	5.2	8.7	1.9	7.1	1.7	0.4
Equal eqn weighting	4.6	23.4	1.9	94.2	1.7	25.7
$\overline{W}$, quadratic	5.4	7.4	2.2	5.3	1.9	0.5
$\overline{W}$, quartic	4.8	9.6	1.9	13.6	1.7	3.9
$K_b = 1 \times 10^{-6}$ m^2 s^{-1}	5.0	8.3	2.0	9.2	1.7	2.1
$K_b = 1 \times 10^{-4}$ m^2 s^{-1}	10.2	29.2	4.5	93.9	4.2	17.2
Surface bc's removed	5.4	7.3	2.2	5.6	2.0	0.4

Table 3. Root-mean-square values of the residuals for the momentum balance, the heat balance, the vertical turbulent momentum and heat fluxes and the turbulent diffusivities for momentum and heat. The rms residuals are computed for the standard case and for different weights ($\lambda = 1, 8$, equal equation), uniform vertical grid ($\Delta z = 5$m), quadratic and quartic polynomial representations of vertical velocity, background diffusivity, K_b, an order of magnitude smaller and larger than the standard case, and with surface boundary conditions removed.

Appendix C

Implementaion and Stability Analysis of Simple R_i Model

The implementation of the model computations are summarized in the flow chart shown in Fig. 35. The details of each unit of the chart are described below.

Grid and time step

As shown in Fig. 36, with the total depth $h_b = 200\,\mathrm{m}$ divided up uniformly by the vertical grid spacing of Δz, there are total $J = h_b/\Delta z$ levels. The grids are numbered sequentially from the bottom to the top, j =1, 2, ..., $J-1$, J, with the bottom being the first, and the top the last or Jth. Grid j is centered at $z_j = (j - J - \frac{1}{2})\Delta z$, and bounded by $z_{j-\frac{1}{2}} = (j - J - 1)\Delta z$, and $z_{j+\frac{1}{2}} = (j - J)\Delta z$.

All of the variables of the momentum and heat equations are evaluated or approximated at the center of the grid, except the vertical turbulent fluxes and diffusivities, which are evaluated at the bounds. We use subscript "$_j$" to indicate evaluation at grid j.

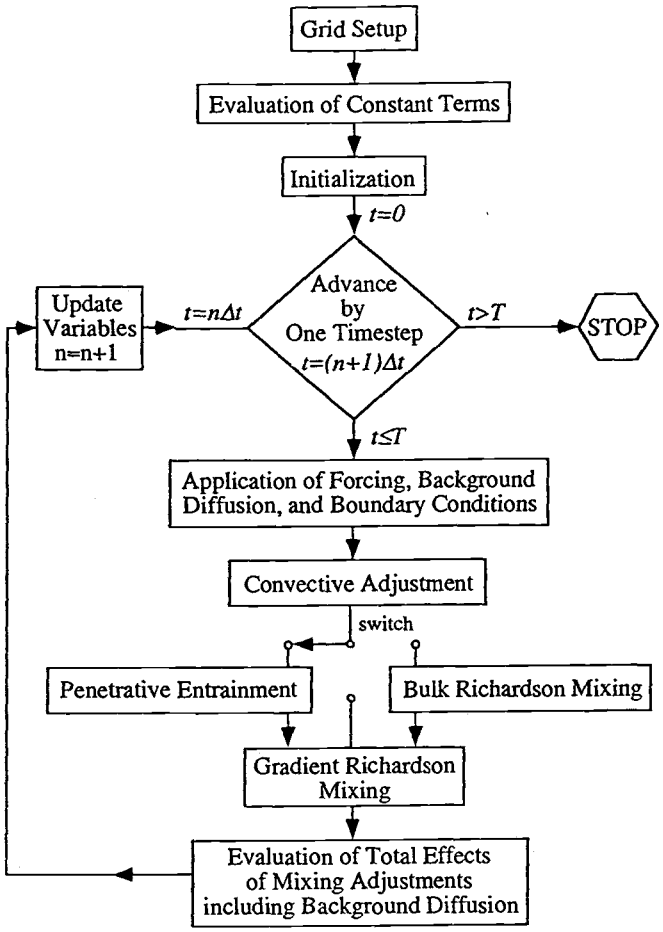

Figure 35. Flow chart of computational implementation of the model.

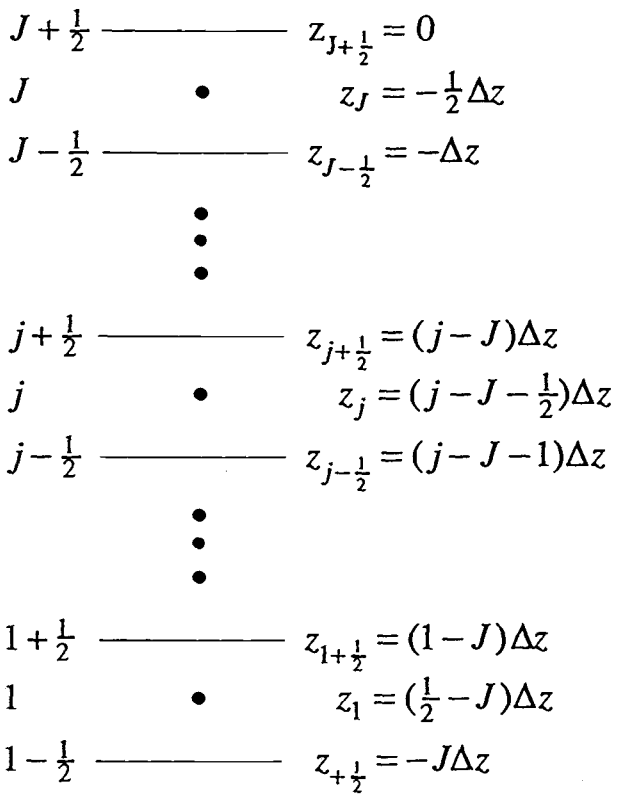

Figure 36. Diagram of vertical grid levels.

We start the model computation from $t = 0$, and then increment the computation with a time step Δt at $t = n\Delta t$ for a specified total period of $T = N\Delta t$. Hence, $n = 0, 1, 2, \ldots, N-1, N$. We use superscript "$n$" to represent evaluation at the end of time step n, $t = n\Delta t$. Thus, superscript "0" indicates initial values.

Constant terms

At the beginning of the computation, all constant forcing terms are evaluated at the center of each grid $j = 1, 2, \ldots, J-1, J$, such as

$$\overline{W}_j = \overline{W}\Big|_{z=z_j} \tag{C.1}$$

$$\left(\frac{1}{\rho_\circ}\frac{\partial \overline{P}}{\partial x}\right)_j = \frac{1}{\rho_\circ}\frac{\partial \overline{P}}{\partial x}\Big|_{z=z_j} \tag{C.2}$$

$$\left(\frac{\partial \overline{U}}{\partial x}\right)_j = \frac{\partial \overline{U}}{\partial x}\Big|_{z=z_j} \tag{C.3}$$

$$\left(\frac{\partial \overline{T}}{\partial x}\right)_j = \frac{\partial \overline{T}}{\partial x}\Big|_{z=z_j} \tag{C.4}$$

$$\left(\frac{\partial \overline{V'U'}}{\partial y}\right)_j = \frac{\partial \overline{V'U'}}{\partial y}\Big|_{z=z_j} \tag{C.5}$$

$$\left(\frac{\partial \overline{V'T'}}{\partial y}\right)_j = \frac{\partial \overline{V'T'}}{\partial y}\Big|_{z=z_j} \tag{C.6}$$

Initialization

Before the computation for first time step $t = \Delta t$, initial values of zonal velocity and temperature are assigned as following, unless specified differently,

$$\hat{U}_j^0 = \hat{U}(z_j, t=0) = \overline{U}(z_j) \tag{C.7}$$

$$\hat{T}_j^0 = \hat{T}(z_j, t=0) = \overline{U}(z_j) \tag{C.8}$$

Application of forcing, background diffusion and boundary conditions

At the beginning of a new time step $n+1$, we first apply the boundary and interior forcing terms including the the prescribed background diffusion of constant diffusivity K_b. The tildes over the any time-dependent variables such as zonal velocity and temperature represent their intermediate values within a time step; and the hats represent the variables' final values (after all mixing adjustments) at the end of a time step.

Surface boundary conditions on turbulent fluxes, together with other forcing terms involved, are applied to the top grid, $j = J$. That is, at $z_j = -\frac{1}{2}\Delta z$ and at the beginning of time step $t = (n+1)\Delta t$,

$$\begin{aligned}\frac{\hat{U}_J^{n+1} - \tilde{U}_J^n}{\Delta t} &= -\overline{W}_J \frac{\hat{U}_J^n - \hat{U}_{J-1}^n}{\Delta z} + \frac{\frac{\tau_x}{\rho_\circ} - K_b \frac{\hat{U}_J^n - \hat{U}_{J-1}^n}{\Delta z}}{\Delta z} - \\ &\quad \hat{U}_J^n \left(\frac{\partial \overline{U}}{\partial x}\right)_J - \left(\frac{\partial \overline{V'U'}}{\partial y}\right)_J - \left(\frac{1}{\rho_\circ}\frac{\partial \overline{P}}{\partial x}\right)_J \qquad \text{(C.9)} \\ \frac{\hat{T}_J^{n+1} - \tilde{T}_J^n}{\Delta t} &= -\overline{W}_J \frac{\hat{T}_J^n - \hat{T}_{J-1}^n}{\Delta z} + \frac{\frac{-Q_{net}}{\rho_\circ C_p} - K_b \frac{\hat{T}_J^n - \hat{T}_{J-1}^n}{\Delta z}}{\Delta z} - \\ &\quad \hat{U}_J^n \left(\frac{\partial \overline{T}}{\partial x}\right)_J - \left(\frac{\partial \overline{V'T'}}{\partial y}\right)_J \qquad \text{(C.10)}\end{aligned}$$

For the interior grids at $z_j = (j - J - \frac{1}{2})\Delta z$, $j = J-1, J-2, \ldots, 3, 2$, at the beginning of time step $t = (n+1)\Delta t$,

$$\begin{aligned}\frac{\hat{U}_j^{n+1} - \tilde{U}_j^n}{\Delta t} &= -\overline{W}_j \frac{\hat{U}_{j+1}^n - \hat{U}_{j-1}^n}{2\Delta z} + K_b \frac{\hat{U}_{j+1}^n - 2\hat{U}_j^n + \hat{U}_{j-1}^n}{(\Delta z)^2} - \\ &\quad \hat{U}_j^n \left(\frac{\partial \overline{U}}{\partial x}\right)_j - \left(\frac{\partial \overline{V'U'}}{\partial y}\right)_j - \left(\frac{1}{\rho_\circ}\frac{\partial \overline{P}}{\partial x}\right)_j \qquad \text{(C.11)}\end{aligned}$$

$$\frac{\hat{T}_j^{n+1} - \hat{T}_j^n}{\Delta t} = -\overline{W}_j \frac{\hat{T}_{j+1}^n - \hat{T}_{j-1}^n}{2\Delta z} + K_b \frac{\hat{T}_{j+1}^n - 2\hat{T}_j^n + \hat{T}_{j-1}^n}{(\Delta z)^2} - \hat{U}_j^n \left(\frac{\partial \overline{T}}{\partial x}\right)_j - \left(\frac{\partial \overline{V'T'}}{\partial y}\right)_j \quad \text{(C.12)}$$

At the bottom grid, $j = 1$, $z = -(K - \frac{1}{2})\Delta z$, boundary conditions are applied

$$\hat{U}_1^{n+1} = \hat{U}_1^{n+1} = \overline{U}_1 \quad \text{(C.13)}$$

$$\hat{T}_1^{n+1} = \hat{T}_1^{n+1} = \overline{T}_1 \quad \text{(C.14)}$$

Convective adjustment

After the application of forcing, the model checks for static instabilities throughout the profile of density. When static instability is detected, all properties at the grids involved are homogenized by the model (Fig. 37).

Once these convective adjustments are done, the model has three choices for its next step: (1) adjust for penetrative entrainment due to convective adjustments, (2) check for bulk Richardson number, or (3) bypass both (1) and (2).

Penetrative convection

About 15% of the potential energy supply from density inversion in the surface layer discussed above is available to entrain mass, momentum and heat from the grid(s) immediately below the surface mixed layer, with the rest dissipated. If the available potential energy is used up to entrainment whole sub-layers between two more grid levels, then properties of these sub-layers are homogenized with those in the surface mixed layer. If the available

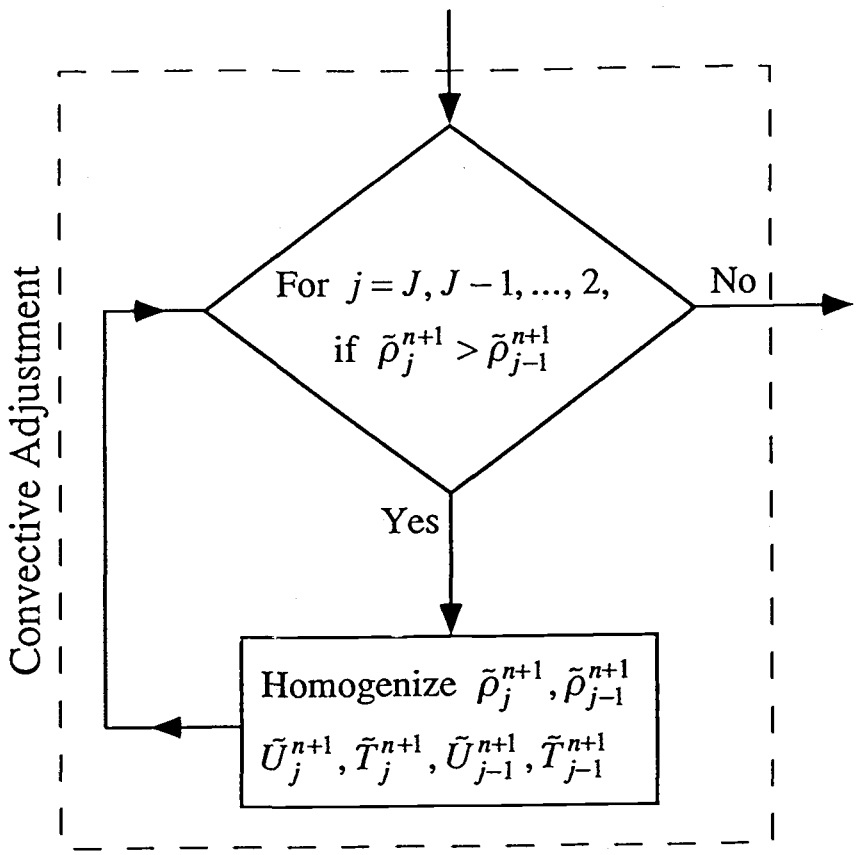

Figure 37. The component "Convective Adjustment" in the flowchart shown in Fig. 35.

potential energy, or the portion left after entraining whole sub-layers, is not enough to entrainment the next whole sub-layer, then the properties of the next sub-layer is partially mixed with the surface layer above so that all the available energy is used up completely, *i.e.*, the properties of this sub-layer are not identical to those in the mixed layer.

Bulk Richardson number mixing

After the adjustment for convection, Bulk Richardson number instability is checked for the surface mixed layer of depth $j_{MLD}\Delta z$, where j_{MLD}, with a minimum of 1, is the number of top grid(s) included by the surface mixed layer. If the bulk Richardson number R_b of the surface mixed layer is below the critical value of 0.65, the model homogenizes the grid below the surface layer, and then checks if the new, deeper mixed layer of depth $(j_{MLD}+1)\Delta z$ yields a value of R_b above its critical value. Iteration continues until a surface mixed layer with a stable R_b is obtained (Fig. 38).

Gradient Richardson number mixing

The algorithm for shear instability mixing using the gradient Richardson number criterion is shown in Fig. 39, and has been discussed in the text in detail. This is the last adjustment for turbulent mixing for a given time step.

Evaluation of turbulent fluxes and diffusivities

After applying the forcing and adjusting all the required mixing criteria for each time step, $t = (n+1)\Delta t$, the model obtain the final values of the properties of the time step $n+1$. Then the model evaluate the vertical

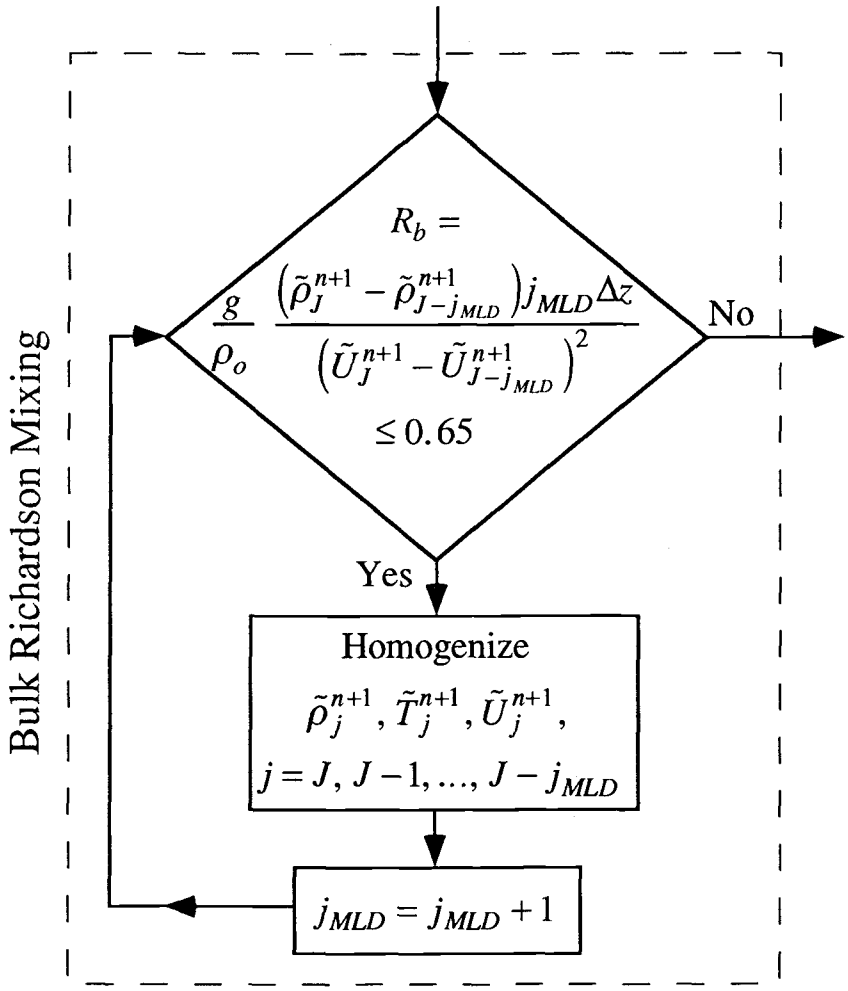

Figure 38. The component "Bulk Richardson Mixing" in the flowchart shown in Fig. 35.

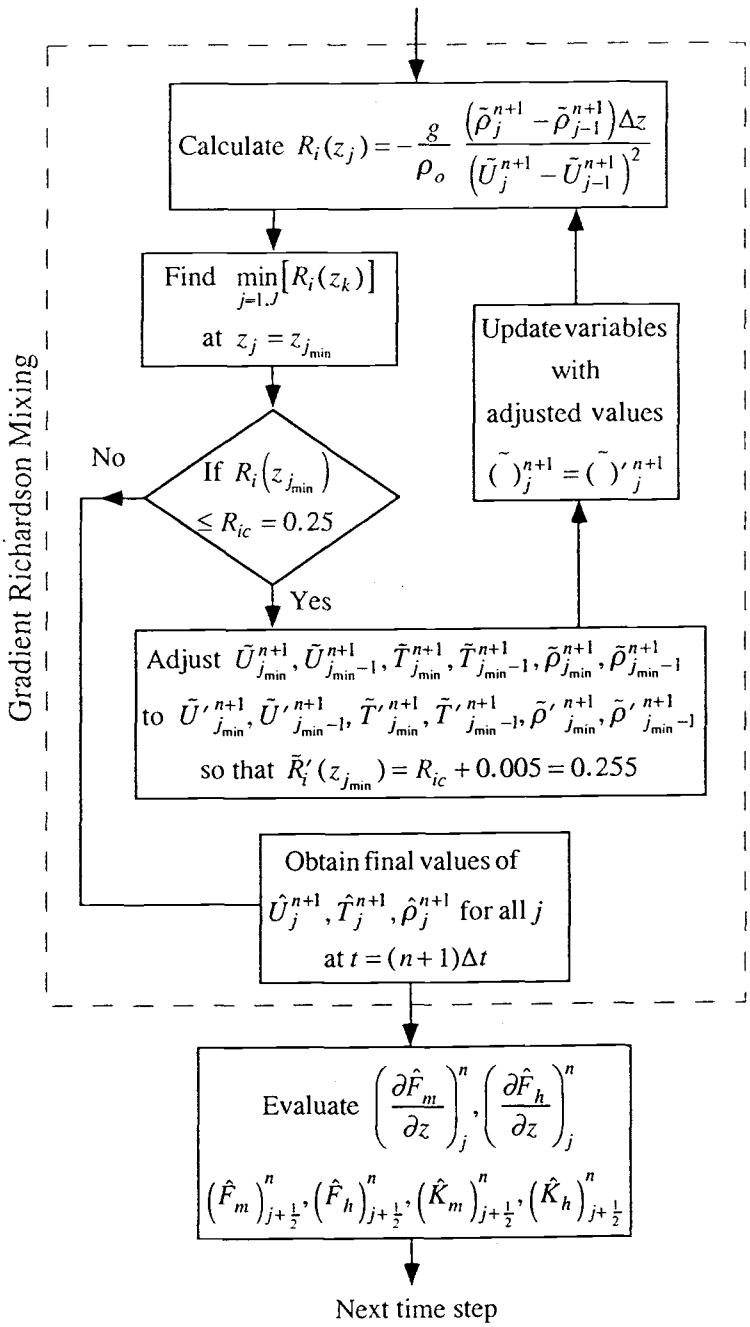

Figure 39. The component "Gradient Richardson Mixing" in the flowchart shown in Fig. 35.

convergence of turbulent fluxes of zonal momentum and heat that include the total effects of the background diffusion applied at the beginning of time step $n+1$ and all other model adjustments for turbulent mixing during the same time time step. When these values of turbulent convergences are applied together with forcing terms at the beginning of the time step $n+1$, the model yields same final values for all the properties for the time step without all the mixing adjustments.

At the bottom, $j = 1$,

$$\left(\frac{1}{\rho_\circ}\frac{\partial \hat{F}_m}{\partial z}\right)_j^n = -\overline{W}_j\frac{\hat{U}_{j+1}^n - \hat{U}_j^n}{\Delta z} - \hat{U}_j^n\left(\frac{\partial \overline{U}}{\partial x}\right)_j - \left(\frac{\partial \overline{V'U'}}{\partial y}\right)_j - \left(\frac{1}{\rho_\circ}\frac{\partial \overline{P}}{\partial x}\right)_j \tag{C.15}$$

$$\left(\frac{1}{\rho_\circ c_p}\frac{\partial \hat{F}_h}{\partial z}\right)_j^n = -\overline{W}_j\frac{\hat{T}_{j+1}^n - \hat{T}_j^n}{\Delta z} - \hat{U}_j^n\left(\frac{\partial \overline{T}}{\partial x}\right)_j - \left(\frac{\partial \overline{V'T'}}{\partial y}\right)_j \tag{C.16}$$

At the interior grids, $j = 2, 3, \ldots, J-2, J-2$,

$$\left(\frac{1}{\rho_\circ}\frac{\partial \hat{F}_m}{\partial z}\right)_j^n = -\frac{\hat{U}_j^{n+1} - \hat{U}_j^n}{\Delta t} - \overline{W}_j\frac{\hat{U}_{j+1}^n - \hat{U}_{j-1}^n}{2\Delta z} - \hat{U}_j^n\left(\frac{\partial \overline{U}}{\partial x}\right)_j - \left(\frac{\partial \overline{V'U'}}{\partial y}\right)_j - \left(\frac{1}{\rho_\circ}\frac{\partial \overline{P}}{\partial x}\right)_j \tag{C.17}$$

$$\left(\frac{1}{\rho_\circ c_p}\frac{\partial \hat{F}_h}{\partial z}\right)_j^n = -\frac{\hat{T}_j^{n+1} - \hat{T}_j^n}{\Delta t} - \overline{W}_j\frac{\hat{T}_{j+1}^n - \hat{T}_{j-1}^n}{2\Delta z} - \hat{U}_j^n\left(\frac{\partial \overline{T}}{\partial x}\right)_j - \left(\frac{\partial \overline{V'T'}}{\partial y}\right)_j \tag{C.18}$$

At the surface, $j = J$,

$$\left(\frac{1}{\rho_\circ}\frac{\partial \hat{F}_m}{\partial z}\right)_j^n = -\frac{\hat{U}_j^{n+1} - \hat{U}_j^n}{\Delta t} - \overline{W}_j\frac{\hat{U}_j^n - \hat{U}_{j-1}^n}{\Delta z} -$$

$$\hat{U}_j^n \left(\frac{\partial \overline{U}}{\partial x}\right)_j - \left(\frac{\partial \overline{V'U'}}{\partial y}\right)_j - \left(\frac{1}{\rho_\circ}\frac{\partial \overline{P}}{\partial x}\right)_j \qquad \text{(C.19)}$$

$$\left(\frac{1}{\rho_\circ c_p}\frac{\partial \hat{F}_h}{\partial z}\right)_j^n = -\frac{\hat{T}_j^{n+1} - \hat{T}_j^n}{\Delta t} - \overline{W}_j \frac{\hat{T}_j^n - \hat{T}_{j-1}^n}{\Delta z} - \hat{U}_j^n \left(\frac{\partial \overline{T}}{\partial x}\right)_j - \left(\frac{\partial \overline{V'T'}}{\partial y}\right)_j \qquad \text{(C.20)}$$

Write

$$\left(\frac{\partial \hat{F}_m}{\partial z}\right)_j^n = \frac{\left(\hat{F}_m\right)_{j+\frac{1}{2}}^n - \left(\hat{F}_m\right)_{j-\frac{1}{2}}^n}{\Delta z} \qquad \text{(C.21)}$$

$$\left(\frac{\partial \hat{F}_h}{\partial z}\right)_j^n = \frac{\left(\hat{F}_h\right)_{j+\frac{1}{2}}^n - \left(\hat{F}_h\right)_{j-\frac{1}{2}}^n}{\Delta z} \qquad \text{(C.22)}$$

Assuming turbulent fluxes across the top bound of the bottom grid are completely due to prescribed background diffusion (the model shows no other turbulent adjustments at the bottom grid):

$$\left(\hat{F}_m\right)_{1+\frac{1}{2}}^n = -\rho_\circ K_b \frac{\hat{U}_2^n - \hat{U}_1^n}{\Delta z} \qquad \text{(C.23)}$$

$$\left(\hat{F}_h\right)_{1+\frac{1}{2}}^n = -\rho_\circ C_p K_b \frac{\hat{T}_2^n - \hat{T}_1^n}{\Delta z} \qquad \text{(C.24)}$$

$$\left(\hat{K}_m\right)_{1+\frac{1}{2}}^n = K_b \qquad \text{(C.25)}$$

$$\left(\hat{K}_h\right)_{1+\frac{1}{2}}^n = K_b \qquad \text{(C.26)}$$

Then the values of turbulent fluxes and diffusivities at the top bound of grid $j = 2, 3, \ldots, J-1, J$, are approximated as

$$\left(\hat{F}_m\right)_{j+\frac{1}{2}}^n = \left(\hat{F}_m\right)_{j-\frac{1}{2}}^n + \Delta z \left(\frac{\partial \hat{F}_m}{\partial z}\right)_j^n \qquad \text{(C.27)}$$

$$\left(\hat{F}_h\right)_{j+\frac{1}{2}}^n = \left(\hat{F}_h\right)_{j-\frac{1}{2}}^n + \Delta z \left(\frac{\partial \hat{F}_h}{\partial z}\right)_j^n \qquad \text{(C.28)}$$

$$\left(\hat{K}_m\right)^n_{j+\frac{1}{2}} = -\left(\hat{F}_m\right)^n_{j+\frac{1}{2}} \left(\rho_\circ \frac{\hat{U}^n_{j+1} - \hat{U}^n_j}{\Delta z}\right)^{-1} \tag{C.29}$$

$$\left(\hat{K}_h\right)^n_{j+\frac{1}{2}} = -\left(\hat{F}_h\right)^n_{j+\frac{1}{2}} \left(\rho_\circ C_p \frac{\hat{T}^n_{j+1} - \hat{T}^n_j}{\Delta z}\right)^{-1} \tag{C.30}$$

Numerical stability and convergence

At the beginning of each time step, the application of (1) forcing, (2) prescribed background diffusion of constant diffusivity K_b, and (3) boundary conditions to the momentum equation alone, is similar to the numerical integration of the following parabolic partial differential equation of $\hat{U}$

$$\begin{aligned}
\frac{\partial \hat{U}}{\partial t} - K_b \frac{\partial^2 \hat{U}}{\partial^2 z} + \overline{W}\frac{\partial \hat{U}}{\partial z} + \frac{\partial \overline{U}}{\partial x}\hat{U} &= d(z) = -\frac{\partial \overline{V'U'}}{\partial y} - \frac{1}{\rho_\circ}\frac{\partial \overline{P}}{\partial x}, \\
&\quad -200 < z < 0, \quad 0 < t < T \\
\hat{U}\Big|_{t=0} &= \overline{U}(z), \quad 200 < z < 0 \\
\hat{U}\Big|_{z=-h_b} &= \overline{U}(z = -h_b), \\
\hat{U}\Big|_{z=0} &= \overline{U}(z = 0).
\end{aligned}$$

Similarly, for the heat balance

$$\begin{aligned}
\frac{\partial \hat{T}}{\partial t} - K_b \frac{\partial^2 \hat{T}}{\partial^2 z} + \overline{W}\frac{\partial \hat{T}}{\partial z} &= d(z) = -\frac{\partial \overline{V'T'}}{\partial y} - \frac{\partial \overline{T}}{\partial x}\hat{U}, \\
&\quad -200 < z < 0, \quad 0 < t < T \\
\hat{T}\Big|_{t=0} &= \overline{T}(z), \quad 200 < z < 0 \\
\hat{T}\Big|_{z=-h_b} &= \overline{T}(z = -h_b), \\
\hat{T}\Big|_{z=0} &= \overline{T}(z = 0).
\end{aligned}$$

Each of the explicit finite difference schemes for the above been proven to be stable and convergent (Richtmyer and Morton, 1967) if

$$k_b - \frac{\overline{W}}{2}\Delta z \geq 0$$

$$1 - \left[\frac{2K_b}{(\Delta z)^2} + \frac{\partial \overline{U}}{\partial x}\right]\Delta t \geq 0$$

For the typical values of $K_b = 1 \times 10^{-5}\,\mathrm{m^2 s^{-1}}$, $\max(\overline{W}) = 2.7 \times 10^{-5}\,\mathrm{m\,s^{-1}}$, and $\max(\partial\overline{U}/\partial x) = 2 \times 10^{-7}\,\mathrm{s^{-1}}$, it yields $\Delta z \leq 0.75\,\mathrm{m}$. and $\Delta t \leq 7.5\,\mathrm{hr}$.

Model tests yield almost identical stable solutions with $\Delta z = 0.5\,\mathrm{m}$ (not shown) and $\Delta z = 1\,\mathrm{m}$ (Fig. 12), very small artificial fluctuations with $\Delta z = 2\,\mathrm{m}$. and increasingly larger artificial fluctuations associated with numerical instability with larger Δz ($> 2\,\mathrm{m}$). The time series of simulated zonal velocity and temperature for the case of $\Delta z = 10\,\mathrm{m}$ is shown in Fig. 40. Numerical instabilities frequently trigger the vertical advection to adjust the model, and give rise to the fluctuations with the time scale of 100 days. Coarser vertical resolution produces larger magnitude fluctuations. However, when averaged over a period of 100 days, the simulated zonal velocity, temperature, and turbulent fluxes and diffusivities, show small differences for values of $\Delta z \leq 5\,\mathrm{m}$.

Increasing Δz with K_b fixed has an effects similar to reducing K_b with Δz fixed in this model (according to the theory, and to model tests not shown).

We also test the model with time steps Δt between 5 sec, and 1 hr with other parameters fixed (not shown), and confirm that simulations remain the same for time step between 5 seconds and 1 hour. However, increasing time step may not reduced computer integration time proportionately because

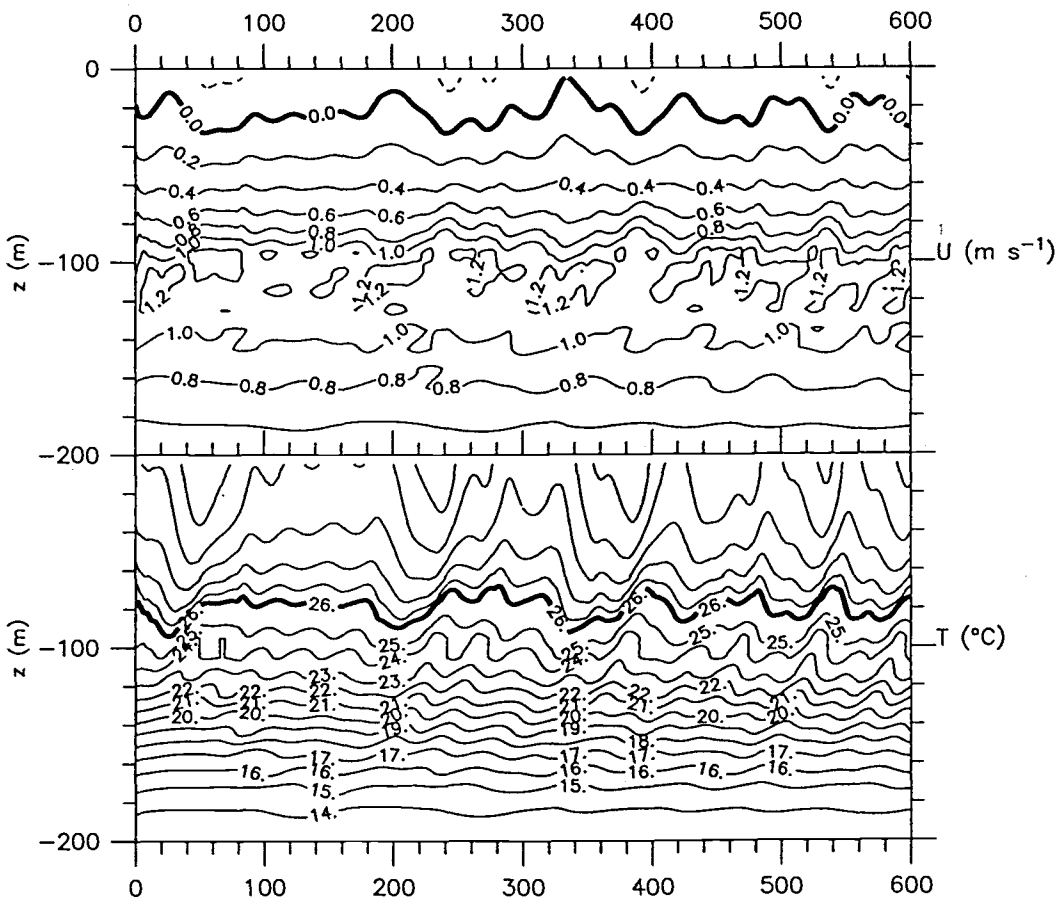

Figure 40. Same as Fig. 12 but with $\Delta z = 10\,\mathrm{m}$ instead of the standard case of 1 m. Numerical instabilities due to coarser vertical resolution gives rise to fluctuations with periods of about 100 days of the vertical advective time scale.